CNWRA 2007-003

LONG-TERM-AVERAGE INFILTRATION AT YUCCA MOUNTAIN, NEVADA: MILLION-YEAR ESTIMATES

Prepared for

U.S. Nuclear Regulatory Commission
Contract NRC–02–02–012

Prepared by

S. Stothoff
G. Walter

Center for Nuclear Waste Regulatory Analyses
San Antonio, Texas

August 2007

ABSTRACT

Yucca Mountain, Nevada, has been studied for more than 20 years as a potential location for geologic emplacement of high-level nuclear waste. Yucca Mountain is located approximately 160 km [100 mi] northwest of Las Vegas, Nevada, in an area with little rainfall and hot summers. The potential repository would be located in the thick unsaturated zone. Assessments of the potential performance of the repository indicate that water fluxes contacting waste can strongly influence repository performance. The importance of water fluxes on performance is evidenced by the significance of performance features such as waste package longevity and the distribution and magnitude of seepage fluxes into drifts. Because net infiltration is the ultimate source of water at depth, the amount and distribution of net infiltration above the repository footprint is anticipated to significantly influence potential repository performance.

Recognition of the important role of net infiltration in repository performance has resulted in a wide variety of studies attempting to quantify net infiltration at Yucca Mountain. Most of the work has focused on estimating net infiltration under present-day interglacial conditions, with a significant amount of work also considering how net infiltration might respond to other climates that may occur in the future. This report estimates future patterns of areal average net infiltration, temporally averaged over the next 1 million years, under the assumption that processes and characteristics occurring at present and in past glacial cycles can be projected into the future.

This report estimates million-year average future net infiltration in a series of steps using the Orbital-Cycle Climate for Yucca Mountain (OCCYM)[1] and Infiltration Tabulator for Yucca Mountain (ITYM)[2] models. First, OCCYM uses well-known insolation patterns for the next million years to infer several possible future continental ice volume sequences based on correlations from past glacial cycles. Second, OCCYM estimates climate local to Yucca Mountain, given continental ice volume, on 1,000-year intervals based on inferred climates during past glacial cycles. Third, OCCYM uses ITYM-calculated tables of areal-average net infiltration (given mean annual precipitation and temperature) and the estimated climate sequences to estimate net infiltration across a Footprint Box circumscribing the potential repository location during each 1,000-year interval. Climatic variability within each 1,000-year interval is accounted for based on inferences from bristlecone-pine tree-ring analyses. Finally, OCCYM tabulates the million-year-average Footprint Box net infiltration.

The OCCYM approach considers future orbital sequences to be deterministic, but incorporates uncertainty in the first, second, and third calculational steps. Uncertainty in future ice volume sequences is considered by varying two key parameters, yielding a total of 6 equally likely future ice volume sequences. Uncertainty in relating ice volume to the climate local to Yucca Mountain is incorporated by providing uncertainty bounds on both present-day and full-glacial-maximum mean annual precipitation and temperature estimates, and by considering three correlations between the ice volume sequences and present-day climate. Uncertainty in

[1]The Orbital-Cycle Climate for Yucca Mountain model is referenced frequently throughout this report. The acronym OCCYM will be used.

[2]The Infiltration Tabulator for Yucca Mountain model is referenced frequently throughout this report. The acronym ITYM will be used.

mean annual infiltration given climate is formally considered in the ITYM calculations, based on uncertainty in input parameters.

A second approach uses the U.S. Department of Energy (DOE) climate sequences estimated by Sharpe (2003) and Bechtel SAIC Company, LLC (2004) to provide future climate and future climate uncertainty. These sequences yield climatic estimates over durations of 500 to 40,000 years. The second approach estimates million-year-average Footprint Box net infiltration from local climate using the ITYM estimates in the same way as the first approach.

Million-year-average Footprint Box net infiltration is estimated to have an expected value and standard deviation of 41 and 33 mm/yr [1.6 and 1.3 in/yr], respectively, using the OCCYM approach, compared to an expected value and standard deviation of 41 and 32 mm/yr [1.6 and 1.3 in/yr], respectively, using the DOE climate sequences. Present-day decadal-average Footprint Box net infiltration is estimated to have both an expected value and standard deviation of 13 mm/yr [0.51 in/yr], for a mean annual precipitation of 201 mm/yr [7.9 in/yr] and mean annual temperature of 15.7 °C [60.3 °F] at an elevation of 1,524 m [5,000 ft].

References:

Bechtel SAIC Company, LLC. "Future Climate Analysis." ANL–NBS–HS–000008. Rev. 01. Las Vegas, Nevada: Bechtel SAIC Company, LLC. 2004.

Sharpe, S. "Future Climate Analysis—10,000 Years to 1,000,000 Years After Present." MOD–01–001. Rev. 01. Reno, Nevada: Desert Research Institute. 2003.

CONTENTS

CONTENTS (continued)

FIGURES

TABLES

ACKNOWLEDGMENTS

This report was prepared to document work performed by the Center for Nuclear Waste Regulatory Analyses (CNWRA) for the U.S. Nuclear Regulatory Commission (NRC) under Contract No. NRC–02–02–012. The activities reported here were performed on behalf of the NRC Office of Nuclear Material Safety and Safeguards, Division of High-Level Waste Repository Safety. The report is an independent product of the CNWRA and does not necessarily reflect the views or regulatory position of the NRC.

The authors would like to thank Dr. Randall Cervany for providing constructive and useful advice on alternative models for generating future climates. The authors wish to thank Dr. Robert Lenhard and Dr. Cynthia Dinwiddie for their technical reviews and Dr. Gordon Wittmeyer for his programmatic review. Thanks are also expressed to Lauren Mulverhill for her editorial review.

QUALITY OF DATA, ANALYSES, AND CODE DEVELOPMENT

DATA: All CNWRA-generated data contained in this report meet quality assurance requirements described in the Geosciences and Engineering Division Quality Assurance Manual. Sources of other data should be consulted for determining the level of quality of those data.

ANALYSES: The analyses performed using data obtained from other sources and using Infiltration Tabulator for Yucca Mountain (ITYM) results were coded in special-purpose Matlab routines interfacing with Microsoft® Excel spreadsheets. Input and output files for the Matlab-based analyses presented in this report are documented in CNWRA Scientific Notebook 563.

CODE: The ITYM code is controlled as part of the Total-system Performance Assessment (TPA) code. The version of the ITYM code used for the analyses in this report is part of Version 5.1 of the controlled TPA code.

1 INTRODUCTION

Yucca Mountain, Nevada, has been studied for more than 20 years as a potential location for geologic emplacement of high-level nuclear waste. Yucca Mountain is located approximately 160 km [100 mi] northwest of Las Vegas, Nevada, in an area with little rainfall and hot summers. The potential repository would be located in the thick unsaturated zone roughly 250 m [825 ft] above the current water table, with even greater thicknesses of unsaturated rock overlying the repository horizon. Assessments of the potential performance of the repository indicate that water fluxes contacting waste can strongly influence repository performance (NRC, 2004). The importance of water fluxes on performance is evidenced by the significance of performance features such as waste package longevity and the distribution and magnitude of seepage fluxes into drifts. Because net infiltration is the ultimate source of water at depth, the amount and distribution of net infiltration above the repository footprint is anticipated to strongly influence potential repository performance.

Net infiltration, mean annual infiltration, deep percolation, and recharge are terms that are often used interchangeably in the literature. Net infiltration and mean annual infiltration are synonymous, defined as the net flux of water passing into the zone where evapotranspiration influences are negligible (e.g., the maximum rooting depth). Recharge is the liquid water flux passing out of the vadose zone into the saturated zone at the water table. Deep percolation is the liquid water flux intermediate between the rooting zone and the water table. The magnitude and distribution of deep percolation crossing the repository horizon is particularly important for potential repository performance, as fluxes at this horizon determine the magnitude and distribution of seepage into drifts containing waste packages. Because the rock forming Yucca Mountain is fractured, faulted, and tilted, water is unlikely to travel vertically through the mountain in perfect piston-like fashion, with younger water overlying older water. Instead, water in fractures will move faster than water in the matrix, causing waters of different ages to mix and a certain amount of lateral redistribution to occur. Average percolation fluxes will decrease slightly from below the rooting zone to the water table, primarily due to vapor losses caused by upward geothermal-gradient-induced vapor transport and by air moving through the upper part of Yucca Mountain. When averaged over sufficiently large spatial and temporal scales, net infiltration, deep percolation, and recharge will be numerically quite similar; even though they may have different spatial patterns and respond to climate change at different rates.

Recognition of the important role of net infiltration in repository performance has resulted in a wide variety of studies attempting to quantify net infiltration at Yucca Mountain. Most of the work has focused on estimating net infiltration under present-day interglacial conditions, with a significant amount of work also considering how net infiltration might respond to other climates that may occur in the future. During the Pleistocene, glacial cycles occurred on a roughly 100,000-year period, and numerous lines of evidence suggest that present-day climatic conditions represent a relatively hot and dry stage of typical glacial cycles. Climatic patterns in the Yucca Mountain region have been generally arid to semiarid over the previous few glacial cycles, generally dominated by winter precipitation but with summer-dominated (monsoonal) conditions over a small fraction of the record (Bechtel SAIC Company, LLC, 2004a). Performance assessments have considered climatic variability over multiple glacial cycles using the Total System Performance Assessment code since the viability assessment (DOE, 1998), but the effect of climatic changes on net infiltration over such long periods has recently received more attention.

This report is part of a series of net infiltration reports under present and potential future climates at Yucca Mountain. The first report in the series, a literature review and analysis by Stothoff and Musgrove (2006), provided a global and regional context for estimates of net infiltration at Yucca Mountain. The second report (this document) synthesizes several lines of climatic evidence. It uses abstractions for net infiltration developed specifically for Yucca Mountain with the Infiltration Tabulator for Yucca Mountain (ITYM)[1] code to estimate bounds on million-year-average net infiltration, averaged over approximately 13 km^2 [5 mi^2] above the potential repository, for plausible future climate sequences. The third report (under preparation) documents the technical basis for the ITYM code and inputs.

To augment direct observational evidence from the Yucca Mountain vicinity, the literature review and analysis by Stothoff and Musgrove (2006) considered worldwide analog sites with climatic conditions that mimicked previous stages of the glacial cycle. The literature review concluded that site-specific conditions strongly influence recharge. The studies from outside the American West are difficult to directly apply to Yucca Mountain because the scatter in recharge estimates is even wider than the scatter in estimates of present-day net infiltration at Yucca Mountain. Literature from locations in the American West, while more useful, was found to require careful interpretation. One study of 16 hydrologic basins in east-central Nevada provided sufficient information to derive a relationship between mean annual precipitation and mean annual recharge for upland areas analogous to Yucca Mountain. Extrapolating this newly derived site-scale relationship to mean annual precipitation values typical of Yucca Mountain under present-day conditions yields estimates of mean annual infiltration of 2.5 to 6.3 mm/yr [0.098 to 0.25 in/yr].

Building on the analysis by Stothoff and Musgrove (2006), this report estimates bounds on million-year-average areal-average net infiltration at Yucca Mountain. Global climate, local climate, and vadose-zone processes are the three major factors assumed to affect net infiltration at Yucca Mountain. Global climate, driven by predictable changes in the Earth's orbital characteristics and characterized by continental ice volume, is assumed to play a dominant role in determining the local climate at Yucca Mountain by affecting the movement and nature of atmospheric air masses. Local climate, responding to the air masses moving over Yucca Mountain and characterized by mean annual precipitation and mean annual temperature at Yucca Mountain, directly affects the water balance above the potential repository footprint by mediating water supply to and loss from the vadose zone. Vadose-zone processes, which respond to local climate and depend on soil and bedrock hydraulic properties, vegetation, and overland flow, also directly affect the water balance above the potential repository by determining what fraction of infiltration pulses overcome evapotranspiration and move deep within Yucca Mountain.

There are uncertainties associated with each of the three major infiltration-affecting factors. The future response of continental ice volumes to orbital forcing is unknown; the precise relationship between continental ice volume and Yucca Mountain climate is unknown; and areal-average net infiltration cannot be directly measured under present-day climatic conditions, much less under different climatic conditions. Because of the uncertainties associated with each

[1]The Infiltration Tabulator for Yucca Mountain module is referenced frequently throughout this chapter. The acronym ITYM will be used.

infiltration-affecting factor, a probabilistic approach is followed in this report to estimate long-term-average net infiltration at Yucca Mountain.

This report includes three major analysis sections, introductory and summary sections, and three supplementary appendices. The first major section, Section 2, describes the construction of potential sequences of climate on millennial-scale timesteps to represent the next million years. Two approaches are considered: the Department of Energy approach derived by Sharpe (2003) and the independent Orbital-Cycle Climate for Yucca Mountain (OCCYM) approach derived in this report. Both approaches are based on well-known parameters describing the past and future orbit of the Earth, relate the global glacial stage to orbital parameters, and relate local climate to the global glacial stage using paleoclimate proxies. The approaches differ in their level of complexity and the observations and interpretations incorporated in the model. Estimates of uncertainty are derived for the global glacial stage and for the local climate in both approaches.

Section 3, describes ITYM, a model that estimates net infiltration and the associated uncertainty on a square grid with 30-m [98-ft] sides. The estimates are based on a reference climate state described by mean annual precipitation and temperature for a typical decade. The ITYM estimates are averaged into a summary set of statistics called the Decadal-Scale Footprint Box Infiltration estimates (Decadal Infiltration estimates) that represent all grid cells within a box circumscribing the potential repository layout. The Decadal Infiltration estimates scale up temporal processes occurring over time periods of minutes to years and spatial processes occurring over length scales of centimeters up to kilometers. The Decadal Infiltration estimates are compared to estimates of infiltration and recharge from studies of Yucca Mountain and locations in nearby Nevada, which suggest that the model reasonably represents both present-day infiltration and the change in infiltration that might be expected due to climate change associated with a glacial cycle. The Decadal Infiltration estimates are scaled up to the time scales associated with orbital dynamics, creating the Millennial-Scale Footprint Box Infiltration estimates (Millennial Infiltration estimates) that account for variability in climate between time scales of decades to millennia. The effect of precipitation seasonality on net infiltration is also investigated in Section 3, as paleoclimatic indicators suggest that a stronger summer monsoon has occurred during some portions of previous glacial cycles. Estimates of winter and summer recharge efficiency (the fraction of precipitation becoming recharge) lead to a model for effective present-day precipitation. The model scales winter and summer precipitation by their corresponding seasonal recharge efficiencies, yielding an effective mean annual precipitation under current seasonality that would induce the same recharge. Estimated recharge efficiencies imply that even a large increase in summer precipitation has a relatively small influence on Decadal Infiltration.

Section 4 uses the probability distributions of potential future Yucca Mountain climate for the next million years (derived in Section 2) and the probability distribution of Millennial Infiltration given climate (derived in Section 3) to estimate probability distributions of million-year-average areal-average net infiltration. An analysis extrapolating natural variability cycles suggests that uncertainty in infiltration processes given climate has a larger effect on million-year-average net infiltration than uncertainty in future climate over the million-year time scale. The probability distribution for million-year net infiltration based on best estimates is well described by a lognormal distribution with a mean value of 40.6 mm/yr [1.60 in/yr] and a coefficient of variation equal to 0.810. Estimates assuming a steady-state climate with the long-term-average climatic conditions have a mean value of 37.7 mm/yr [1.48 in/yr] and a coefficient of variation equal to

0.793, implying that climatic variability and uncertainty over multiple glacial cycles increases the median long-term-average net infiltration by less than 8 percent and slightly increases the scaled spread in estimates.

Section 4 also considers anthropogenic effects on climate, which may cause climatic conditions to deviate from the natural cycle for some period into the future. Hypothesized anthropogenic effects significantly reduce average infiltration rates during the anthropogenic period, but average infiltration over a million years is relatively unaffected if the anthropogenic period is less than 1 or 2 glacial cycles out of the approximately 10 cycles anticipated for the next million years. This finding suggests that natural-cycle estimates reasonably represent million-year-average future deep percolation even if anthropogenic effects on climate do not completely dissipate for hundreds of thousands of years.

Section 5 summarizes the analyses and conclusions presented in Sections 2–4.

2 FUTURE CLIMATE ESTIMATES

Long-term-average net infiltration estimates for Yucca Mountain depend on estimates of climatic conditions over the period of interest. Climatic conditions may be described in several ways, such as time sequences of climatic conditions, long-term-average conditions, most likely conditions, worst-case conditions, and so forth. These different climatic descriptions will generally yield different estimates of average net infiltration.

Estimates of future climates are inherently uncertain so the approach used for estimating long-term-average infiltration is based on estimates of time sequences of climatic conditions while explicitly accounting for uncertainty. Sequences of future climates are transformed into a probability distribution of average climatic conditions over periods representative of orbital change (e.g.,10 thousand years). Climatic variability at shorter time scales is incorporated in the infiltration model, as described in Section 3. The probability distributions for climatic conditions and for net infiltration given a climatic condition are combined in Section 4.

Two contrasting approaches are used to estimate climatic probability distributions. Sharpe (2003) considers several climate states that represent the range of climatic conditions thought to have occurred over the last 800,000 years. The occurrence of each state is associated with insolation triggers that are estimated from past glacial cycles. The Orbital-Cycle Climate for Yucca Mountain (OCCYM)[1] approach developed in this report also uses insolation to drive climate change, but the linkage is mediated by continental ice volume dynamics. Data discussed in this section are referenced in Appendix C.

2.1 Sharpe (2003) Model

Sharpe (2003) developed a sequence of future climate states based on correlation of paleoclimate conditions with Earth's orbital cycles. The Sharpe (2003) analysis is built on the extensive work by Forester, et al. (1999) and Thompson, et al. (1999a), adopting the approach used for the future climate analysis for the next 10 thousand years at Yucca Mountain that was most recently presented by Bechtel SAIC Company, LLC (2004a). Walter (2005) discusses the Sharpe (2003) model assumptions in detail, using an earlier revision of the Sharpe (2003) report.

The Sharpe (2003) model is straightforward. An undated sequence of late Pleistocene climatic conditions was established from diatom and ostracode sequences in Owens Lake sediment cores. Sharpe (2003) correlated the fossil algae and microcrustacean assemblages in the sediment cores to geographical and climatic conditions under which these species are found today. To describe the climatic conditions implied by these assemblages, Sharpe (2003) used six climatic states: interglacial (or modern), intermediate, monsoon, and three full-glacial states. Sharpe (2003) linked these states to absolute dates and durations using the Devils Hole vein calcite record (Winograd, et al., 1992) and the Vostok ice core record (Petit, et al., 1999). Sharpe (2003) created rules linking the dated climate sequence to changes in orbital characteristics for the Earth, and estimated a sequence of future climatic conditions at Yucca

[1]The Orbital-Cycle Climate for Yucca Mountain is referenced frequently throughout this chapter. The acronym OCCYM will be used.

Mountain for the next 1 million years by applying the same rules to the future sequence of the same orbital characteristics.

Sharpe (2003) describes the climatic conditions for each climate state by providing upper and lower bounds for the climate state. Each bound is described using two or more analog meteorological stations, representing the 1,524-m [5,000 ft] elevation at Yucca Mountain. A range of mean annual precipitation (MAP)[2] and mean annual temperature (MAT)[3] can be inferred from these analog stations. Sharpe (2003) does not state whether these bounds represent uncertainty on the average climatic condition over the interval or the extreme conditions encountered during the interval; in the current report, it is assumed that the given ranges represent uncertainty on the average climatic condition.

Meteorologic records from the Sharpe (2003) future-climate analog stations were used as input to a site-specific infiltration model (e.g., Bechtel SAIC Company, LLC, 2004b), but the present-day climate Sharpe (2003) recommended was not used for the Bechtel SAIC Company, LLC (2004b) infiltration model. Sharpe (2003) cited the work of Thompson, et al. (1999a) as a basis for the climate for present-day conditions, with MAP equal to 125 mm/yr [4.9 in/yr]. Thompson, et al. (1999a) interpolated present-day MAP to Yucca Mountain using a sparse set of stations that did not include Nevada Test Site stations. However, more than 45 years of observations from the Nevada Test Site suggest that present-day MAP may be more than 200 mm/yr at the same elevation. Bechtel SAIC Company, LLC (2004b) used a different set of stations to represent interglacial and lower bound monsoon conditions with a significantly higher areal-average MAP.

A revised estimate of present-day climatic conditions, replacing the Sharpe (2003) model estimates, can be determined from a suite of site-specific observations. Bechtel SAIC Company, LLC (2004c) does not supply climate at the reference elevation of 1,524 m [5,000 ft], but climate at the reference elevation can be estimated using their models. Bechtel SAIC Company, LLC (2004b) adjusts each climate state to describe conditions at a 1,400-m [4,590-ft] elevation, then distributes MAP and MAT over Yucca Mountain using elevation-dependent models. The Bechtel SAIC Company, LLC (2004b) MAP model is

$$P = \exp(0.6458Z + 4.317) \tag{2-1}$$

where P is MAP [mm/yr] and Z is elevation [km]. The Bechtel SAIC Company, LLC (2004b) MAT model is

$$T - T_r = 9.8(1.4 - Z) \tag{2-2}$$

where T is MAT [°C] and T_r is MAT [°C] at a 1,400-m [4,590-ft] elevation. The adjusted MAT for 1,524-m [5,000-ft] elevation is 13.9 to 17 °C [57 to 63 °F].

---

[2]Mean annual precipitation is referenced frequently throughout this chapter. The acronym MAP will be used.

[3]Mean annual temperature is referenced frequently throughout this chapter. The acronym MAT will be used.

Prior glacial cycles are conventionally dated according to Marine Isotope Stage (MIS) numbers, which represent $\delta^{18}O$ signatures in a collection of cores from ocean sediments from around the world. These are also referred to as Oxygen Isotope Stage (OIS) numbers. Polar and continental ice sheets preferentially segregate lighter oxygen isotopes, thus the presence of large continental ice sheets shifts the isotopic composition of oxygen in the world's oceans. Odd MIS numbers represent interglacial conditions and even numbers represent glacial conditions, with the Holocene denoted by MIS 1 and the last glacial maximum denoted by MIS 2. Forester, et al. (1999) suggest that orbital eccentricity cycles approximately repeat on a period of approximately 400,000 years; thus each of the four 100,000-year glacial cycles in an eccentricity cycle is analogous to the same glacial cycle in other eccentricity cycles. Note that under the MIS numbering scheme, the collection of 4 glacial cycles uses 10 MIS numbers, so climatic conditions for MIS 6 and 16 or MIS 2 and 12 are analogous.

Figure 2-1 shows two proxy indicators for ice volume based on oxygen isotope data, the Devils Hole calcite vein record (Winograd, et al., 1992) and the Spectral Mapping Project (SPECMAP) stacked marine core record (Imbrie, et al., 1989), as well as the Sharpe (2003) interpretation of glacial stages. The proxy indicators are normalized to the range of 0 to 1 to facilitate comparisons. Sharpe (2003) includes a monsoonal period in each intermediate glacial stage following an interglacial stage. Note that the Devils Hole record suggests that MIS stages 8 and 10 were more severe than MIS stages 6 and 2 through 4, but the SPECMAP record suggests the opposite.

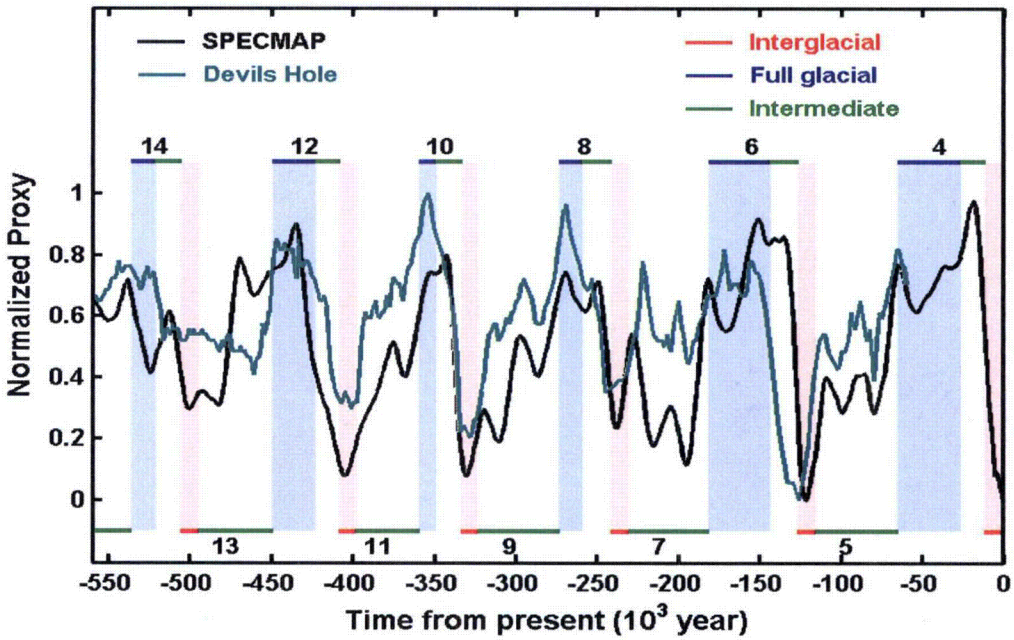

Figure 2-1. Normalized Proxy Indicators of Past Glacial States and the Corresponding Sharpe (2003) States and MIS Numbers

Sharpe (2003) considers three full-glacial states, represented by MIS 6 and 16, MIS 2 through 4, and MIS 8 and 10, calling these full-glacial states MIS 6/16, MIS 2, 4, and MIS 8,10, respectively. Sharpe (2003) draws upon the DOE future climate analysis to define climatic conditions for each state, with the most recent revision of the future climate analysis presented by Bechtel SAIC Company, LLC (2004a). Sharpe (2003) also considers an interglacial state, a monsoon state, and an intermediate state. Figure 2-2 displays the Sharpe (2003) climate states at the 1,524 m [5,000 ft] elevation of Yucca Mountain, using the inferred values for the interglacial and lower-bound monsoon states. The fraction of the next 1 million years that each climate state will occur, as estimated by Sharpe (2003), is indicated in the legend.
Sharpe (2003) describes MIS 6/16 as cold and wet, MIS 2, 4 as warmer and drier, and MIS 8,10 as even warmer, but wetter. The MIS 6/16 climate range shows no overlap with the MIS 2, 4 climate range, sharing one MAP/MAT point at the warm and dry extreme for MIS 6/16 and cold and wet extreme for MIS 2, 4.

2.2 Estimates of Previous Climatic Conditions

Sharpe (2003) rationalizes the selection of meteorological stations representing future-climate analog sites in terms of atmospheric conditions and rain shadows. These climatic factors are important considerations when developing meteorologic boundary conditions for infiltration simulators, but there are relatively few stations available with long high-quality meteorologic records possessing the requisite climatic conditions. However, additional sources of information not considered by Sharpe (2003) are available to further constrain the climatic conditions during other parts of previous glacial cycles.

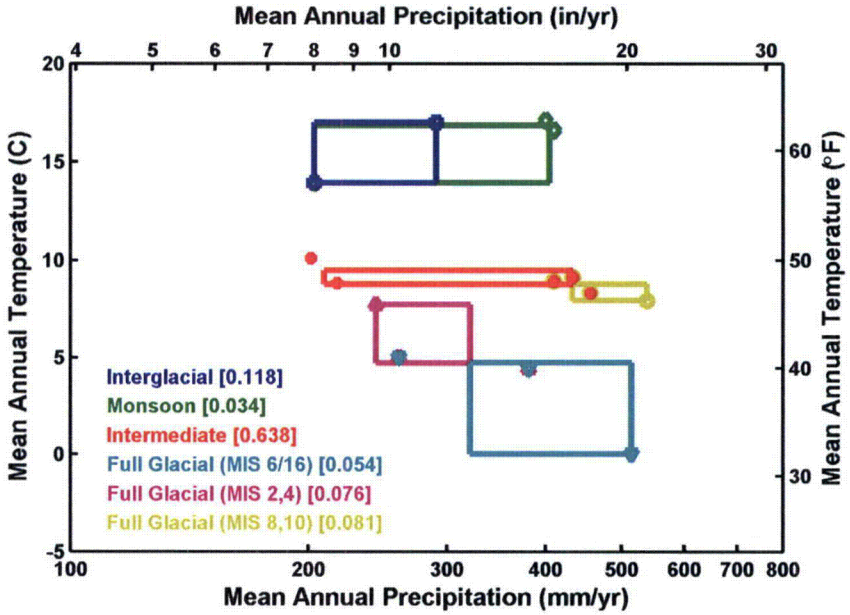

Figure 2-2. Climate States Defined by Sharpe (2003). Analog Sites Are Denoted by Symbols; Climate Boxes Are Obtained by Averaging MAP and MAT for the Analog Sites at Each Bound. The Fraction of the Next 1 Million Years That Sharpe (2003) Estimated for Each Climate State Is Indicated in Brackets.

2.2.1 Glacial Indicators From Owens Lake

Bechtel SAIC Company, LLC (2004a) uses ostracode sequences from Owens Lake drawn from the discussion by Forester, et al. (1999), comparing this evidence to regional evidence of lake stands to infer regional climatic conditions during glacial states. Several species in the record have different tolerances for water temperature and chemistry, and Bechtel SAIC Company, LLC (2004a) infers a range of Owens Lake conditions ranging from alkaline and closed conditions through stable, large, deep, cold and dilute conditions representing an overflowing lake. The ostracode record suggests that MAT was warmest in MIS 10 and was progressively cooler in stages 8, 2, and 6.

The ostracode record suggests that Owens Lake was freshest and coldest in parts of MIS 6 and 2, based on the presence of a species (*Cytherissa lacustris*) that is only found in a few large lakes south of Canada and Alaska today. Bischoff, et al. (1997) measured rock flour in one of the same cores for the period from 155,000 to 10,000 years before present, interpreting elevated rock-flour concentrations as evidence of mountain-glacier advances in the neighboring Sierra Nevada range. Elevated rock-flour concentrations are consistently associated with the presence of *C. lacustris* in this core section. Last-glacial-maximum mountain glaciers terminated below an elevation of 2,000 m [6,600 ft] along the eastern flank of the Sierra Nevada range (Moore, 2000; Kaufman, et al., 2003), within 10 km [6.2 mi] of the edge of the expanded lake. The extent that cold melt runoff lowered the temperature of Owens Lake during periods with extensive glacier activity is not known, but such runoff may have contributed to the presence of *C. lacustris*.

Less extreme wet conditions, at least intermittently spilling, are indicated in all glacial stages and portions of some interglacial stages by the presence of *Candona caudata*, a species found today as far south as the Pahranagat Lakes, Nevada. Other species indicate drier conditions during interglacial stages, with occasional intervals indicating augmented summer precipitation.

Forester, et al. (1999) present corroborating evidence for saline conditions based on diatoms preserved in Owens Lake cores. Most of the intervals with high concentrations of saline diatoms correspond to intervals with ostracode signatures suggestive of saline conditions. Smith and Bischoff (1997) present a considerable body of additional evidence derived from the Owens Lake cores that generally corroborates interpretations of Owens Lake hydrologic conditions (e.g., spilling, cold, and fresh; intermittently spilling; closed and saline).

2.2.2 Last Glacial Maximum Climate Indicators

Sharpe (2003) relied on the climate analysis by Thompson, et al. (1999a) to estimate climate under present-day conditions and during the last glacial maximum. Thompson, et al. (1999a) estimated present-day MAP and MAT for the elevation of 1,524 m [5,000 ft] at Yucca Mountain, apparently based on interpolated average values from the National Weather Service for the period of 1951 through 1980. Thompson, et al. (1999a) estimated MAP to be 125 mm/yr [4.9 in/yr] and MAT to be 13.4 °C [56.1 °F] for present-day conditions. Thompson, et al. (1999a) used the same interpolation procedure to estimate the range of MAP and MAT at locations where indicator plant species are found today, and used plant macrofossil assemblages from selected packrat middens to estimate MAP of 266 to 321 mm/yr [10.5 to 12.6 in/yr] and MAT of 7.9 to 8.5 °C [46 to 47 °F] at the last glacial maximum. Thompson, et al. (1999a), therefore, estimates an increase of approximately 2.1 to 2.6 times present MAP and cooling by 4.9 to

5.5 °C [8.8 to 9.9 °F] from present MAT. Spaulding (1985) used packrat midden data to derive climatic conditions for the Nevada Test Site, estimating present-day MAP of 189 mm/yr [7.4 in/yr] and MAT of 13.5 °C [56 °F] and last-glacial-maximum MAP of 246 to 265 mm/yr [9.7 to 10.4 in/yr] and MAT of 6.5 to 7.5 °C [44 to 46 °F]. Spaulding (1985), therefore, estimates an increase of approximately 1.3 to 1.4 times present MAP and cooling by 6 to 7 °C [11 to 13 °F] from present MAT.

Plant macrofossils from packrat middens helps constrain estimates of climatic conditions, but there are drawbacks in using this information to make climatic inferences. The U.S. Geological Survey (USGS)/National Oceanic and Atmospheric Administration North American Packrat Midden Database is a large collection of samples obtained from packrat middens (Strickland, et al., 2001). Most samples in the database use a single macrofossil for dating the entire sample, but some have as many as five age determinations. Figure 2-3 shows all age-difference pairs available from individual samples in the database. Half of the samples in the database with multiple dates were different by more than 1,000 years and 20 percent were different by more than 3,000 years. These age differences suggest that a single sample may be a collection of macrofossils over several thousand years, which is long enough to encompass at least one millennial-scale wet/dry climatic cycle.

Inferring climate from the presence of several species requires that the climatic tolerances of the species are known, but different researchers report significantly different climatic tolerances.

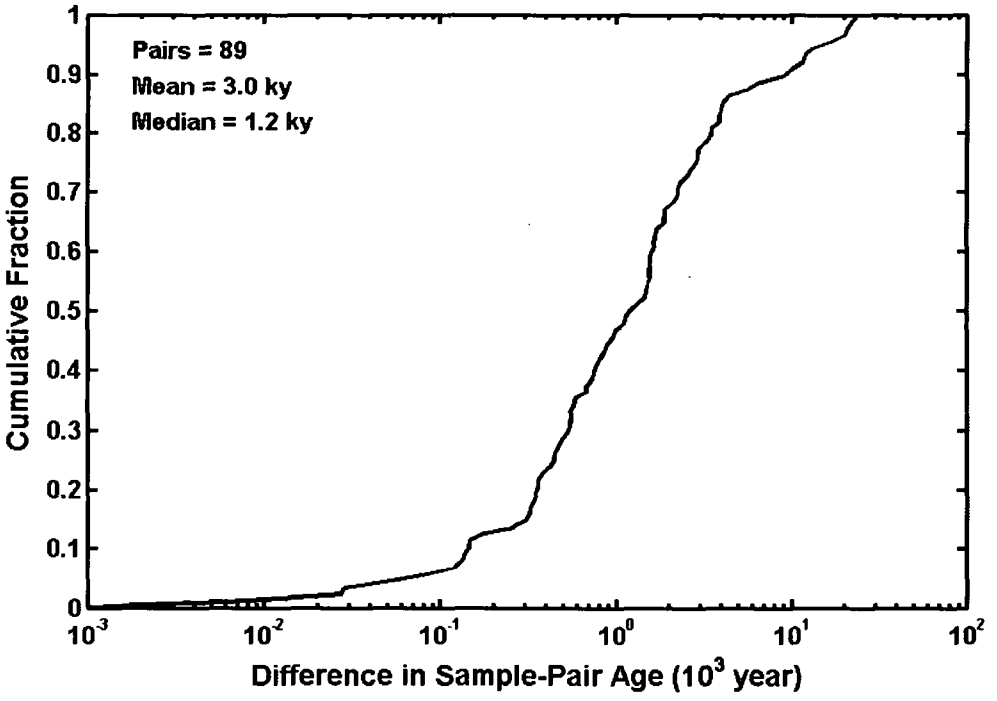

Figure 2-3. Cumulative Fraction of Subsample Age Differences in Samples Obtained From Packrat Middens

For example, Forester, et al. (1999) uses 380 to 560 mm/yr [15 to 22 in/yr] for the MAP tolerance of limber pine (*Pinus flexilis*) and 510 to 890 mm/yr [20.1 to 35 in/yr] for the MAP tolerance of Rocky Mountain white fir (*Abies concolor*). Thompson, et al. (1999b) provides MAP ranges for which 10 to 90 percent of the species occurs, with limits of 365 to 910 mm/yr [14.4 to 35.8 in/yr] for limber pine and 375 to 1,185 mm/yr [14.8 to 46.7 in/yr] for Rocky Mountain white fir. This uncertainty in climatic tolerance, combined with the possibility of favorable or unfavorable microclimatic conditions near a midden, makes it difficult to firmly estimate climate during a particular period. In addition, plant species may have different responses to changes in the concentration of atmospheric carbon dioxide, which is typically not accounted for in interpretations of climate change from packrat midden samples. Atmospheric carbon dioxide, as recorded in the Vostok ice core (Barnola, et al., 2003), varied between approximately 180 and 300 ppm over the past 417,000 years, with lower levels during glacial periods. Loehle (2007) suggests that indications of extremely cold and dry conditions in the eastern United States during the last glacial maximum, inferred from biological factors such as tree line lowering, may be instead attributable to carbon dioxide starvation. Finally, plant distributions are affected by competition between species and dispersal constraints, especially during periods of changing climate, so that the presence and absence of species is not solely determined by climate.

Additional lines of evidence from Nevada and neighboring areas, not discussed by Sharpe (2003), are available to estimate the difference in climate from the last glacial maximum to present. These lines of evidence are quite consistent in constraining MAP to a relatively narrow range of 1.7 to 1.9 times present MAP during the last glacial maximum.

Hostetler and Benson (1990) used a water balance model of Lake Lahontan in northwest Nevada and northeast California to estimate climate during the last glacial maximum. Hostetler and Benson (1990) found that multiplying MAP by 1.8 and sufficiently reducing evaporation replicated high stands of Lake Lahontan during the last glacial maximum.

D'Agnese, et al. (1999) considered climate change in the Death Valley region by increasing recharge in a groundwater model. A fivefold regional increase in recharge resulted in a water table rise in the vicinity of Yucca Mountain on the order of 100 m [330 ft], comparable to known paleospring discharge elevations, and produced reasonable lake levels across the region. The regional upland recharge models presented in Section 3 yield a similar multiple of recharge using an elevation change of approximately 900 m [2,950 ft], with MAP increasing by a factor of approximately 1.8 and MAT decreasing by approximately 5.6 °C [10.1 °F].

Kessler, et al. (2006) used a two-dimensional physically based numerical model to simulate mountain glaciers in the vicinity of Kings Canyon of the Sierra Nevada range during the last glacial maximum. A wide range of MAP and MAT changes was able to produce simulated glacier extent matching observed glacier extent in Kings Canyon, which is on the west flank of the Sierra Nevada range, as long as wetter conditions compensated for warmer conditions. However, the east flank of the Sierra Nevada has a different compensation relationship between MAP and MAT because of the rain-shadow effect, smaller accumulation areas, and steeper slopes on the east flank. When both eastern and western flanks were considered simultaneously, the simulation best matching both flanks had a MAP multiplier of 1.9 and MAT reduction of 5.6 °C [10.1 °F]. The regression relationships suggest a slightly drier and cooler state, with a MAP multiplier of 1.7 to 1.8 and MAT reduction of 5.6 to 5.7 °C [10.1 to 10.3 °F], which is equivalent to a change in elevation of approximately 800 to 900 m [2,600 to 3,000 ft].

Kaufman, et al. (2003) compiled recognized glaciations of the Sierra Nevada during the Pleistocene. The extent of the glaciation is related to the equilibrium line altitude, where accumulation and deflation are balanced. According to Kaufman, et al. (2003), the last glacial maximum saw an east-flank equilibrium line altitude about 800 m [2,620 ft] lower relative to present at latitude 37 °N, with prior equilibrium line altitudes during MIS 4 through 2 an additional 100 m [330 ft] lower. The most extreme lowering of the east-flank equilibrium line altitude over the past 820,000 years is approximately 200 m [660 ft] below the last glacial maximum during MIS 6, suggesting that MIS 6 was only marginally more extreme than MIS 2.

Changes in MAP and MAT can be inferred using the difference in elevation ranges for individual species found in midden samples rather than directly estimating MAP and MAT changes from changes in species assemblages. Note that inferences from elevation changes tacitly assume that MAP and MAT changed approximately according to the present-day elevation gradient. Forester, et al. (1999) noted that limber pine and white fir were observed at elevations more than 1,000 m [3,300 ft] lower than previously seen in southern Nevada during the last glacial maximum. An elevation shift of 1,000 m [3,300 ft] implies that MAP was approximately 1.9 times larger and MAT was reduced by approximately 6 to 7 °C [11 to 13 °F] using present-day gradients, a change in climate intermediate between the Thompson, et al. (1999a) and Spaulding (1985) estimates. A similar elevation shift in juniper is found in Owens Valley middens, implying that this change was regional in extent. It is possible that a larger change in elevation occurred, because there is a limited range in midden elevations at any locale. Note that changes in elevation for plants may result from changes in MAP, MAT, atmospheric carbon dioxide concentration, and dominant season for precipitation. Consistent with the analysis by Loehle (2007), estimates of climate change resulting from elevation shifts for plant species are more extreme than estimates using abiotic factors.

The additional lines of evidence not considered by Sharpe (2003) suggest that MAP was 1.7 to 1.9 times present values during the last glacial maximum and MAT was reduced by 5.6 to 7 °C [10.1 to 12.6 °F]. These ranges were doubled to account for uncertainty, yielding ranges of 1.6 to 2 times present MAP and a MAT reduction of 4.9 to 7.7 °C [8.8 to 13.9 °F] .

2.2.3 Earlier Glacial States

The evidence for climatic states is sparser for earlier glacial stages. The penultimate full glacial maximum during MIS 6 showed more extreme change based on (i) somewhat higher lake stands in northern Nevada (Reheis, 1999), (ii) east-flank mountain-glacier equilibrium line altitudes 200 m [660 ft] approximately lower in the Sierra Nevada (Kaufman, et al., 2003), and (iii) somewhat greater deviations of pollen assemblages from present conditions (Woolfenden, 2003). All of these indicate that the penultimate full glacial maximum was incrementally more extreme than the last glacial maximum. A 200 m [660 ft] increase in elevation (equivalent to lowering the equilibrium line altitude) increases MAP by approximately 14 percent and decreases MAT by approximately 2 °C [3.6 °F]. Applying these factors to the last glacial maximum yields an estimate of MAP 1.8 to 2.3 times present-day values and MAT reduced by 6.9 to 9.7 °C [12.4 to 17.5 °F] for the penultimate glacial maximum.

Forester, et al. (1999) suggest that 400,000-year eccentricity cycles are analogous. The penultimate 400,000 year eccentricity cycle is considered analogous to the last 400,000-year cycle, although perhaps with increased effective moisture. Lake stands were somewhat higher during the MIS 16 than during the MIS 6 glaciations (Reheis,1999), which are analogous, and

higher during the MIS 12 than during the MIS 2 glaciations (also analogous). However, little or no evidence of Sierra Nevada glaciation remains from this cycle (Kaufman, et al., 2003), suggesting that subsequent glaciers overrode the glacier deposits from the penultimate eccentricity cycle. This apparent contradiction may be due in part to ongoing uplift of the Sierra Nevada range. As Sharpe (2003) notes, Sierra Nevada uplift may be occurring at a rate of 175 to 345 m/My [570 to 1,130 ft/My], corresponding to 70 to 140 m [230 to 460 ft] per eccentricity cycle. Glacier evidence from a slightly more severe climatic state in the previous eccentricity cycle may have been overridden by subsequent glaciers due to uplift carrying the evidence to higher elevations. Also, a higher Sierra Nevada intensifies the rain shadow, which may have reduced east-flank MAP in the latest eccentricity cycle. It may also be that smaller ice sheets in the penultimate cycle did not deflect storm tracks as far south, delivering more moisture to northern Nevada and less to the southern Sierra Nevada and Yucca Mountain. This latter interpretation is consistent with the Owens Lake record, which suggests shallow water conditions from 650,000 to 450,000 years before present, and the Searles Lake record, which suggests shallow water conditions from 650,000 to 350,000 years before present gradually increasing to deep conditions by 150,000 years before present (Smith and Bischoff, 1997). Accordingly, the estimates for the last eccentricity cycle are also assumed to be appropriate for the penultimate cycle.

It is difficult to directly constrain the climatic conditions for the MIS 8 and 10 glaciations, as mountain-glacier evidence has been overridden. Forester, et al. (1999) interprets the ostracode record in these two glacial sequences as implying warmer conditions than the MIS 2 and 6 glaciations, due to the lack of the "cold and fresh" indicator species, and infers that this further implies significantly wetter conditions during MIS 8 and 10 to maintain observed lake stands in the face of increased evaporation. The Devils Hole record shown in Figure 2-1 suggests that the oxygen isotope ratio deviated approximately 20 percent more from the penultimate interglacial during MIS 8 and 10 than during MIS 6. There are a number of factors that affect the isotope signal, including evaporation and the isotopic composition of the source waters, but all else being equal, the implication is that recharge had a colder signature during MIS 8 and 10 than during MIS 6. If MAT was indeed cooler, with the corresponding drop in evapotranspiration, the lack of evidence for mountain glaciers and the generally shallow Owens Lake imply that the MIS 8 and 10 stages must have been significantly drier than MIS 6. In either case, mean annual infiltration (MAI)[4] at Yucca Mountain was probably less during MIS 8 and 10 than during MIS 6 and 2,4.

2.3 OCCYM Model

The OCCYM model, which provides an independent approach to estimating potential future climatic sequences, shares some characteristics with the Sharpe (2003) model, but differs in others. The OCCYM model is driven by orbital change like the Sharpe (2003) model, but the translation process between orbital parameters and Yucca Mountain climate is significantly different.

[4]Mean annual infiltration is referenced frequently throughout this chapter. The acronym MAI will be used.

2.3.1 Ice Volume Model

The OCCYM model diverges from the Sharpe (2003) model by explicitly estimating global ice volume using a numerical model. The ice volume model is an ordinary differential equation, not physically based, that uses the Milankovitch insolation forcing (i.e., summer-solstice insolation at 65° N latitude) to drive changes in ice volume. Insolation is estimated using a computer program developed by Roper (2003) that is based on the model by Berger and Loutre (1991). A detailed description of the ice volume model is provided in Appendix A. Anthropogenic effects are not considered in the ice volume model.

There are a number of parameters that may be used to tune the model output. The optimal set of parameters in the model are a result of tuning to observed global signatures of ice volume over the past 800,000 years, using ice cores and the Devils Hole vein calcite record. The values of the parameter set are not unique, and a range of values may provide nearly identical model outputs. A set of potential ice volume sequences were generated by varying two key parameters, I_0 and I_3 (described in Appendix A), that prescribe how climate states switch from interglacial to glacial conditions. The I_0 and I_3 parameters have nominal values of -0.75 and 1, respectively. The ice volume sequences are compared to the Devils Hole and SPECMAP records in Figure 2-4(a), with all sequences normalized to their respective minimum and maximum values over the past 800,000 years. The ice volume model captures some of the larger volume changes reasonably well, but appears to be overly sensitive to smaller effects. There is little reason to favor one parameter set over another, as all sets are essentially identical in this interval; thus the parameter sets may be considered equally likely.

The set of modeled ice volume sequences are compared to the Devils Hole and SPECMAP records in a different way in Figure 2-4(b). The interval from 568,000 to 60,000 years before present is extracted from each sequence, giving a common record to compare; this shorter record is normalized, then plotted as a cumulative fraction. The modeled ice volume sequences are intermediate between the two proxy records. Even though the model does not perfectly describe either proxy record, the model reasonably captures the frequency of ice volume states.

Figure 2-5(a) shows that different parameter sets yield almost indistinguishable results for more than one-third of the next 1 million years. Again, the ice volumes are normalized to the interval from 568,000 to 60,000 years before present. The different parameter sets disagree significantly over the next 300,000 years, particularly from approximately 100,000 to 300,000 years in the future (see Figure A–9 in Appendix A). The disagreement may be due to the unusually low eccentricity during this period, which will send a weaker signal for climate change than occurred in the prior 800,000 years.

The cumulative frequency distribution for each OCCYM ice volume sequence during the next 1 million years is plotted in Figure 2-5(b). Unlike the previous 800,000 years, there is a spread of estimates for the next 1 million years. The model estimates are all shifted towards somewhat greater ice volumes in the next 1 million years relative to the past 800,000 years. In contrast, the Sharpe (2003) estimates discussed in Section 2.1 show full-glacial periods occurring a slightly smaller fraction of time during the next 1 million years, but otherwise the Sharpe (2003) estimates have almost identical statistics for the past and future periods.

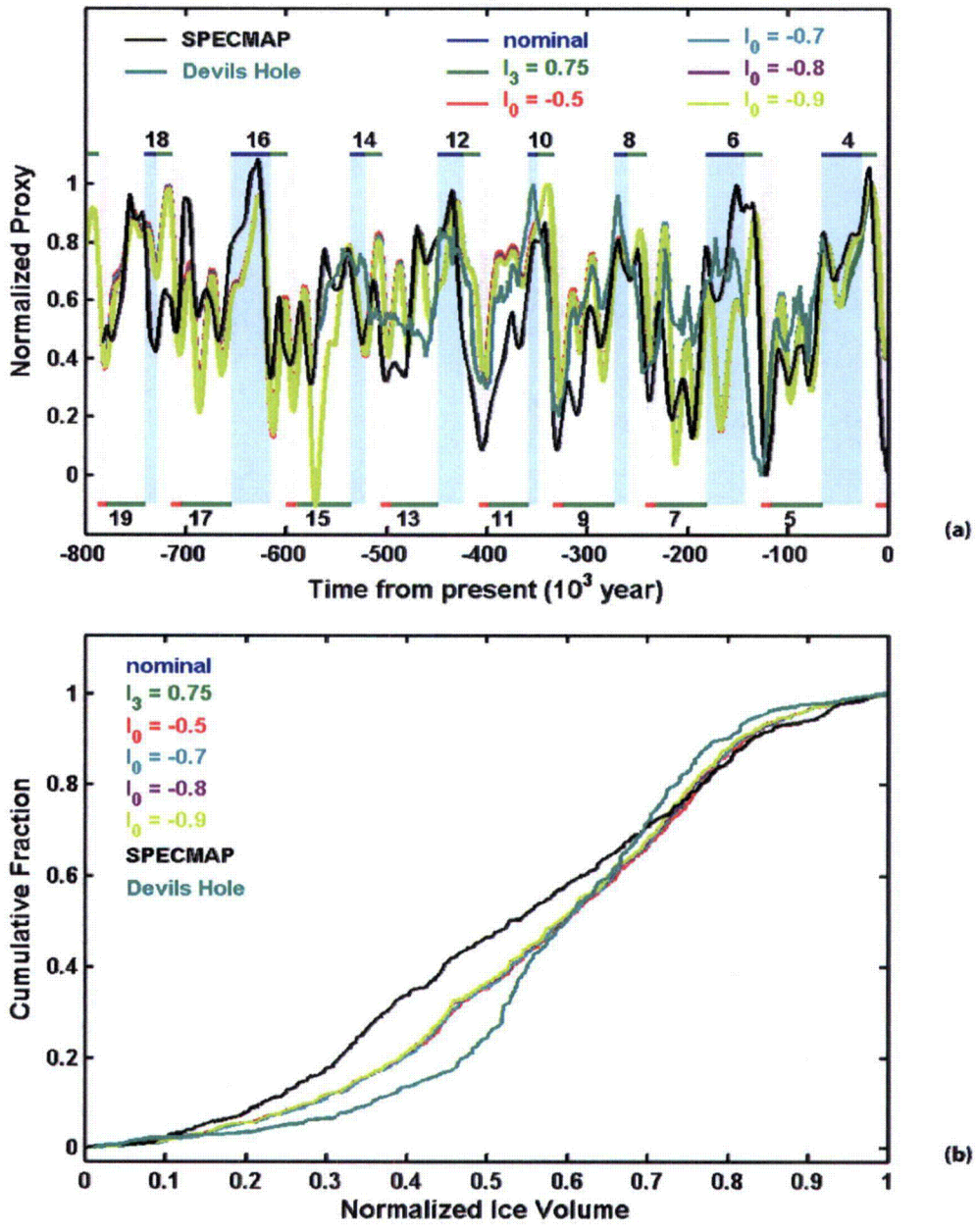

Figure 2-4. Estimated Ice Volumes and Proxy Indicators for Past Glacial States. All Values Are Normalized Using Extremes From 568,000 to 60,000 Years Before Present. (a) Time Sequences, With the Corresponding Sharpe (2003) State Sequence Provided for Reference. (b) Cumulative Fraction, With Normalized Proxy Indicators From 568,000 to 60,000 Years Before Present Shown for Reference.

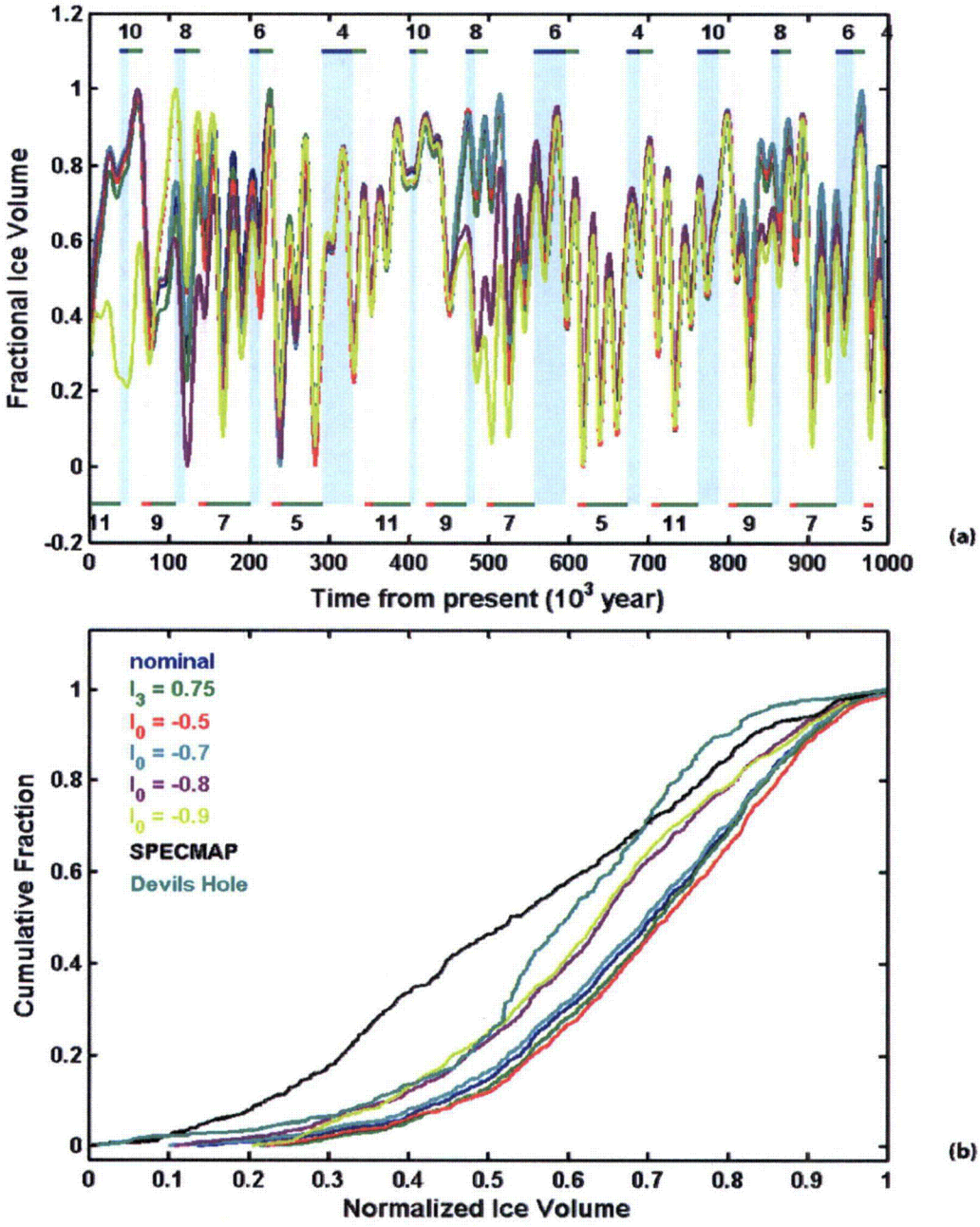

Figure 2-5. Estimated Ice Volumes Over the Next 1 Million Years. All Volumes Normalized Using Extremes From 568,000 to 60,000 Years Before Present. (a) Time Sequences, With Corresponding Sharpe (2003) States Provided for Reference. (b) Cumulative Fraction, With Normalized Proxy Indicators From 568,000 to 60,000 Years Before Present Shown for Reference.

2.3.2 Climate-Change Model

The orbital-scale climate-change model is explicitly linked to the ice volume model, based on rationale that the presence of a continental ice sheet deflects atmospheric patterns. The orbital-scale model does not account for climatic variability at scales less than approximately 10,000 years. Climatic variability at these shorter time scales is accounted for with the infiltration model, as described in Section 3.5.

As a first approximation, MAT is assumed to vary linearly with continental ice volume, based on the assumptions that (i) MAT varies roughly linearly with latitude at a given longitude, (ii) MAT at the equator changes little over glacial cycles {Lea, et al. (2000) present evidence that surface seawater temperatures in the tropics may have been cooler by 2.8 ± 0.7 °C [5.0 ± 1.3 °F] during the last glacial maximum}, (iii) MAT at the edge of the continental ice sheet changes little over glacial cycles, and (iv) the edge of the continental ice sheet moves proportionately to total ice volume. The expansion of an ice sheet implies that the temperature gradient between the equator and pole becomes steeper; hence the temperature at Yucca Mountain becomes colder. The two points used for the interpolation are determined from the interglacial estimates and the MIS 6/16 full glacial conditions.

As a first approximation, MAP is assumed to vary loglinearly with continental ice volume. The rationale for this approximation is that a moderate expansion of the continental ice sheet would tend to deflect the jet stream equatorward, bringing additional storms to the Yucca Mountain area and increasing MAP. Further deflection would tend to bring polar air masses over Yucca Mountain, reducing MAP because polar air masses are too cold to carry large amounts of moisture. However, there is little firm evidence to support the hypothesis that ice sheets expanded sufficiently to reduce MAP as far south as Yucca Mountain.

Monsoonal conditions are not considered in the OCCYM climate model. Monsoonal conditions are fostered by strong summer insolation in the northern hemisphere, which warms the interior of the continent and induces atmospheric circulation patterns that bring moisture from the Gulf of Mexico and the Gulf of California over the continent. Monsoonal conditions may be most prevalent during interglacials, tend to last only a few thousand years, and occur during only a small percentage of a glacial cycle. As is discussed in Section 3, summer precipitation is significantly less efficient at inducing recharge than winter precipitation; thus a large increase in summer precipitation may result in only a modest increase in overall recharge. Monsoonal conditions also tend to be associated with warmer values of MAT, which further reduces recharge. All of these factors suggest that neglecting monsoonal conditions may not strongly affect long-term-average conditions. A sensitivity study in Section 4 further suggests that long-term-average is rather insensitive to the precise value of MAI during low-MAI interglacial and monsoon periods.

2.3.3 Present-Day MAP Uncertainty

Uncertainty in present-day MAP results from the relatively short period of record and the relatively few meteorologic stations at Yucca Mountain. This uncertainty is independent of the uncertainty regarding regional climate change, and the OCCYM model considers it separately.

Table 2-1 lists a number of regression relationships between MAP and elevation that have been developed for the Yucca Mountain region. The coefficients in Table 2-1 cast these relationships into the form

$$\log P = A + BZ \tag{2-3}$$

where P is MAP [mm/yr], Z is elevation [km], and A [unitless] and B [1/km] are fitting coefficients. As shown in Figure 2-6, these relationships form an envelope of estimates that are in reasonably good agreement with stations on and near Yucca Mountain.

OCCYM describes uncertainty in present-day MAP by identifying values for A and B that yield a relationship falling in the middle of the envelope, with A considered uncertain and B considered known. The equation is

$$\log P = A_o + B_o Z + \Delta A \tag{2-4}$$

where A_o [unitless] and B_o [1/km] are the coefficients for the middle of the envelope and ΔA [unitless] represents the uncertainty in A.

The band shown in Figure 2-6 represents the uncertainty in present-day MAP used for calculations presented in Sections 2.4 and 4.1. The OCCYM Middle coefficients listed in Table 2-1 are used for A_o and B_o, and the range in ΔA is equivalent to multiplying the base MAP

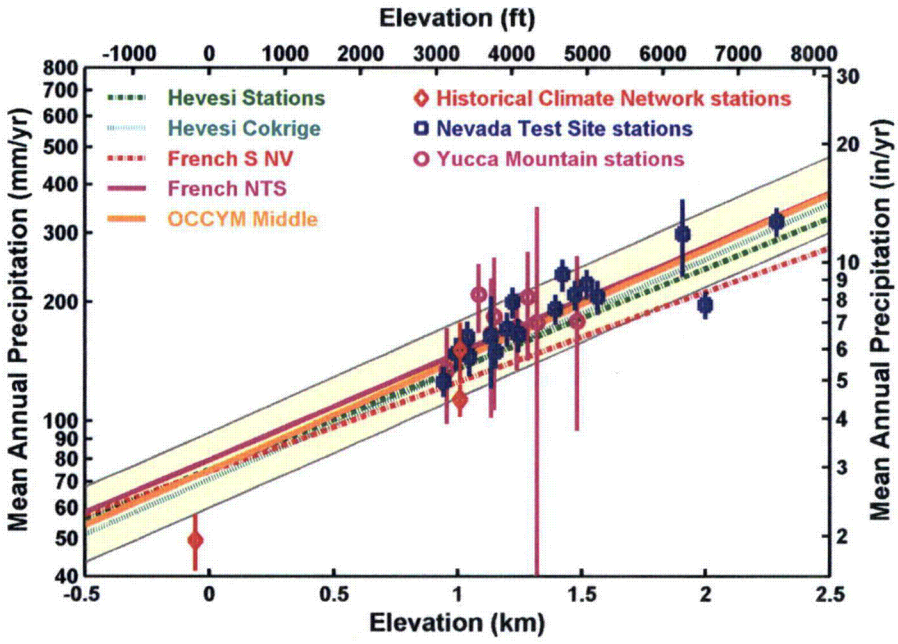

Figure 2-6. Several Regression Equations for the Elevation Dependence of MAP at Yucca Mountain

Table 2-1. Relationships Describing the Variation of Log (MAP) With Elevation in the Yucca Mountain Region			
A*	**B* [1/km]**	**Label**	**Description**
1.876	0.256	Hevesi† Stations	Regional meteorological stations only
1.850	0.281	Hevesi‡ Cokrige	Regional meteorological stations with cokriged elevations
1.872	0.228	French NTS§	Southern Nevada meteorological stations
1.902	0.271	French NTS§	Nevada Test Site meteorological stations
1.875	0.281	OCCYM Middle‖	DOE model for distributing MAP on Yucca Mountain

*Coefficients A and B assume that MAP is in units of mm/yr
†Hevesi, J.A., J.D. Istok, and A.L. Flint. "Precipitation Estimation in Mountainous Terrain Using Multivariate Geostatistics: Part II—Isohyetal Maps. *Journal of Applied Meteorology.* Vol. 31 (7). pp. 661–676. 1992a.
‡Hevesi, J.A., A.L. Flint, and J.D. Istok. "Precipitation Estimation in Mountainous Terrain Using Multivariate Geostatistics: Part I—Isohyetal Maps. *Journal of Applied Meteorology.* Vol. 31 (7). pp. 677–688. 1992b.
§French, R.H. "Daily, Seasonal, and Annual precipitation at the Nevada Test Site, Nevada." Publication No. 45042. Reno, Nevada: Desert Research Institute. 1986.
‖Bechtel SAIC Company, LLC. "Technical Basis Document No. 1: Climate and Infiltration." Las Vegas, Nevada: Bechtel SAIC Company, LLC. 2004c.

by 4/5 to 5/4 (i.e., ΔA ranges from -0.0969 to 0.0969). The OCCYM Middle relationship is simply Eq. 2-1 transformed into the format of Eq. 2-3. The ΔA parameter is described with a triangular probability distribution in Sections 2.4 and 4.1.

2.3.4 Present-Day MAT Uncertainty

Uncertainty in present-day MAT results from the relatively short period of record and the relatively few meteorologic stations at Yucca Mountain. Present-day MAT is affected by elevation, usually cooling with increasing elevation, but MAT is affected by temperature inversions, differential wind-induced mixing, and topography-induced redistribution across the site. This uncertainty is independent of the uncertainty regarding regional climate change, and the OCCYM model considers it separately.

Atmospheric temperature observations are only available at Yucca Mountain since the 1980s, from the onset of Yucca Mountain site characterization. Atmospheric temperature observations also have been made on the Nevada Test Site since the 1980s. The National Weather Service maintains an extensive network of meteorological stations across the United States, and daily summaries of temperature extremes are available for hundreds of Cooperative Observer Program (COOP)[5] stations in Nevada and surrounding states.

[5]Cooperative Observer Program stations are referenced frequently throughout this chapter. The acronym COOP will be used.

Daily temperature-extreme records, from station inception through 1997, were obtained for the network of COOP stations run by the National Weather Service in Arizona, California, Nevada, and Utah. These data are available on CD-ROM from the National Climatic Data Center web site (www.ncdc.noaa.gov). A reduced set of stations was obtained by restricting the analysis to include all Nevada stations, all Utah stations west of longitude W 113°, all Arizona stations west of longitude W 113° and north of latitude N 35°, and all California stations east of longitude W 118.2° and north of latitude N 34.5° (north of the San Gabriel mountains and east of the crest of the southern Sierra Nevada). All stations in Inyo and Mono counties of California were also explicitly included. The boundaries include at least a 2-degree buffer on every side of Yucca Mountain. A total of 262 stations were considered, all with record lengths more than 5 years.

Table 2-2 lists regression relationships between MAT, elevation, and normalized latitude based on the 262 regional COOP stations. These relationships are for mean annual daily maximum, daily mean, and daily minimum temperature. The regional relationships have the form

$$T = A + BZ + CN \tag{2-5}$$

where T denotes mean annual daily mean, daily maximum, or daily minimum temperature [° C]; Z is elevation [km], N is latitude normalized from 0 at latitude N 34° to 1 at latitude N 42°; and A, B, and C are fitting coefficients. Corresponding relationships using mean annual insolation have similar explanatory power, as mean annual insolation on a horizontal plane outside the atmosphere varies essentially linearly with latitude in this zone.

Note that maximum daily temperature is described better than minimum daily temperature with these regressions, reflecting the stronger influence of insolation on maximum temperature relative to minimum temperature.

Table 2-2. Relationships Describing the Variation of MAT With Elevation in the Yucca Mountain Region

A [°C]	B [°C/km]	C [°C]	R^2	Description
24.30	-6.340	-6.861	0.95	Regional mean daily temperature
21.87	-6.340			Mean daily temperature at Yucca Mountain
32.93	-6.856	-5.828	0.97	Regional maximum daily temperature
30.87	-6.856			Yucca Mountain Maximum daily temperature at Yucca Mountain
15.67	-5.824	-7.895	0.84	Regional minimum daily temperature
12.87	-5.824			Minimum daily temperature at Yucca Mountain

°F = (9/5)°C+32
1 km = 3281 ft

Each regional relationship in Table 2-2 is localized to Yucca Mountain by adding the local value of *CN* at Yucca Mountain to the *A* coefficient. The resulting equation has the form

$$T = A + BZ \quad (2\text{-}6)$$

where *A* includes *CN*. Yucca Mountain has an approximate latitude of N 36° 50', so *N* is set to 0.354 when localizing the regional relationships. Table 2-2 also lists regression relationships between MAT and elevation based on 25 Nevada Test Site stations with record lengths of at least 10 years. The stations systematically increase in elevation moving from south to north, but the latitude correction is not incorporated because the stations have such similar latitude. Again daily maximum is described better than daily minimum. The final set of regression relationships presented in Table 2-2 were developed from Yucca Mountain stations using measurements in 1992 (Bechtel SAIC Company, LLC, 2004c).

The set of regression relationships are plotted in Figure 2-7, as well as observations both from the Nevada Test Site and from Yucca Mountain. The regional and Nevada Test Site regression relationships agree very well for daily maximum temperature, are somewhat dissimilar for daily minimum temperature, and are reasonably similar for mean annual temperature. The Bechtel SAIC Company, LLC (2004c) relationship for MAT is warmer by approximately 3 to 5 °C [5 to 9 °F] than the more regional relationships. Each Yucca Mountain observation falls between the Bechtel SAIC Company, LLC (2004c) relationship and the regional relationships. Observed minimum daily temperatures at Yucca Mountain all fall in the warm end of regional observations, without a strong elevation dependence, whereas maximum daily temperatures are typical of regional patterns.

OCCYM uses two relationships to describe elevation-dependent Holocene-average MAT across Yucca Mountain. Both relationships are based on the regional relationship for MAT using the 262 COOP stations. The warmer base relationship adds an offset to the regional relationship to match the highest Yucca Mountain station (on Yucca Crest) to represent present-day MAT, then assumes that average late-Holocene MAT was uncertain in the range of 0 and 2 °C [0 and 3.6 °F] warmer than present. The highest station is closest to the reference elevation of 1,524 m [5,000 ft] used to relate regional information to Yucca Mountain. The reference MAT at this elevation is 15.7 °C [60.3 °F]. The base relationship is indicated by a shaded parallelpiped in Figure 2-7.

Further examination of the temperature observations suggested that the highest station may be anomalously warmer than Yucca Mountain as a whole, so a second relationship was defined to assess the effect of small differences in present-day MAT. The cooler relationship adds an offset to the regional relationship so that the maximum deviation between Yucca Mountain observations and regression is approximately equal above and below the regression line, yielding MAT of 14.4 °C [57.9 °F] at the reference elevation. The cooler relationship further assumes that there is an uncertainty of 0.5 °C [0.9 °F] above and below the present-day relationship. The second relationship also assumes that on average the late Holocene was between 0 and 2 °C [0 and 3.6 °F] warmer than at present, so that the overall uncertainty is between -0.5 and 2.5 °C [-0.9 and 4.5 °F] relative to the present-day relationship. This second relationship is indicated by a black parallelpiped in Figure 2-7. The second relationship is considered in Section 4.1.

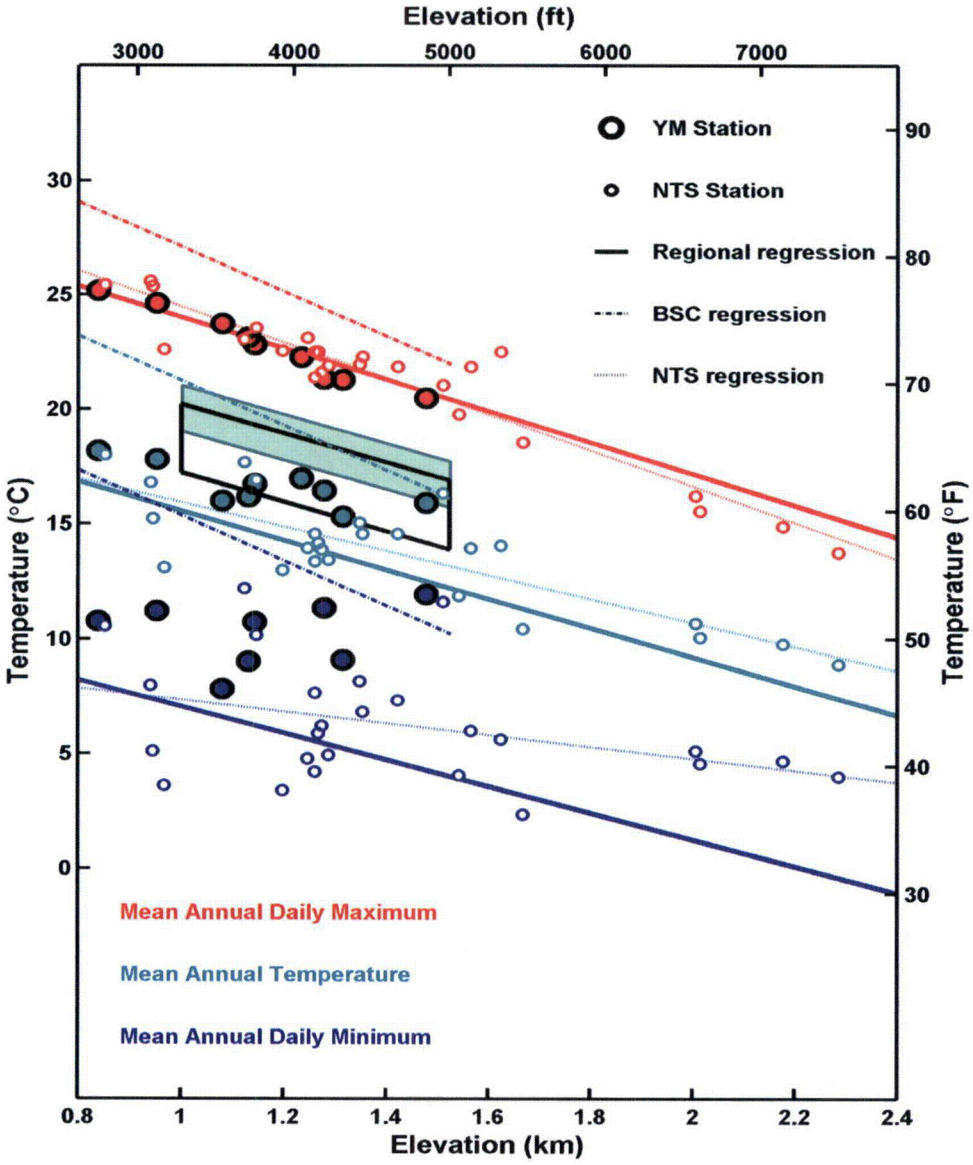

Figure 2-7. Several Regression Equations for the Elevation Dependence of MAT at Yucca Mountain. Mean Annual Daily Maximum and Minimum Temperature Are Shown For Reference. The Shaded Box Denotes the OCCYM Nominal Interglacial Case and the Outlined Box Denotes the OCCYM Cool Interglacial Case.

2.4 Probability Distributions for Long-Term Averages

The future climate at Yucca Mountain will be both temporally variable and uncertain. On top of climatic variability and uncertainty, the value of MAI given a climatic condition is uncertain. To combine these effects into statistical distributions of long-term-average MAP, MAT, and MAI, the OCCYM model defines MAP and MAT pairs, with fixed probabilities, that are used to integrate MAI over time using the OCCYM ice volume sequences. Three independent sources of future-climate uncertainty are considered: (i) uncertainty in which ice volume sequence is correct (Section 2.3.1), (ii) uncertainty in the link between ice volume and climate change (Section 2.3.2), and (iii) uncertainty in present-day MAP (Section 2.3.3).

The probability distributions for long-term-average MAP, MAT, and MAI are represented by cumulative probability distributions similar to the curves shown in Figures 2-4(b) and 2-5(b). These distributions are calculated in stages.

In the first stage, reference interglacial and full-glacial climates for reference ice volumes are determined, with each ice volume sequence normalized using its extremes for the period from 568 to 60 thousand years. The OCCYM model determines the climate for any given ice volume by linearly interpolating MAT and loglinearly interpolating MAP as a function of ice volume, using the reference states.

The full-glacial-maximum endpoint climate is based on the MIS 6 state described in Section 2.2.3, with a range in MAP of 1.8 to 2.3 times present-day MAP and a range in MAT reduction of 6.9 to 9.7 °C [12.4 to 17.5 °F] . The interglacial endpoint climate is based on present-day conditions, with present-day millennial-scale MAP assumed uncertain with an estimate of 1 to 1.2 times present-day MAP and present-day MAT within ±1°C [±1.8 °F]. The upper limit in present-day millennial-scale MAP is the average MAP of the bristlecone pine record analyzed in Section 3.5, using moving averages over the last 1,000 years.

Unfortunately, the numerical model for ice volume in OCCYM does not always match the proxies. The ice volume model appears to undershoot during the Holocene relative to previous interglacial periods, but peaks of full glacial periods are better captured. Because of the uncertainty in numerical model results, three representative normalized ice volumes are used to represent the interglacial endpoint, with normalized ice volumes of 0 (representative of the lowest model extreme in the calibration period), 0.4 (representative of the model value for the present), and 0.2 (the average of the two). The nominal value for interglacial conditions is 0.2, splitting the difference.

In the second stage, probability distributions for the endpoint climates are determined. The OCCYM model assumes that endpoint MAT and A_o are uniformly distributed within their respective bounds. The joint probability distribution is partitioned into a grid with N_p values for A_o and N_t values for MAT. These grid points are used to define the corners of grid blocks. Each block is assigned the average value for A_o and MAT from the four corners, and is assigned a probability of $1 / [(N_p - 1)(N_t - 1)]$.

In the third stage, the average value of MAP, MAT, or MAI for each ice volume sequence is integrated from present to 1 million years in the future for each of the endpoint grid blocks. Each integral has the form

$$\overline{x} = \frac{\int_0^T x\,dt}{\int_0^T dt} \tag{2-7}$$

where x represents MAP, MAT, or MAI; t is time; and T is the final time (1 million years). Each integral has equal probability P_i, where $P_i = N_v (N_p - 1) (N_t - 1)$ and $N_v = 6$ is the number of ice volume sequences. Each integration uses matching grid blocks, so that one integration is always hot and dry, another is always cool and wet, and so forth. A climate is determined for each thousand-year segment by loglinearly interpolating MAP and linearly interpolating MAT between endpoint states.

In the final stage, the cumulative probability distribution over all of the integrals is calculated by sorting the integrals from lowest to highest value.

The procedure is modified slightly when integrating MAP or MAI, because Yucca Mountain MAP is uncertain for any given regional climate. Each of the A_o values in the endpoint grid blocks is associated with a triangular probability distribution for ΔA. The triangular probability distribution for ΔA is discretized into N_d blocks with appropriate probability, and a total of $N_v (N_p - 1) (N_t - 1) N_d$ integrals are calculated. In this case, there are as many as N_d different probability values for the different integrals, which are taken into account when assembling the cumulative probability distribution.

Estimating MAI creates one additional complexity, because there is a probability distribution for MAI given a climate state. The probability distribution for MAI, which is independent of climate and is described in Section 3, is handled just like the ΔA distribution. The MAI probability distribution for each climate state is divided into N_i equal-probability bins, with each bin integrated separately, for a total of $N_v (N_p - 1) (N_t - 1) N_d N_i$ integrals.

An analogous approach is followed when estimating probabilities using the Sharpe (2003) climate states. In this case, $N_v = 1$ (just one set of states), $N_d = 1$ (MAP uncertainty and climate uncertainty are merged), and $N_t = 6$ (for the six climate states), but each state has a different frequency.

The median value for MAP, MAT, and MAI is simply the value where the cumulative frequency is 0.5. The expected value for MAP, MAT, and MAI is calculated from a set of N integrals using the formula

$$\mu_x = \sum_{i=1}^{N} P_i x_i \tag{2-8}$$

where μ_x is the expected value of x; x_i represents long-term-average MAP, MAT, or MAI from integral i; and P_i is the probability associated with integral i. The standard deviation σ_x is calculated using the formula

$$\sigma_x = \left[\sum_{i=1}^{N} P_i (x_i - \mu_x)^2 \right]^{1/2} \quad (2\text{-}9)$$

Figure 2-8 shows the MAP and MAT cumulative probability distributions for the Sharpe (2003) and OCCYM models at a reference elevation of 1,524 m [5,000 ft]. The models have generally similar distributions, with the Sharpe (2003) model in the dry end of the OCCYM models for MAP but in the cooler end of the OCCYM models for MAT. The rounded distribution extremes in the OCCYM model are a result of the triangular probability distribution for local MAI uncertainty, which is not explicitly included in the Sharpe (2003) model.

2.5 Summary

The overall Sharpe (2003) model is based on work by Forester, et al. (1999); Thompson, et al. (1999a); and Bechtel SAIC Company, LLC (2004a). The Sharpe (2003) model was modified for this report to represent interglacial MAP and MAT using the models of Bechtel SAIC Company, LLC (2004c). Independent estimates of climates during past glacial states are somewhat drier and warmer than the Sharpe (2003) model for intermediate and full glacial climatic states.

An independent model for orbital-cycle climate at Yucca Mountain, developed from the literature, considers the dynamics of global ice volume as forced by changes in insolation. This model suggests that the next 1 million years may have a somewhat greater average global ice volume than the past 800,000 years. The OCCYM model combines climatic uncertainty with time histories of global ice volumes estimated by the ice volume model to yield a set of climatic states with associated probability levels. The sequences of ice volumes (for the OCCYM model) or glacial states [for the Sharpe (2003) model] are used to integrate MAP, MAT, and MAI over the next 1 million years.

These climate states are combined with the models for net infiltration derived in Section 3 to provide estimates of long-term-average net infiltration in Section 4.

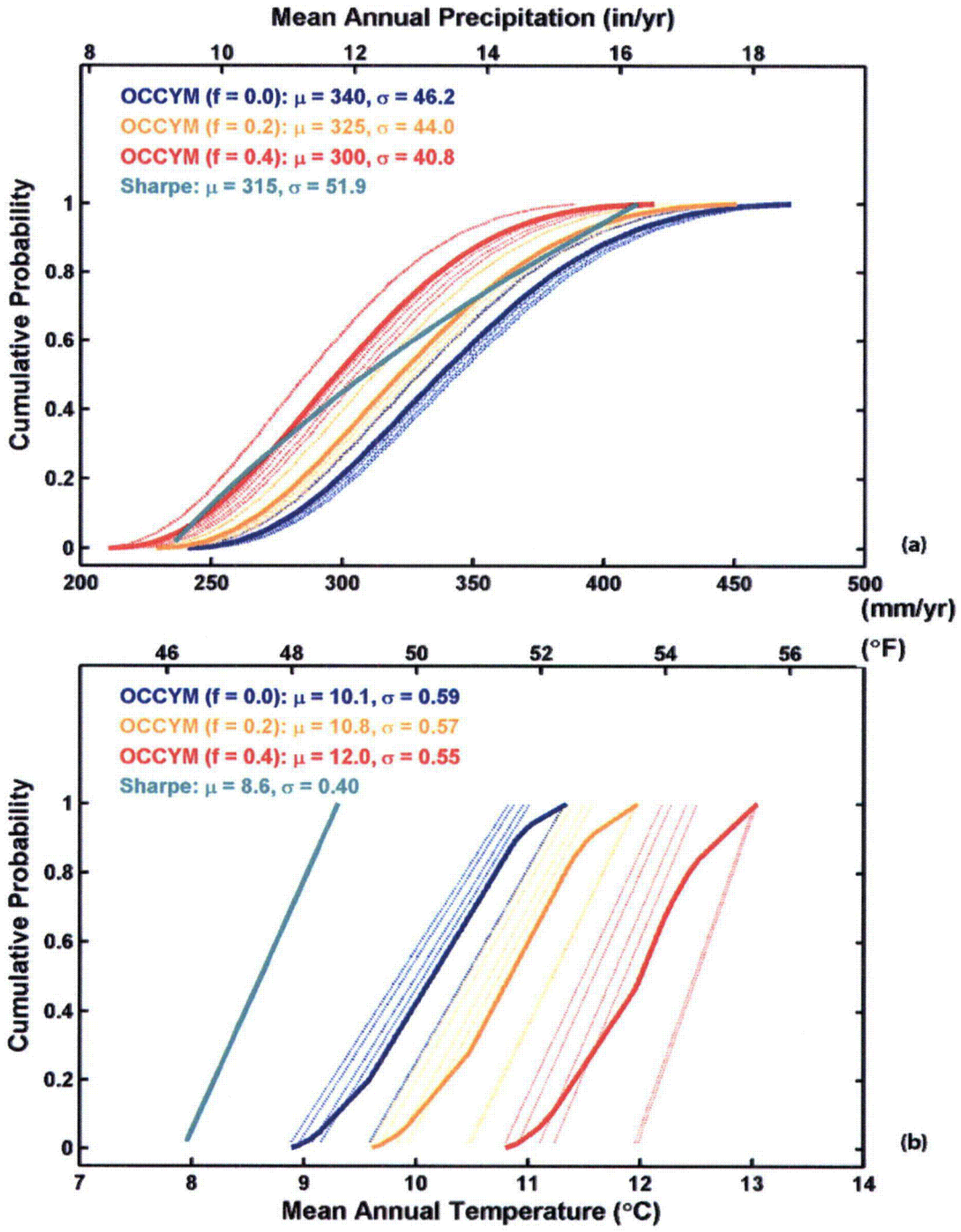

Figure 2-8. Cumulative Probability Distribution for (a) MAP Using N_p = 50, N_t = 1, and N_d = 11 and (b) MAT Using N_p = 1, N_t = 50, and N_d = 1

3 INFILTRATION FROM CLIMATE

Two descriptions for areal-average net infiltration are developed in this section. Estimates of Decadal-Scale Footprint Box Infiltration (Decadal Infiltration) characterize areal-average decade-average net infiltration over a representative decade in a rectangular region bounding a potential repository footprint. The Decadal Infiltration estimates account for variability at time scales below a decade and spatial scales below the footprint scale, compactly summarizing the results of numerous field, laboratory, and numerical investigations. The Decadal Infiltration estimates are scaled up to Millennial-Scale Footprint Box Infiltration estimates (Millennial Infiltration results). The Millennial Infiltration results are used in Section 4 to estimate the response of footprint-average net infiltration to climate change at time scales determined by orbital forcings. Sources of data discussed in this section are referenced in Appendix C.

3.1 Background and Previous Work

Net infiltration at any location is ultimately driven by precipitation (rain and snow), as modified by lateral redistribution and evapotranspiration. Overland flow and moisture redistribution within the soil column can be sensitive to precipitation patterns over time scales of minutes to hours, while evapotranspiration rates vary over each day. However, the magnitude of pulses in water flux due to infiltration events decreases rapidly with depth in a column, and recharge may only respond to annual or decadal variation in net infiltration in parts of the arid American West with thick vadose zones.

As discussed by Stothoff and Musgrove (2006), most studies related to arid-zone infiltration are at small plot or hillslope scales, typically considering only the top few meters of the soil column for a period of weeks to years, or at large basin scales, typically considering many watersheds over years to decades. Yucca Mountain is unusual among hydrologic studies, because neither near-surface fluxes nor recharge fluxes are of the most direct interest. Instead, percolation fluxes midway between the surface horizon and the water table are of the most direct interest, particularly the fluxes in the lower 250 m [820 ft] vadose zone between the repository horizon and the water table. The spatial scale considered at Yucca Mountain is also unusual among hydrologic studies, intermediate between typical small-scale infiltration studies and typical hydrologic basin studies. The repository footprint is approximately 13 km^2 [5 mi^2] with numerous small watersheds above the footprint, while Nevada hydrologic basins range from 23 to 7,578 km^2 [9 to 2,926 mi^2].

The classical approach to modeling spatially distributed net infiltration in a watershed uses a horizontal grid of cells to represent the ground surface. Typically each cell contains a vertical stack of several layers, partitioning soil and bedrock into compartments. During a precipitation event, water moves from the surface into deeper soil layers, and water exceeding infiltration capacity is routed from cell to cell as overland flow. Vertical movement continues after precipitation ends, and in some models water is also allowed to redistribute as subsurface lateral flow. This approach can be extremely computationally demanding at the Yucca Mountain scale, because tens to hundreds of thousands of cells may be considered simultaneously, and decades of simulations may be necessary to properly capture the expected range of precipitation events.

The U.S. Geological Survey/U.S. Department of Energy (DOE) approach to simulating net infiltration at Yucca Mountain is described by Bechtel SAIC Company, LLC (2004b). The U.S. Geological Survey/DOE [Bechtel SAIC Company, LLC (2004b)] (BSC04)[1] model is based on the classical approach, using a horizontal mesh with square cells 30 m [98 ft] on a side to describe a domain of 123.7 km^2 [47.8 mi^2]. Daily timesteps are used to step through 50 to 100 years, with daily climatic inputs derived from meteorologic stations that are analogs to particular climate states. A typical cell has three soil layers and a bedrock layer. During precipitation events, infiltration excess (precipitation that cannot be absorbed by the soil) is assumed to run off to a downslope cell, but each cell is considered independently when neither precipitation nor runoff is occurring. The model is further partitioned into a number of independent watersheds to reduce the computational burden. Bechtel SAIC Company, LLC (2004b) combined a total of nine simulations to represent infiltration under several potential future climatic states at Yucca Mountain.

CRWMS M&O (2003b) used 100 realizations of 12 uncertain input parameters, including precipitation- and evapotranspiration-affecting parameters, to assess infiltration uncertainty for one reference climate. These simulations used a weather sequence from Tule Lake, in northern California near the Oregon border, as an analog climate for intermediate glacial conditions. The cumulative frequency distribution for the areal-average recharge fraction [mean annual infiltration (MAI)[2] divided by mean annual precipitation (MAP)[3]] from the 100 realizations is shown in Figure 3-1.

Figure 3-1 compares a lognormal distribution constructed using the mean and variance of the log-transformed set of realizations to the 100 realizations. The lognormal distribution captures some characteristics of the cumulative frequency distribution estimated from the CRWMS M&O (2003b) model, but the lognormal distribution has a higher proportion of high-recharge values and a lower proportion of low-recharge values.

3.2 Infiltration Tabulator for Yucca Mountain (ITYM)[4] Model Description

The ITYM model is a preprocessor code for the TPA code used in U.S. Nuclear Regulatory Commission (NRC) performance assessments. The ITYM model tabulates areal-average MAI as a function of decade-average MAP and MAT and accounts for uncertainties in hydraulic parameters. The ITYM model is briefly described in this section. Appendix B provides a more detailed description of the model and input parameters. A complete description of the ITYM model and inputs will be the topic of the next report in the series.

---

[1]The U.S. Geological Survey/DOE [Bechtel SAIC Company, LLC (2004b)] model is referenced frequently throughout this chapter. The acronym BSC04 will be used.

[2]Mean annual infiltration is referenced frequently throughout this chapter. The acronym MAI will be used.

[3]Mean annual precipitation is referenced frequently throughout this chapter. The acronym MAP will be used.

[4]The Infiltration Tabulator for Yucca Mountain module is referenced frequently throughout this chapter. The acronym ITYM will be used.

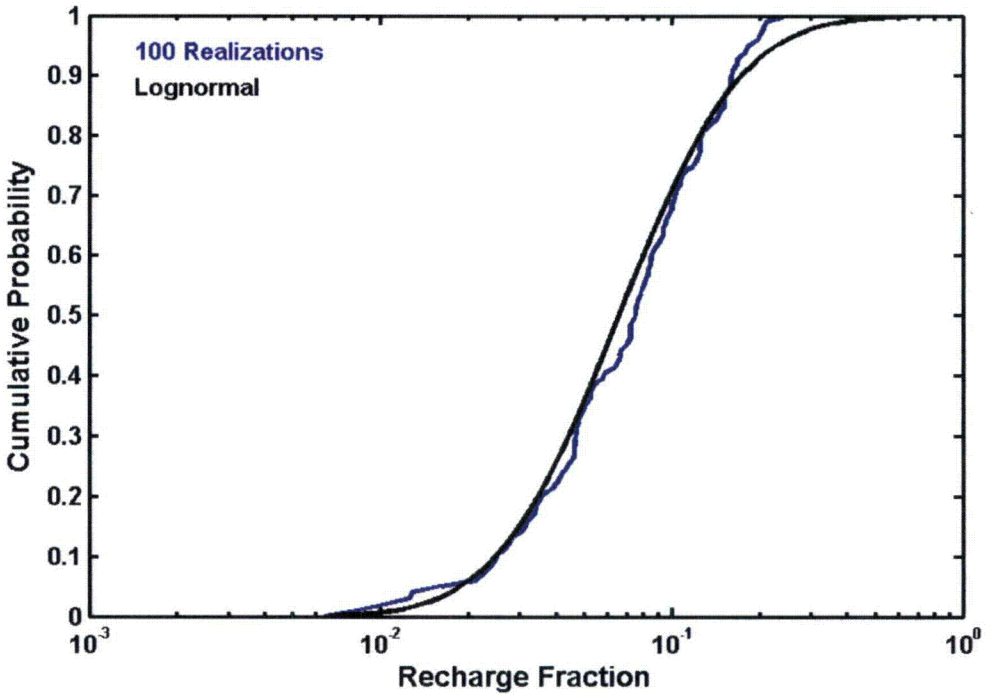

Figure 3-1. Cumulative Probability Distribution for Tule Lake Realizations and a Comparison Lognormal Distribution. There Are 100 Realizations of Areal-Average Net Infiltration With 12 Uncertain Input Parameters Using the CRWMS M&O (2003b) Model With a Weather Sequence From Tule Lake, California. The Lognormal Distribution Has the Same Mean and Standard Deviation as the 100 Realizations.

The ITYM model describes the same physical system as the BSC04 model, but the methods and assumptions that are used to calculate net infiltration are quite different than those in the BSC04 model. Unlike the BSC04 model, the input parameters in ITYM are considered uncertain, and this uncertainty is explicitly incorporated into the ITYM model using Monte Carlo sampling.

Evaluating infiltration uncertainty typically requires hundreds or thousands of evaluations, which would be extremely demanding from a computational standpoint using a classical approach based on two- or three-dimensional numerical infiltration simulations. Instead, ITYM uses an abstracted representation for net infiltration derived from many one-dimensional infiltration simulations (Stothoff, 1999). This abstraction is applied on a horizontal mesh slightly offset from the mesh used for BSC04 simulations but with the same grid spacing. Like the BSC04 model, each grid cell has an associated set of parameters based on field mapping, laboratory analyses, and theoretical models.

Most parameters used in ITYM are derived from basic data obtained by the DOE program, and BSC04 model inputs are the source of many ITYM parameters that are relatively certain or that

minimally influence infiltration estimates. For example, bedrock and soil maps were obtained from the DOE program, and bedrock and soil hydraulic properties are based on BSC04 model input. Insight from independent field visits by Center for Nuclear Waste Regulatory Analyses (CNWRA) and NRC investigators to observe bedrock, soil, and vegetation characteristics at outcrops, exposures, pits, and trenches guided the selection of the remaining parameters, such as fracture hydraulic properties and soil thickness, and built confidence in the representativeness of the BSC04 soil hydraulic properties. The ITYM model for plant uptake is entirely unlike the BSC04 model. Input parameters are discussed in more detail in Appendix B.

ITYM uses a response relationship between soil and bedrock hydraulic parameters, decade-average climatic parameters, and decade-average infiltration that was developed using the BREATH code (Stothoff, 1995). The response relationship is used for each 30 by 30 m [98 by 98 ft]-square grid cell in an overall grid of 6 by 9 km [3.7 by 5.6 mi], as shown in Figure 3-2. The reference area for estimating deep percolation in this report (the Footprint Box in Figure 3-2) is a 14.7-km^2 [5.7-mi^2] rectangular subset bounding the potential repository outline, with sides of 2.7 by 5.43 km [1.7 by 3.4 mi]. The larger grid is used to estimate overland flow onto the Footprint Box. The model can only approximately represent features such as channels that may provide local areas of high infiltration but are smaller than the 30-m [98-ft]-grid block size.

The ITYM model provides a collection of grid-cell estimates that captures the relative frequency of different infiltration patterns, within the constraints of grid resolution, as well as providing reasonable spatial patterns of infiltration. Spatial averages of the model results honor the model intention and provide a transparent representation for investigating the effects of different climates. Accordingly, all ITYM results are averaged into a single measure, areal-average decadal-average MAI, and this measure is used in subsequent analyses. This averaging process scales up calculations performed at the scale of centimeters and hours into averages representative of several square miles over a decade.

The ITYM model produces output tables of MAI statistics for each grid cell, assuming that the statistical description for input parameters does not depend on decade-average MAP and decade-average MAT. Several combinations of decade-average MAP and mean annual temperature (MAT)[5] are used to describe the response of MAI to climate. For this analysis, the output tables are created for all 16 combinations of 4 fixed values of decade-average MAP and 4 fixed values of decade-average MAT at a reference elevation of 1,400 m [4,600 ft], approximately 100 m [330 ft] below the crest of Yucca Mountain (note that climate is adjusted for elevation-dependent effects within the ITYM model). Topography, upslope properties, bedrock and soil classes, and soil depth are assumed to be constant and independent of climatic condition. All other input properties are considered uncertain with the same statistical properties used for all climatic conditions. Statistical properties are explicitly considered through Monte Carlo sampling, using 2,000 realizations of all uncertain input parameters for each combination of decadal-average MAP and MAT. Note that the same ITYM results are used for NRC performance assessments as part of TPA Version 5.1.[6]

---

[5]Mean annual temperature is referenced frequently in this chapter. The acronym MAT will be used.

[6]Durham, J., C. Grossman, and B. Leslie (coords.). "Total-system Performance Assessment (TPA) Version 5.1 Code Module Descriptions and User Guide." San Antonio, Texas: CNWRA. 2007. (Unpublished).

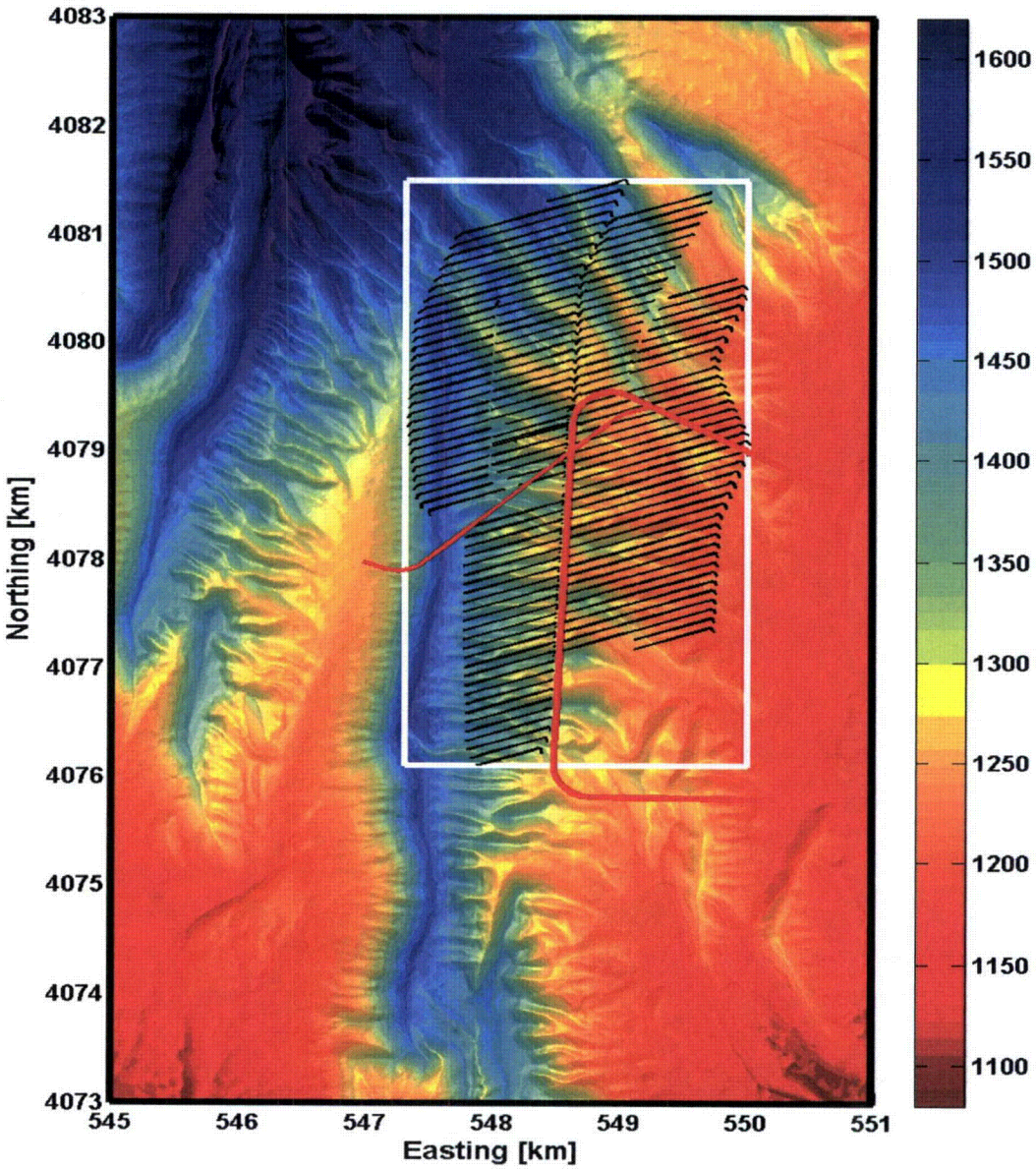

Figure 3-2. Shaded Relief Map of Yucca Mountain. Total Modeled Domain, Potential Repository Layout, and Footprint Box Used for Infiltration Estimates Are Shown. Color Scale is Elevation in Meters. Map Projection is Universal Transverse Mercator Zone 11, 1927 North American Datum. [1 m = 3.28 ft, 1 km = 0.62 mi]

3.3 Decadal Infiltration Estimates

ITYM calculates the mean and standard deviation of MAI in each grid cell, or pixel, in the domain. The ITYM estimates of decade-average net infiltration are approximately lognormally distributed in each grid cell, with the coefficient of variation decreasing as mean infiltration increases. Figure 3-3 suggests that a lognormal distribution also is a good approximation for the probability distribution of areal-average MAI over a 6 by 9-km [3.7 by 5.6-mi] area centered on Yucca Mountain. This area has 59,700 pixels. The "Lognormal from Pixels" method uses the average of the pixel statistics as an estimate of the mean and standard deviation for the areal-average MAI. The "Lognormal from Average" distribution instead uses the actual mean and standard deviation of areal-average MAI. Figure 3-3 suggests that the Lognormal from Pixels method is a good approximation to the more rigorous Lognormal from Average method, because the two methods yield almost identical distributions.

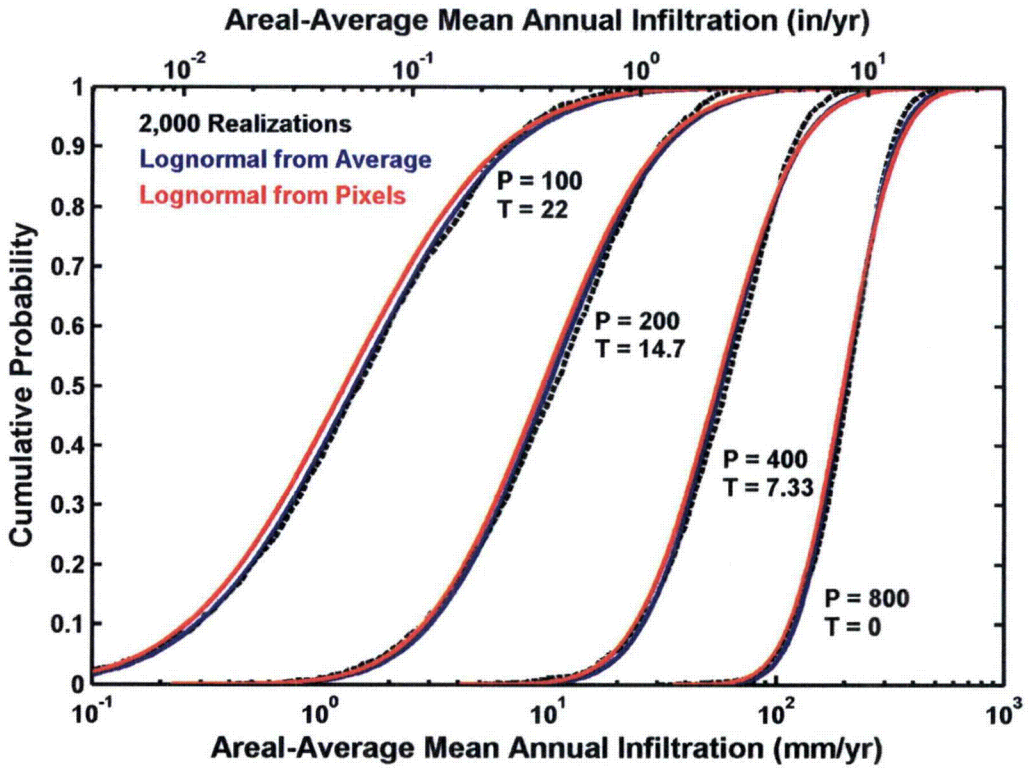

Figure 3-3. Cumulative Probability Distributions for Areal-Average MAI Under Selected Climatic Regimes. P and T Indicate Mean Annual Precipitation (mm/yr) and Mean Annual Temperature (°C) at 1,400 m Elevation, Respectively. Regardless of Climate, Areal-Average MAI From 2,000 Realizations Compares Well to Two Lognormal Distributions, One With the Same Mean and Standard Deviation as the Areal-Average Realizations and One With the Average Mean and Standard Deviation for the 59,700 Pixels. [100 mm/yr = 3.94 in/yr, °F = (9/5)°C+32]

Figure 3-3 shows that the model realizations have slightly less probability of high infiltration rates and slightly greater probability of low infiltration rates than the lognormal distribution. The CRWMS M&O (2003b) results shown in Figure 3-1 also exhibited this characteristic. A lognormal distribution is unbounded, implying that there is some small probability that areal-average MAI is nonphysically greater than areal-average MAP, as shown in Figure 3-3. Because a lognormal distribution is a reasonable description of the model results, areal-average net infiltration is described using a lognormal distribution through the remainder of the report, truncated to eliminate nonphysical extremes. All of the remaining results use grid-cell-average statistics (i.e., the Lognormal from Pixels method) to estimate areal-average decade-average infiltration, summarized for the Footprint Box in Table 3-1.

Table 3-1. Mean and Standard Deviation of Grid-Cell Estimates of MAI* in the Footprint Box Given Climate at a Reference Elevation of 1,400 m [4,590 ft]

MAP† [mm/yr]*	MAT‡ [°C]§	Mean MAI* [mm/yr]‖	Standard Deviation of MAI* [mm/yr]‖
100	0	10.2	9.58
200	0	33.3	24.2
400	0	90.4	50.4
800	0	226	95.1
100	7.33	7.04	8.17
200	7.33	23.6	21.5
400	7.33	74.3	50.8
800	7.33	197	102.9
100	14.67	4.75	6.71
200	14.67	16.1	18.1
400	14.67	52.1	45.0
800	14.67	155	103
100	22	3.09	5.64
200	22	10.9	14.6
400	22	36.1	38.5
800	22	116	94.8

*Mean Annual Infiltration (MAI)
†Mean Annual Precipitation (MAP)
‡Mean Annual Temperature (MAT)
‖100 mm/yr = 3.94 in/yr
§°F = (9/5)°C+32

These results are referred to as Decadal-Scale Footprint Box Infiltration (or Decadal Infiltration) in the rest of the report. The Footprint Box defined for this report lies between 4,076.1 and 4,081.5 km northing and 547.3 and 550 km easting using the Universal Transverse Mercator Zone 11 projection and the 1927 North American Datum. The Decadal Infiltration statistics listed in Table 3-1 are the starting point for assessing the response of infiltration to climate change in the rest of this report. These statistics scale up spatial variability in infiltration patterns below several square kilometers and scale up temporal variability at scales from minutes to years. An additional scaling procedure presented in Section 3.5 accounts for the variability of decadal-average climate over several millennia to yield the Millennial-Scale Footprint Box Infiltration statistics (Millennial Infiltration).

The median values of the Decadal Infiltration distributions are shown in Figure 3-4. By definition, half of the Decadal Infiltration estimates are larger than the median value, and half are smaller. The properties of lognormal distributions ensure that the median values are somewhat less than the mean values reported in Table 3-1. For reference, estimates of Decadal Infiltration for conditions representing present-day Yucca Mountain climate are also indicated by circles in Figure 3-4 using estimates of MAP and MAT at the reference elevation of 1,400 m [4,600 ft] obtained from several regional regressions. These represent the median value and extremes in MAP from several regional regressions. Uncertainty in Decadal Infiltration and the local climate is indicated by a filled box, indicating one standard deviation above and below the median value for both MAP and Decadal Infiltration.

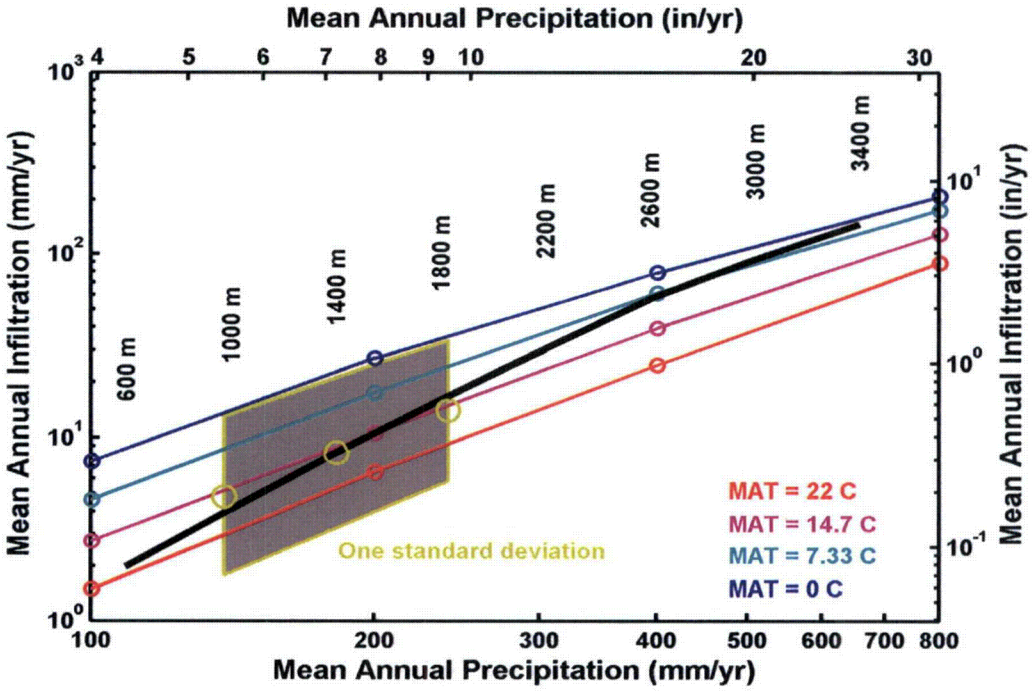

Figure 3-4. Median Values for the Decadal Infiltration Estimates. Different MAT Values Are Indicated by Color. Estimates for Present-Day MAP at the Reference Elevation Are Indicated by Yellow Circles. The Filled Area Represents the Region Within One Standard Deviation of the Median Present-Day Decadal Infiltration. The Black Curve Represents the Effect of Climate Change Equivalent to Changing Elevation.

The heavy black curve in Figure 3-4 represents how median Decadal Infiltration would change if Yucca Mountain was at different elevations, using the average relationship between MAP and elevation. Moving up in elevation results in both cooler and wetter climates; thus, changing elevation provides an analog to climatic changes over glacial cycles.

3.4 Decadal Infiltration Estimates Compared to Observation

Stothoff and Musgrove (2006) reviewed the available literature on worldwide recharge estimates, with an emphasis on studies applicable to Yucca Mountain. Several studies collected by Stothoff and Musgrove (2006) on spatial scales comparable to or smaller than the Footprint Box are compared with the Decadal Infiltration estimates in this section.

Estimates of hydrobasin-wide recharge are not compared to the Decadal Infiltration estimates. Hydrobasin-wide studies are much larger in spatial scale than the Footprint Box; thus, such studies combine the recharge from a much wider elevation range than representative of the Footprint Box. Hydrobasin studies also include alluvium-filled valleys that occupy more than half of the basin, whereas only a small fraction of the Footprint Box area has surficial deposits deeper than a meter. However, most Nevada hydrobasin studies listed by Lopes and Evetts (2004) are based on the Maxey-Eakin method for estimating recharge, which may be applied at scales similar to the Footprint Box. The Decadal Infiltration estimates are compared to the Maxey-Eakin method (Maxey and Eakin, 1949) and related models derived by Stothoff and Musgrove (2006).

3.4.1 Nevada Estimates

Several recharge estimates are available for locations in Nevada near Yucca Mountain. Lichty and McKinley (1995) report recharge estimates for small high-elevation basins in central Nevada north of the Nevada Test Site, and Russell, et al. (1987) report recharge estimates for Rainier Mesa, an upland area on the Nevada Test Site, Gee, et al. (1994) and Nichols (1987) estimate MAI from alluvial flats near Beatty, Nevada, and Winograd (1981) provides an upper-bound estimate on areal-average recharge in Yucca Flat on the Nevada Test Site.

Stothoff and Musgrove (2006) reinterpreted the Nichols (2000) analysis of 16 east-central Nevada hydrobasins to derive several relationships between precipitation and recharge. Most or all of these hydrobasins were reportedly used to derive the relationship developed by Maxey and Eakin (1949), which has become a standard approach for estimating hydrobasin-scale recharge in Nevada. Stothoff and Musgrove (2006) also identified several independent southern Nevada studies outside of the Yucca Mountain/Nevada Test Site area for which recharge was quantified at a scale smaller than an entire hydrobasin.

The Maxey-Eakin method is straightforward. Precipitation varies across a hydrobasin, generally increasing as a function of elevation. Temperature decreases approximately linearly with increasing elevation, which reduces evapotranspiration rates. The Maxey-Eakin method breaks the precipitation range into discrete bins (i.e., <8, 8 to 12, 12 to 15, 15 to 21, and >21 in/yr) and applies a constant recharge fraction within each bin (0, 3, 7, 15, and 25 percent, respectively) to account for the combined effects of increasing precipitation and decreasing evapotranspiration with increasing elevation.

Stothoff and Musgrove (2006) found that the observations from the Nichols (2000) study could be interpreted as a loglinear increase in recharge fraction with precipitation in the form

$$\log f = \min[A + B \log P,\ \log f_{max}] \qquad 3\text{-}1$$

where f is recharge fraction, f_{max} is maximum recharge fraction, P is mean annual precipitation, and A and B are fitting constants. Stothoff and Musgrove (2006) derived a total-system relationship between precipitation and recharge fraction by assuming that alluvial-fill basins and upland areas have similar hydrologic behavior with respect to recharge. Stothoff and Musgrove (2006) derived values of $A = -4.449$ and $B = 2.886$ when P is defined in inches per year and when $f_{max} = 0.626$, as assumed by Nichols (2000). Linearizing the Maxey-Eakin relationship by fitting a loglinear relationship between Maxey-Eakin bin midpoints yields $A = -4.399$ and $B = 2.876$. The total-system and linearized Maxey-Eakin relationships are essentially identical even though precipitation levels were significantly wetter during the Nichols (2000) study.

Stothoff and Musgrove (2006) derived additional loglinear relationships assuming that recharge in upland areas and in alluvial basins may not be similar. Assuming that alluvial basins have nonzero recharge and again assuming $f_{max} = 0.626$ and P is in inches per year, the relationship for upland recharge is $A = -3.190$ and $B = 1.798$. This relationship is directly comparable to the Footprint Box estimates, because it is not influenced by recharge in alluvial basins. However, the topography within the Footprint Box has an uncharacteristically large fraction of total area at the highest elevations with gentle slopes and shallow surficial cover. These features are associated with high values of MAI. Accordingly, it is reasonable to expect that average MAI across the Footprint Box may be somewhat larger than the relationship derived for the range of upland areas across hydrobasins.

The Maxey and Eakin (1949), Nichols (2000), and selected loglinear models are shown in Figure 3-5, as well as the independent recharge studies from southern Nevada. Most of the models are generally similar between 200 and 600 mm/yr [8 and 24 in/yr]. The Nichols (2000) model shares the characteristic of little or no recharge at low precipitation levels with the Maxey and Eakin (1949) model, but otherwise is much less sensitive to precipitation than the remaining models. The independent recharge models for upland areas are generally consistent with all of the loglinear models derived by Stothoff and Musgrove (2006), and the independent recharge models for alluvial basins are consistent with the total-system model.

The comparison between Figure 3-4 and Figure 3-5 suggests that the recharge relationships should vary somewhat across Nevada. There is a drop in MAT of approximately 6 °C [11 °F] from south to north in Nevada at any given elevation. At a given elevation with the same MAP, this temperature difference would yield approximately 50 percent higher MAI in northern Nevada than in the southern part of the state. Recharge is similarly larger for a given MAP in the rain shadow of the Sierra Nevada at a given latitude, because the given MAP value is found at higher elevations (with colder MAT) than in the wetter eastern portions of the state.

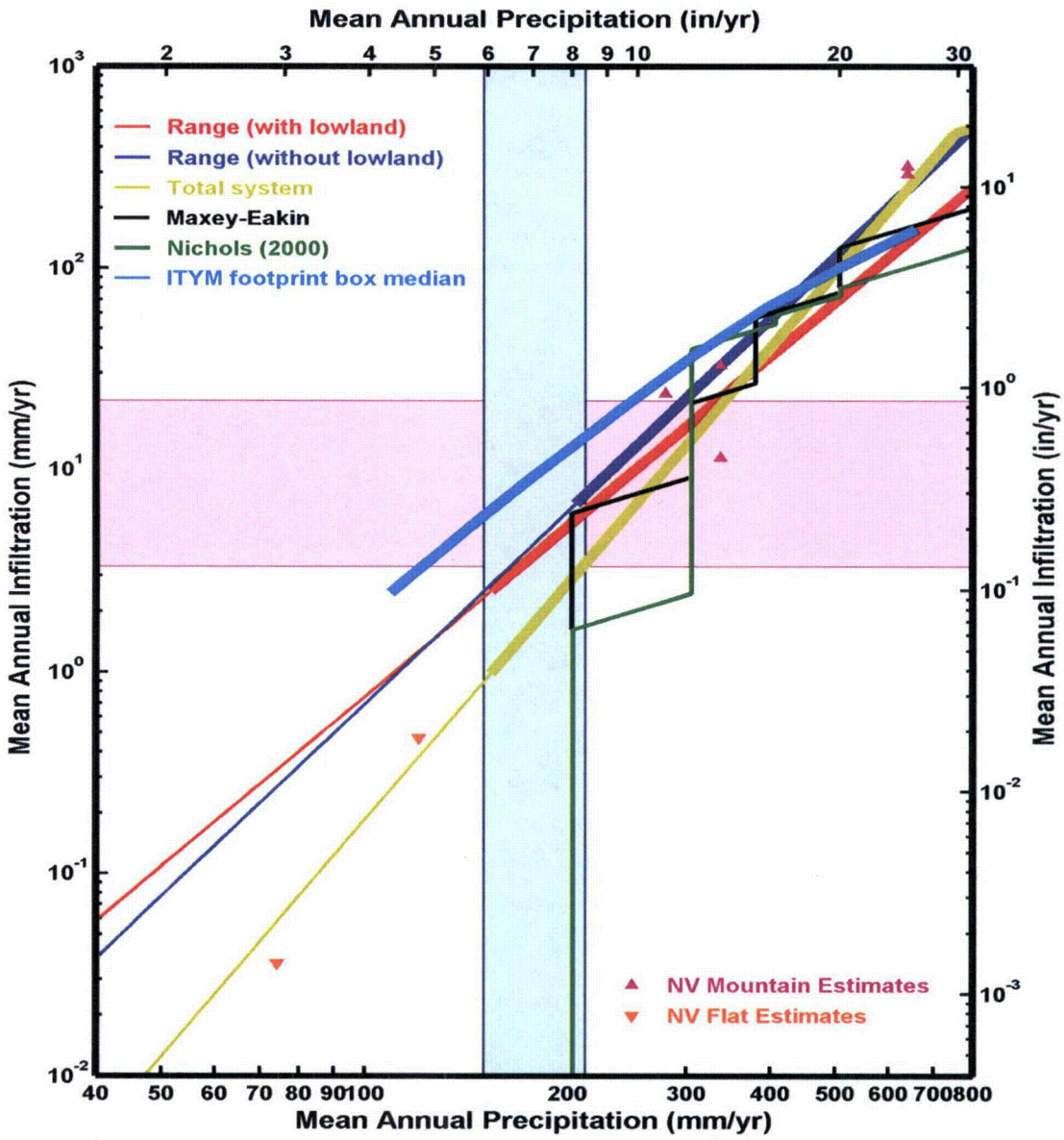

Figure 3-5. Relationships Between MAP and MAI for Hydrobasin Estimates

3.4.2 Estimates Based on Temperature Profiles

There is a regional upward flux of heat in the subsurface, which is expressed by a temperature gradient affected by the thermal properties of the underground formations without downward water flux. The natural geothermal gradient is purely due to heat diffusion. Several researchers have estimated downward flux of water at Yucca Mountain based on the deflection of the subsurface temperature profile from the diffusion-only profile. The temperature method has the advantages of (i) not relying on precipitation estimates and (ii) being insensitive to how water movement is partitioned between matrix and fracture flow. The method is sensitive to evaporation and lateral water flux as well as vertical water flux; thus it may be poorly suited for shallow boreholes and for boreholes in the vicinity of a fault.

Sass, et al. (1988) considered the temperature profile in 18 boreholes and estimates of the geothermal heat flux to derive estimates of vertical percolation fluxes. Bodvarsson, et al. (2003) use a one-dimensional analytic solution to estimate vertical percolation fluxes based on temperature profiles without the need to estimate the geothermal heat flux. Bodvarsson, et al. (2003) provide estimates for 16 of the Sass, et al. (1988) boreholes and 2 additional boreholes not considered by Sass, et al. (1988). Bodvarsson, et al. (2003) consider but discard an additional 14 boreholes with the rationale that the requirements for the analytic solution are not met. The selected boreholes are generally deep enough to include several geologic formations. Constantz, et al. (2003) consider two of the boreholes with an additional analysis. These estimates are listed in Table 3-2. Estimates indistinguishable from zero were obtained for several boreholes.

Note that Bodvarsson, et al. (2003) calculate analytic solutions for 28 boreholes, discard 10 solutions, and correct 2 solutions without providing a basis for the correction. The Bodvarsson, et al. (2003) values in Table 3-2 represent the uncorrected solutions for the 18 retained boreholes.

Bodvarsson, et al. (2003) display root-mean-square-error curves for most of the boreholes. While the curves generally have a unique minimum, a range of water flux estimates yield nearly the same root-mean-square error. Visually estimating the fluxes resulting from a 10 percent increase in error suggests that the estimates are within 2 to 10 mm/yr [0.08 to 0.39 in/yr],generally increasing with flux, and most estimates are within 4 to 6 mm/yr [0.16 to 0.24 in/yr]. These visually estimated values are listed in Table 3-2 as the low and high estimates for Bodvarsson, et al. (2003). Table 3-2 shows the Sass, et al. (1988) and Bodvarsson, et al. (2003) estimates are within 4 mm/yr [0.16 in/yr] for 10 of the 16 shared boreholes. The Constantz, et al. (2003) estimates are within 8 mm/yr [0.31 in/yr] of the Bodvarsson, et al. (2003) and Sass, et al. (1988) estimates in both cases, but have a significantly wider uncertainty range.

The collection of flux estimates in Table 3-2 are shown in Figure 3-6. Most of the estimates are within or close to the one-standard deviation MAI band from ITYM, although seven fall well below the band. None of the estimates are from the highest quarter of the MAP band, illustrating that the high-elevation zones of Yucca Mountain are less well represented than the lower elevations. In general, estimates of deep percolation fluxes from borehole temperature profiles appear consistent with the Footprint Box estimates for MAI.

Table 3-2. Vertical Deep Percolation Fluxes Inferred From Borehole Temperature Profiles. Estimated Mean Annual Precipitation at the Ground Surface is Presented for Reference.*

	MAP†	Bodvarsson, et al.‡			Sass§	Constantz, et al.‖		
Borehole	mm/yr	Low	Best	High		Low	Best	High
UE-25 A#7	156	2	7	12	7			
USW G-1	167	21	27	35	5			
USW G-2	193		~0		11			
USW G-3	184		~0		4			
USW G-4	161	4	8	12	5			
USW H-1	164				9			
USW H-3	185	~0	5	10	3	3.3	10.5	18.7
USW H-4	159	9	13	17	~0			
USW H-5	184	22	25	29	5			
USW H-6	164	~0	8	18	4			
SD-12	167	13	15	17	15			
USW UZ-1	169		8		8			
USW WT-1	154				7			
USW WT-2	164	0.5	4	7	0.5	-7.8	0.14	7.8
UE-25 WT #4	151	6	10	15	7			
UE-25 WT #6	166		~0					
USW WT-7	154	0.5	3	5	3			
UE-25 WT #16	155		3					
UE-25 WT #17	147		~0		~0			
UE-25 WT #18	168		12		12			

*All flux values are in mm/yr [100 mm/yr = 3.94 in/yr]
†Mean Annual Precipitation (MAP)
‡Bodvarsson, G.S., E. Kwicklis, C. Shan, and Y.-S. Wu. "Estimation of Percolation Flux From Borehole Temperature Data at Yucca Mountain, Nevada." *Journal of Contaminant Hydrology.* Vols. 62–63. pp. 3–22. 2003.
§Sass, J.H., A.H. Lachenbruch, W.W. Dudley, Jr., S.S. Priest, and R.J. Munroe. "Temperature, Thermal Conductivity, and Heat Flow Near Yucca Mountain, Nevada: Some Tectonic and Hydrologic Implications." U.S. Geological Survey Open-File Report No. 87-649. Denver, Colorado: U.S. Geological Survey. 1988.
‖Constantz, J., S.W. Tyler, and E. Kwicklis. "Temperature-Profile Methods for Estimating Percolation Rates in Arid Environments." *Vadose Zone Journal.* Vol. 2. pp. 12–24. 2003.

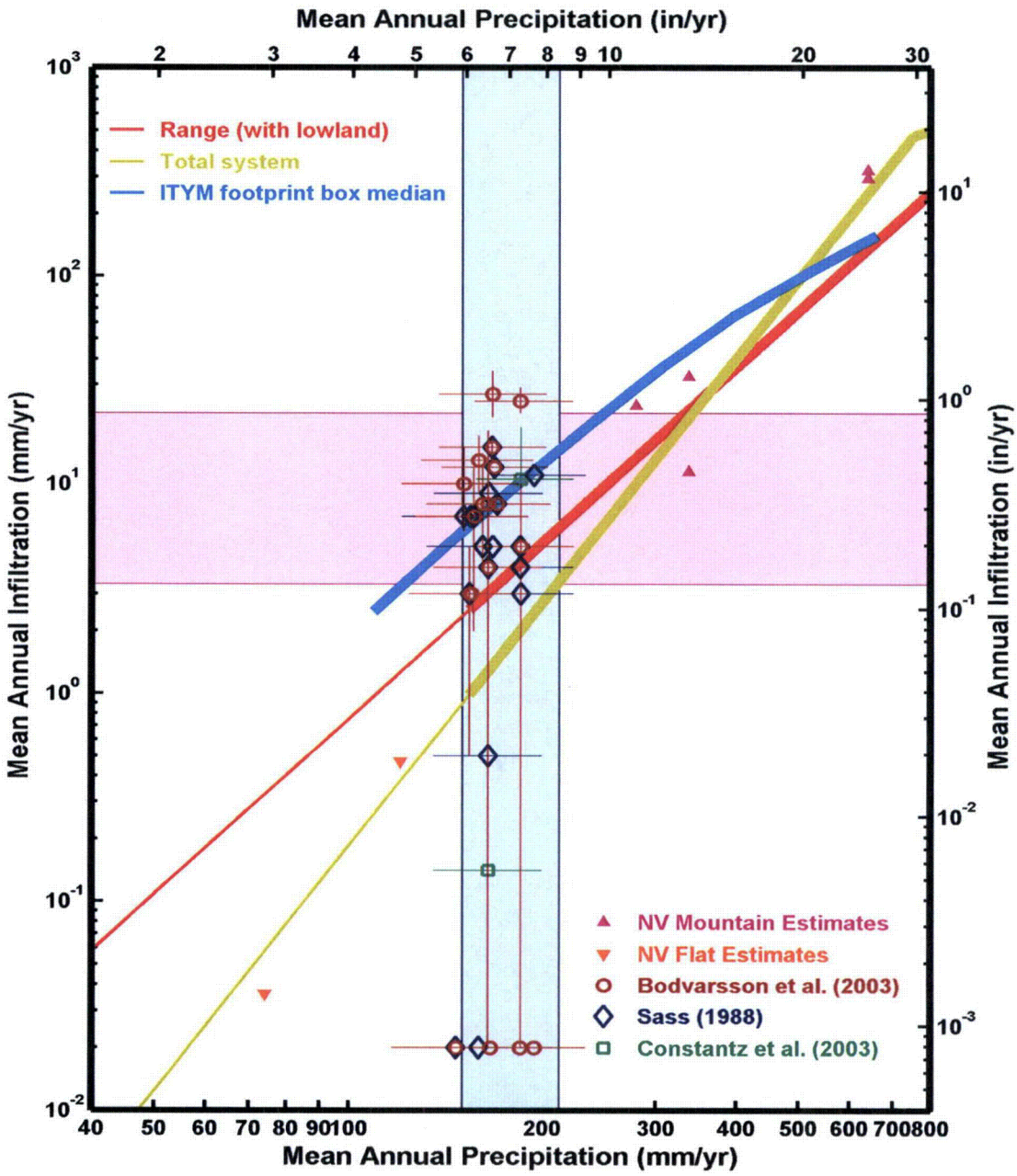

Figure 3-6. Mean Annual Infiltration Relationships From Borehole Temperature Profiles. Zero and Negative Values Are Plotted as 2×10^{-2} mm/yr. Hydrobasin Estimates Are Shown for Reference.

3.4.3 Estimates Based on Saturated Zone Chloride Mass Balance

Chloride salts are deposited at the ground surface through both dry deposition (e.g., windblown dust settles on the ground with chloride salts attached to the dust particles) and wet deposition (i.e., rainfall and snowfall that contain dissolved chloride ions). Because chloride ions are conservative, evaporation increases the chloride concentration in the solution. With a known chloride deposition rate, the chloride concentration in pore waters indicates the fraction of precipitation that escapes evapotranspiration in the soil column. The method is classically applied under the restrictive conditions of steady state, negligible mixing, and negligible contribution to pore-water chloride from the host matrix. The method may be most appropriate for deep unfractured profiles, such as the alluvial flats in Nevada basins. The chloride mass balance method can be extended to consider a mixing model with more than one input stream (e.g., matrix and fracture pathways, Holocene and Pleistocene recharge). The Holocene period started approximately 11,500 years before present and has continued through the present. The Pleistocene started about 1.8 million years before present and extended to the Holocene; when recharge is considered Pleistocene in age, this often refers to the last glacial period, which ended as the Holocene began.

The chloride mass balance method relates observed porewater chloride concentrations to the effective chloride concentration in precipitation, using the relationship (e.g., CRWMS M&O, 2000; Zhu, et al., 2003)

$$C_g = \left(\frac{P}{R}\right) C_p = \frac{C_p}{F} \tag{3-2}$$

where C_g is the groundwater concentration, C_p is the long-term-average effective concentration in precipitation accounting for both wet and dry deposition, P is long-term-average mean annual precipitation, R is long-term-average mean annual recharge, and F is the recharge fraction ($F = R / P$). Estimates for F depend only on observed values for C_g and estimated values for C_p. Estimates for R also depend on estimates of P.

CRWMS M&O (2000) and Zhu, et al. (2003) use the chloride mass balance method to estimate MAI based on observations in the saturated zone under Yucca Mountain. Both CRWMS M&O (2000) and Zhu, et al. (2003) interpret the sampled waters as Pleistocene in origin based on stable isotope chemistry observations in Crater Flat and under Yucca Mountain, indicating that the waters were recharged under cooler climatic conditions than currently occur at Yucca Mountain. However, CRWMS M&O (2000) used Holocene estimates for P and C_p to estimate recharge, assuming a value of 170 mm/yr [6.7 in/yr] for P and using low, medium, and high estimates of 0.3, 0.35, and 0.6 for C_p. The two studies calculated similar recharge rates, but the assumption of a Holocene origin implies a recharge fraction of nearly 6 percent, whereas the assumption of a Pleistocene origin implies a recharge fraction of slightly more than 3 percent.

Table 3-3 and Figure 3-7 present estimates of recharge rates using the CRWMS M&O (2000) estimates for C_p and lower, middle-, and upper-bound estimates of P based on the ground surface elevation at the borehole location and the Orbital-Cycle Climate for Yucca Mountain (OCCYM) description for MAP from Section 2.3.3. The low, medium, and high MAI estimates in Table 3-3 are calculated with matching low, medium, and high values for both P and C_p; for

Table 3-3. Estimates of Recharge to the Saturated Zone Using the Chloride Mass Balance Method. Estimated MAP* at the Ground Surface is Presented for Reference						
	Estimated MAP* [mm/yr]†			Estimated MAI‡ [mm/yr]†		
Borehole	Low	Medium	High	Low	Medium	High
UE-25 B#1	130	163	204	3.6	5.3	11.3
UE-25 C#1	125	156	195	5.1	7.4	15.8
UE-25 C#2	123	154	192	5.2	7.6	16.2
UE-25 C#3	125	156	195	5.2	7.6	16.2
UE-25 C#3 (1995)	125	156	195	5.8	8.4	18.0
USW G-2	164	205	256	7.6	11.0	23.6
USW G-4	136	171	213	6.9	10.1	21.7
USW H-1	139	174	218	7.3	10.7	22.9
USW H-3	157	196	245	4.9	7.2	15.5
USW H-4	135	168	210	5.9	8.5	18.3
USW H-5	156	195	244	7.7	11.2	24.0
UE-25 ONC#1	127	159	199	5.4	7.8	16.8
UE-25 P#1	123	154	193	2.8	4.2	8.9
USW UZ-14	144	180	224	6.4	9.4	20.1
USW UZ-16	132	165	206	3.7	5.5	11.7
UE-25 WT #3	117	146	183	5.8	8.5	18.3
UE-25 WT #12	120	150	188	4.6	6.7	14.5
UE-25 WT #17	124	155	194	5.8	8.5	18.2
*Mean Annual Precipitation (MAP) †100 mm/yr = 3.94 in/yr ‡Mean Annual Infiltration (MAI)						

example, the medium MAI estimate uses the middle value for P and the medium estimate for C_p. The recharge estimates in Table 3-3 are labeled "YM SZ Cl Mass Balance" in Figure 3-7.

There is reason to suspect that the estimated recharge rates in Table 3-3 are not representative of either Holocene or Pleistocene recharge at Yucca Mountain. Saturated zone waters may be generally younger than Pleistocene age, as suggested by Cl-36 and C-14 indicators of groundwater age. Zhu, et al. (2003) use a mixing model chloride mass balance model to estimate recharge in perched waters under Yucca Mountain, as discussed in Section 3.4.5.

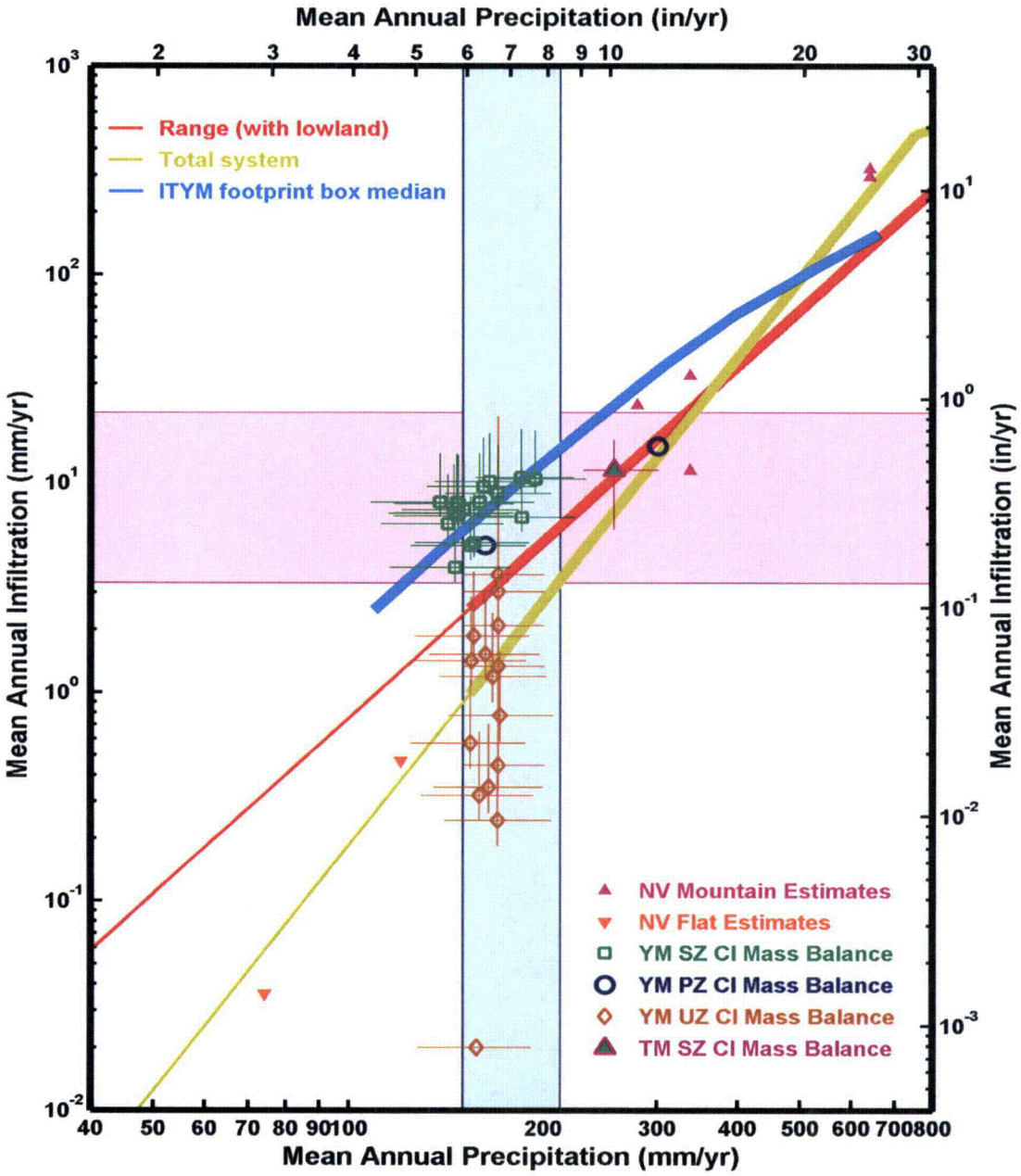

Figure 3-7. Mean Annual Infiltration Relationships From Chloride Mass Balance Methods. Very Small Values Are Plotted as 2×10^{-2} mm/yr. Hydrobasin Estimates Are Shown for Reference.

Zhu, et al. (2003) estimate significantly different values for the ratio of Cl-36 to chloride ion concentrations to represent Holocene and Pleistocene recharge and use these values to infer the fraction of Holocene and Pleistocene waters in perched water samples. The three samples of saturated zone pore waters with measured ratios of Cl-36 to chloride ion concentrations reported by Zhu, et al. (2003) all have values that are closer to the Holocene endpoint than any perched water sample considered by Zhu, et al. (2003), suggesting that the saturated zone water is dominated by Holocene recharge.

Geochemical indicators are consistent with the hypothesis that a large portion of saturated zone waters recharged upstream at higher elevation. Groundwater models and flow-path analyses presented by CRWMS M&O (2000) suggest that the waters under Yucca Mountain passed under Timber Mountain caldera north of Yucca Mountain. Timber Mountain is 1,800 to more than 2,100 m [6,000 to more than 7,000 ft] above sea level, whereas Yucca Mountain is approximately 1,200 to 1,500 m [4,000 to 5,000 ft] above sea level. The approximate difference of 600 m [2,000 ft] in elevation implies that MAT is almost 4 °C [7 °F] cooler at Timber Mountain caldera based on the regional temperature lapse rate. Fractionation of stable isotopes is affected by temperature. The largest difference in stable isotope signature across Yucca Mountain and Crater Flat implies a temperature difference of approximately 4°C, with the warmest signature in active recharge locations at an elevation of approximately 1,200 m [4,000 ft] in upper Forty Mile Wash and the coolest signature in Crater Flat directly down-gradient from Timber Mountain caldera. Accordingly, the stable isotope observations alone do not distinguish between Timber Mountain recharge at high elevations and Pleistocene recharge at Yucca Mountain elevations. Further, assuming that a range of MAP from 230 to 300 mm/yr [9.1 to 11.8 in/yr] is representative of Timber Mountain caldera and using the same approach to estimate chloride deposition rates followed by CRWMS M&O (2000) and Zhu, et al. (2003), groundwater chloride concentrations typical of Yucca Mountain in the range of 6 to 8 mg/L [6 to 8 ppm] provide recharge fractions of 3.8 to 5.7 percent.

The recharge estimate labeled "TM SZ Cl Mass Balance" in Figure 3-7 represents the average recharge for the set of saturated zone chloride concentrations in boreholes reported by CRWMS M&O (2000). The recharge estimate uses the formula for nominal chloride deposition rate reported by Zhu, et al. (2003) with MAP of 256 mm/yr [10.1 in/yr] to represent an average elevation of 1,900 m [6,200 ft]. The error bars for the estimate represent the range of MAP from 230 to 300 mm/yr [9.1 to 11.8 in/yr] and the recharge estimates over this MAP range for the boreholes with the lowest and highest observed saturated zone chloride concentrations. The average of the individual borehole recharge estimates ranges from 11 to 13 mm/yr [0.43 to 0.51 in/yr] over this MAP range using the nominal chloride deposition rate (i.e., not accounting for uncertainty in chloride deposition rate). Note that the recharge estimate inferred for Timber Mountain caldera is consistent with the upland recharge relationships discussed in Section 3.4.1.

Travel times from Timber Mountain caldera to Yucca Mountain in the volcanic aquifer are uncertain, but it is reasonable to expect that travel times for the approximately 20-km [12-mi] distance may be significantly less than 10,000 years. CRWMS M&O (2000) cites several studies considering groundwater velocities in fractured tuff aquifers in the vicinity of Yucca Mountain, with estimates ranging from 1.9 to 46 m/yr [6.2 to 150 ft/yr]. Based on these geochemical lines of evidence, it may be reasonable to assume that a large component of the saturated zone waters derives from Holocene recharge in Timber Mountain caldera. If this is

the case, models that do not account for mixing within the saturated zone may not provide reliable estimates of recharge under Yucca Mountain.

3.4.4 Estimates Based on Perched Water

Two perched water bodies have been identified below the horizon of the potential repository in boreholes UZ-1, UZ-14, NRG-7a, SD-7, SD-9, and WT-24. The southern body has a relatively small extent and was drained in 30 hours at a pumping rate of 0.75 m^3/hr [3.0 gpm] from SD-7 (Bagtzoglou, 2003). The northern body, intercepted by the other boreholes, appears to be orders of magnitude greater in extent and volume.

Bagtzoglou (2003) considered the southern perched water at an east-west cross section of Yucca Mountain passing through the intersection of the Ghost Dance and Sundance faults. Bagtzoglou (2003) compared three different subsurface hydraulic models, finding that the volume of perched water is matched with average infiltration rates of 0.13, 0.51, and 6.2 mm/yr [0.005, 0.02, and 0.24 in/yr], respectively, but C-14 constraints are best matched with the highest infiltration flux. Note that best-fit recharge estimates are strongly dependent on uncertain hydraulic properties; thus these estimates are also uncertain.

Zhu, et al. (2003) developed a modified chloride mass balance approach incorporating Cl-36 observations. Zhu, et al. (2003) used observations from boreholes UZ-14 and WT-24, which intersect the more extensive northern perched water body below the potential repository horizon, to estimate both Holocene and Pleistocene recharge rates. The WT-24 borehole is located on an elevated ridge that has low estimated infiltration rates near the borehole and for more than a kilometer updip, while the UZ-14 borehole is located in a wash with deep alluvium and relatively low estimated infiltration rates updip. Zhu, et al. (2003) inferred a Holocene recharge rate of 5 ± 1.4 mm/yr [0.2 ± 0.055 in/yr] and a Pleistocene recharge rate of 15 ± 5.2 mm/yr [0.59 ± 0.2 in/yr] using best estimates for chloride deposition rate and an intermediate value for precipitation from a range representative of glacial transition climates. The Zhu, et al. (2003) perched water estimates are shown in Figure 3-7, labeled "YM PZ Cl Mass Balance."

3.4.5 Estimates Based on Unsaturated Zone Chloride Mass Balance

The chloride mass balance method is often applied in thick sequences of unsaturated, unconsolidated sediments in arid zones, where flow is vertical and fast pathways may be neglected in accordance with the underlying assumptions behind the method. CRWMS M&O (2003a) estimate percolation flux in Yucca Mountain using chloride observations from unsaturated zone pore waters obtained from boreholes, the Exploratory Studies Facility, and Cross-Drift Tunnel core samples. The samples are obtained from both welded and nonwelded units. The unsaturated zone flux estimates are shown in Figure 3-7, labeled "YM UZ Cl Mass Balance", and tend to be much smaller than estimates derived from the temperature profiles described in Section 3.4.3. Borehole SD-12 is the only location where estimates from both borehole temperature profiles {15 mm/yr [0.59 in/yr]} and unsaturated-zone chloride mass balance {1.2 mm/yr [0.047 in/yr]} can be compared directly, and the chloride mass balance flux estimate is more than an order of magnitude smaller.

There is reason to believe that not all the assumptions in the chloride mass balance method are met for the fractured unsaturated tuff at Yucca Mountain. Typically, the chloride mass balance

method assumes that piston flow occurs, so that all water at a given depth is the same age, and this assumption is tacitly made in the CRWMS M&O (2003a) analysis. This assumption is not strictly necessary under steady conditions, as long as all pathways have the same chloride concentration (i.e., all pathways are in chemical equilibrium). There is some evidence of fast flow pathways at Yucca Mountain [e.g., evidence of bomb-pulse chemistry throughout the Tiva Canyon and deep into the Paintbrush tuffs and even at locations in the Topopah Springs tuff forming the proposed repository horizon (CRWMS M&O, 2003a)]. Bomb-pulse Cl-36 observations at depth are explained as the result of flow within fractures, as the samples with bomb-pulse observations were obtained from features associated with fractures. However, all of the unsaturated zone chloride samples presented by CRWMS M&O (2003a) are from matrix pore waters, and none are from the fracture system that forms the fast pathways.

Vertically moving waters drain into the perched water system, where waters from different pathways mix. The chloride concentration in perched water samples ranges from 4.1 to 9 mg/L [4.1 to 9 ppm]. The chloride concentration in unsaturated tuff pore waters from tunnel, drift, and alcove samples reported by CRWMS M&O (2003a) averages 39 mg/L [39 ppm]. Only 2 of 78 unsaturated tuff samples have concentrations less than 11 mg/L [11 ppm], and 51 samples have concentrations of at least 20 mg/L [20 ppm]. This disparity in chloride concentration in the unsaturated tuff pore water and perched water may be due in part to chloride dilution in the perched zone from Pleistocene waters {Zhu, et al. (2003) estimates that the effective chloride concentration in precipitation during the Pleistocene and Holocene was 0.18 and 0.35 mg/L [0.18 and 0.35 ppm], respectively}, but the disparity between perched-water and typical pore-water concentrations is too large to explain through this mechanism. Accordingly, it appears that pathways with dilute chloride concentrations may not be fully considered in most of the unsaturated zone chloride mass balance estimates. Because incompletely accounting for pathways with dilute concentrations artificially lowers flux estimates, actual unsaturated zone fluxes may be several times larger than the estimates calculated by CRWMS M&O (2003a).

3.5 Millennial Infiltration Estimates

The Decadal Infiltration estimates are representative of MAI at time scales that are short relative to orbital cycles with periodicities of 19,000 to 100,000 years. Decadal Infiltration is nonlinearly sensitive to climate, with wetter-than-average conditions generating a disproportionate increase in net infiltration. Because of this nonlinear sensitivity, net infiltration will be larger when climate is variable than when climate remains constant, because wetter-than-average periods will provide a disproportionate increase in net infiltration. There is a concern that the strategy of characterizing climate on orbital-scale time scales will underestimate recharge using decadal-average estimates unless the intermediate time scales are considered.

Existing proxy information can help quantify the effect of intermediate-scale climatic variability. A tree-ring record from bristlecone pines in Methuselah Walk, above 3,200 m [10,500 ft] in the White Mountains east of the Sierra Nevada crest in Inyo County, California, extends almost 8,000 years into the past. This tree-ring record has been linked to annual (July–June) precipitation in central Nevada based on average ring widths (Hughes and Graumlich, 1996). Nutrients acquired during the year fuel the summer growth of rings; thus bristlecone ring widths are sensitive to annual precipitation and are also thought to be affected by temperature.

The tree-ring dataset (Hughes and Graumlich, 2000) contains samples that were taken from trees experiencing a range of growth-affecting microclimatic conditions, so individual trees do

not perfectly track the average conditions. The sequence of average ring widths with different moving averages is shown in Figure 3-8. There is a clear millennial-scale sequence of average ring widths. A long-term trend toward thinner rings is superimposed on the millennial-scale trend.

Historical precipitation observations were obtained from the National Climatic Data Center for nearby National Weather Service cooperative stations at Dyer, Nevada, and California stations at White Mountain 1 and 2, Deep Springs, and Bishop. These stations all overlap the tree-ring record for the period between 1957 and 1978. The R^2 value between the logarithm of annual ring width and the logarithm of annual precipitation using July through June as a growth year as suggested by LaMarche (1976) for individual stations is between 0.21 and 0.32, increasing to 0.42 when compared against the geometric mean of the five stations. The R^2 value between the logarithm of annual precipitation for the stations is between 0.32 and 0.67, suggesting that the tree-ring record captures some of the precipitation patterns, but not all. The sequence of tree-ring widths during historical periods suggests that precipitation may limit growth in dry years (disproportionately so in the second consecutive dry year), but other unknown factors may limit growth in wet years.

Insufficient information exists to completely disentangle the effects of precipitation and temperature on ring widths. It is likely that the long-term trend toward smaller rings is due in

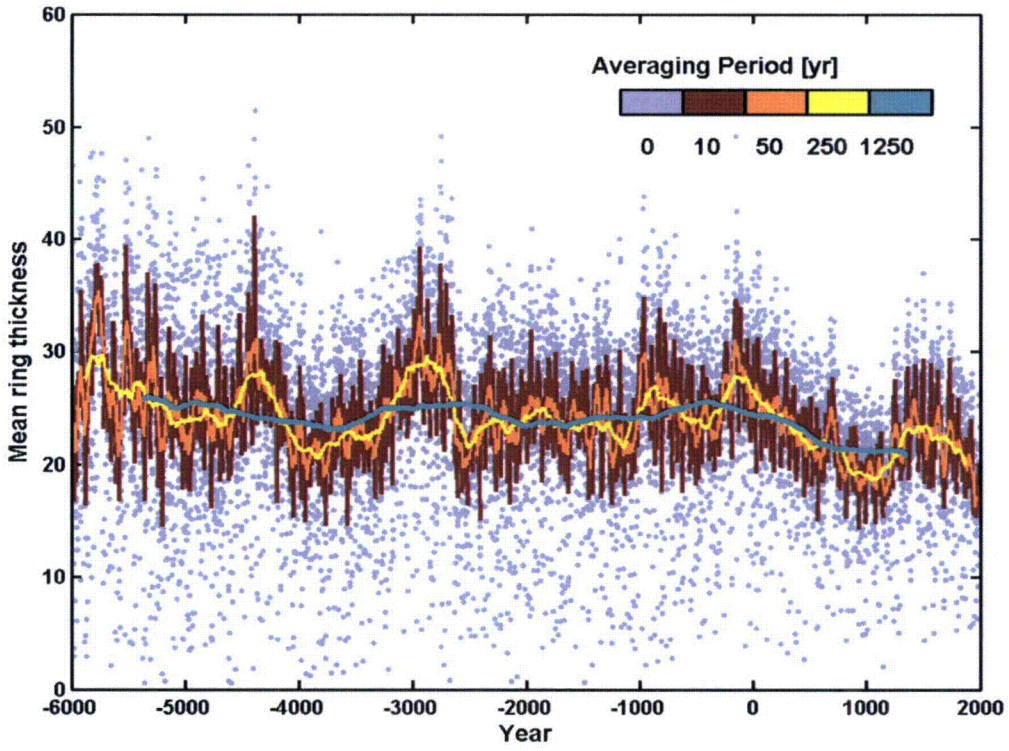

Figure 3-8. Mean Tree-Ring Thickness From Methuselah Walk Observations. Dots Represent Annual Observations, and Lines Represent Moving Averages.

part to somewhat cooler conditions in the last few thousand years. A cooling trend of a few degrees Celsius has been inferred from tree-line dynamics (Lloyd and Graumlich, 1997). The growing season for bristlecone pines is a few months out of the year, and the growing season may be significantly lengthened and enhanced by warming just a few degrees. A change in temperature of 3 °C [5.4 °F], holding precipitation fixed, only changes Decadal Infiltration by a few percent, as can be seen in Figure 3-4. The same change could easily explain systematically thicker rings during the first part of the record. To assess the effects of climatic variability on net infiltration, it is assumed that tree-ring widths monotonically correspond to annual precipitation (i.e., effects due to changing precipitation from seasonality are neglected), and the relationship between ring width and precipitation is the same for the entire sequence (i.e., age-dependent effects are neglected). Assuming that all variability is due to annual precipitation creates the widest range of inferred precipitation values. Comparison between the local stations and the ring record suggests that a power law equation reasonably describes the relationship between MAP and ring width; thus the monotonic relationship is assumed to have the form

$$P_i = A w_i^a \tag{3-3}$$

where P_i is annual precipitation for year i, w_i is mean annual ring width for year i, and a and A are fitting constants. The relationship is location dependent. Smoothing the annual precipitation sequence with a 10-year moving average provides surrogate decadal precipitation sequences. The decadal tree-ring sequences should better represent decadal precipitation than annual tree-ring sequences represent annual precipitation.

The relationship is calibrated with the historical record from the Global Historical Climate Network, which provides a worldwide database of precipitation observations. Figure 3-9 displays a regressed relationship between the coefficient of variation of annual precipitation and the magnitude of annual precipitation based on stations around the world with record lengths between 50 and 70 years. The relationship has the form

$$\log(\sigma / \mu) = a_1 Y + b_1 \tag{3-4}$$

where μ and σ are the mean and standard deviation of P, Y is $\log \mu$, and $a_1 = -0.301$ and $b_1 = 0.301$ are constants. Stations from in and near Nevada are reasonably well described with this relationship, as shown in Figure 3-9.

The a and A parameters can be estimated by combining Eqs. (3-3) and (3-4). Averaging Eq. (3-4) over a suitable period

$$\mu = A\mu^* \tag{3-5}$$

$$\sigma = A\sigma^* \tag{3-6}$$

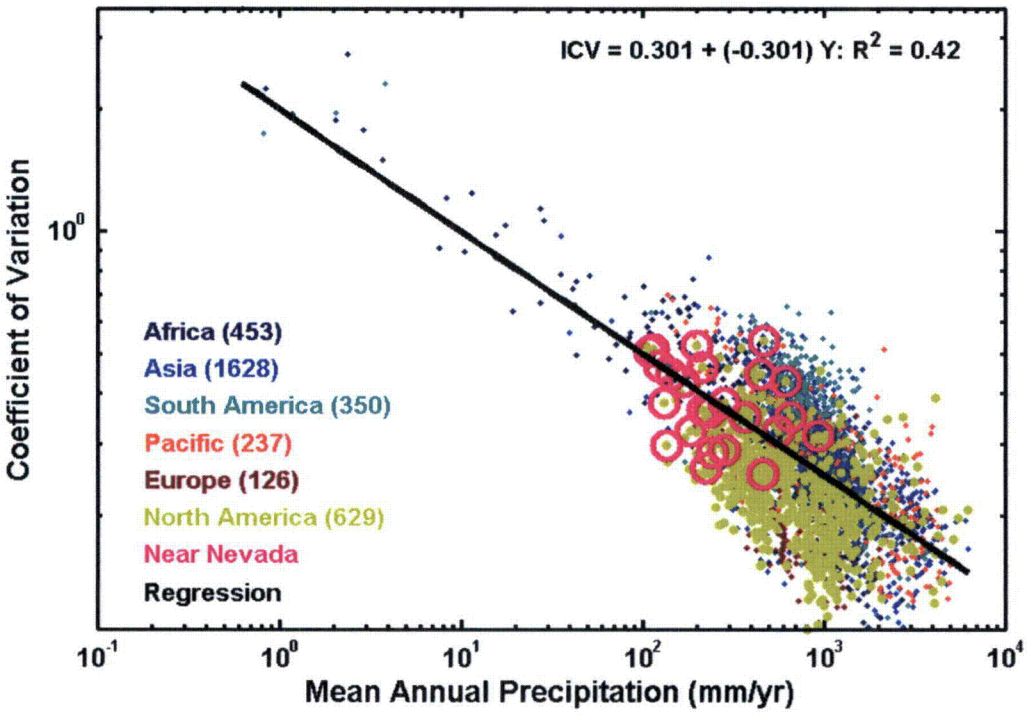

Figure 3-9. Global Relationships Between Mean Annual Precipitation and the Coefficient of Variation of Annual Precipitation. All Stations in the Global Historical Climate Network With Record Length Between 50 and 70 Years Are Shown. [100 mm/yr = 3.94 in/yr]

where μ^* and σ^* denote the mean and standard deviation of w^a, respectively. The a fitting constant in Eq. (3-3) can be found by minimizing

$$\varepsilon = \log(\sigma^* / \mu^*) - a_1 Y - b_1 \qquad (3\text{-}7)$$

and A is found by substituting μ^* (calculated with the optimal a parameter) into Eq. (3-5). Note that the parameters derived from the calibration period are used throughout the tree-ring record and may overestimate variability somewhat during wetter periods of the tree-ring record.

Assuming that μ = 150 mm/yr [5.9 in/yr] for a reference location during the 20-year calibration period of 1957 through 1976 when nearby meteorological stations overlap the tree-ring record, a = 1.11 and A = 1.7 for w in the tree-ring database units. The estimate of MAP for the entire tree-ring record using these parameters is shown in Figure 3-10(a), with an estimated average MAP of 261 mm/yr [10.3 in/yr]. Estimated MAP averaged over the entire 8,000-year tree-ring record drops from 1.74 to 1.4 times larger than MAP averaged over the 20-year calibration period as μ increases from 150 to 600 mm/yr [5.9 to 33 in/yr], because the coefficient of

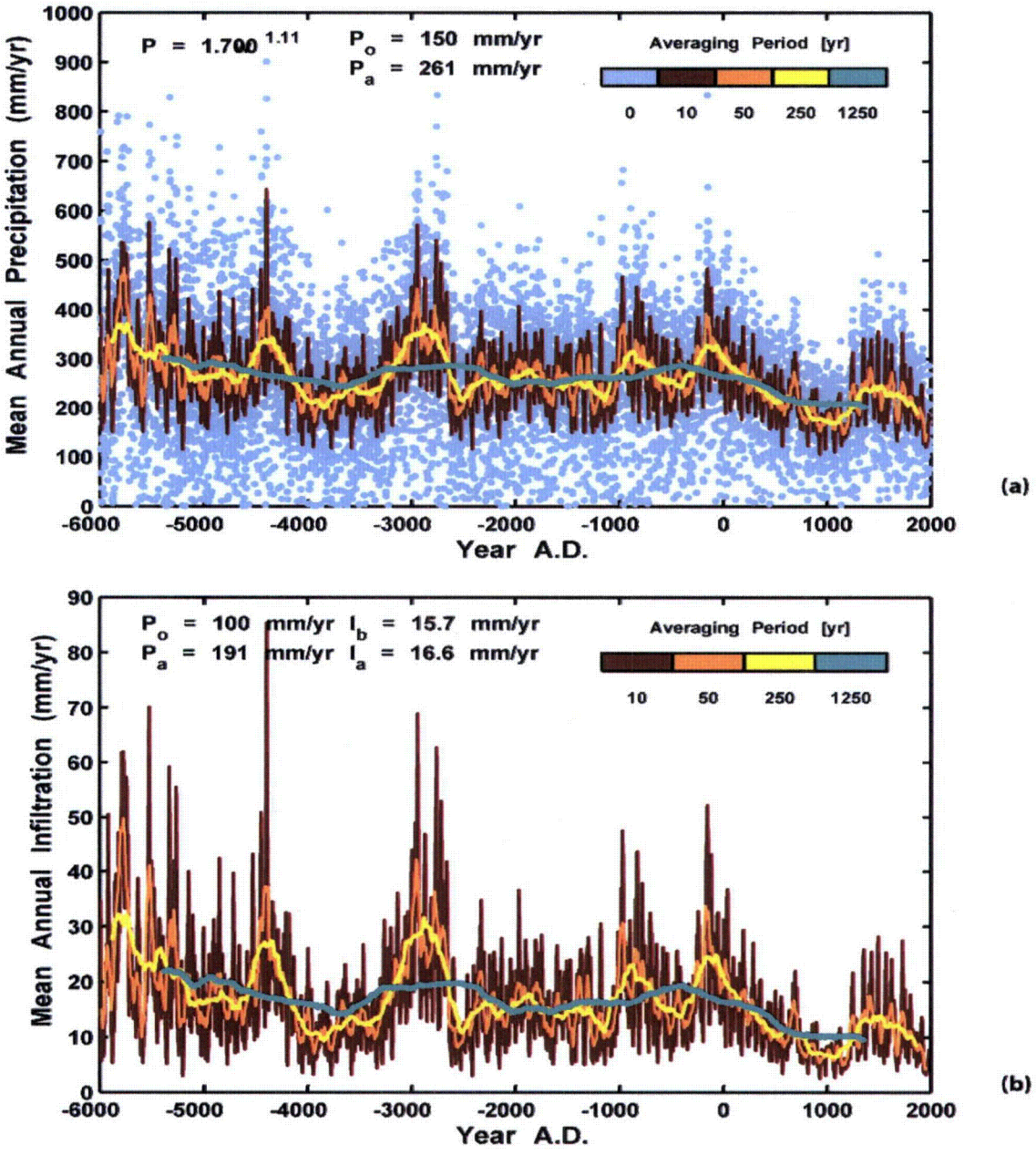

Figure 3-10. Estimates of (a) Mean Annual Precipitation and (b) Mean Annual Infiltration From Methuselah Walk Observations. P_o Is MAP During the Calibration Period, P_a Is Average MAP Over the Entire Record, I_b Is MAI Using P_a, and I_a Is Average MAI Over the Entire Record. Dots and Lines Represent Annual Estimates and Moving Averages, Respectively. [100 mm/yr = 3.94 in/yr]

variation is smaller for higher precipitation rates. These estimates are subject to the confounding effect on ring width because of concurrent changes in MAT that would tend to overestimate MAP, suggesting that the increase in MAP averaged over the 8,000-year period is probably overestimated with this calculation.

Record-average MAP increases from the calibration value in part because the tree-ring record suggests that the current climate is in the dry part of a millennial cycle. Several lines of evidence, such as high lake stands across Nevada, are consistent with the episodic wetter conditions during the Holocene implied by the tree-ring record. For example, Benson, et al. (2002) present records from Lake Tahoe, Pyramid Lake, and Owens Lake, suggesting oscillatory lake levels from circa 8,000 to 6,500 calendar years before present (cal YBP) followed by a dry period. Lake Tahoe had rising waters circa 5,500 cal YBP and overflowing conditions circa 5,000 cal YBP. Note that MAP estimates from the tree-ring record may under represent basin-scale hydrologic changes, because groundwater recharge increases approximately as the cube of MAP (see Figure 3-4).

Thompson, et al. (1999a) suggested that the Holocene as a whole may have been significantly drier than the last half of the 20th century. However, tree-ring and other proxy evidence implies the opposite may be true: that the historical record may be near the arid end of the range of climatic conditions seen during the Holocene.

Climate variability tends to increase net infiltration relative to net infiltration with the equivalent steady state climate, which may be called an amplification effect due to variability. The amplification effect due to decadal variability over several millennia, a duration sufficiently short that insolation characteristics are nearly unchanged, can be bounded by comparing two average net infiltration values calculated using (i) the sequence of estimated decadal precipitation values and (ii) the long-term-average precipitation over the entire record. The amplification effect determined from the 8,000-year tree-ring record is expected to overestimate the amplification effect during cooler and wetter conditions, because interannual precipitation variability decreases under wetter conditions and because infiltration is less sensitive to precipitation variability under wetter conditions (see Figure 3-4).

An example calculation suggests that the amplification effect is small. Selecting a MAP calibration value of 100 mm/yr [3.9 in/yr] provides an average MAP value of 191 mm/yr [7.5 in/yr], representative of present-day MAP estimates at the Footprint Box reference elevation. This warm and dry example should provide a more extreme amplification effect than almost any other conditions during a glacial cycle. The resulting infiltration sequences for present-day MAT are shown in Figure 3-10(b). Decadal-average MAI varies from 2.5 to 85 mm/yr [0.1 to 3.3 in/yr], 50-year-average MAI varies from 4.2 to 50 mm/yr [0.17 to 2 in/yr], and 250-year-average MAI varies from 6.4 to 32 mm/yr [0.25 to 1.3 in/yr]. The MAI value for the average MAP over the sequence is 15.7 mm/yr [0.618 in/yr], while the average decadal-average MAI value is 16.6 mm/yr [0.654 in/yr]—5.7 percent larger.

Even with the extreme range in decadal-average MAI seen in the example and under conditions for which the amplification effect would be largest, the amplification effect is small compared to the uncertainty in MAI estimates. A slightly larger amplification effect would be observed if MAT were negatively correlated to MAP (i.e., wet decades or wet periods in the millennial cycle are also cooler). However, a temperature change of a few degrees Celsius has little effect on MAI

(see Figure 3-4); thus temperature excursions that might reasonably have occurred during the Holocene would not be expected to significantly increase the amplification effect.

Climatic variability on time scales between 10 and 8,000 years (timesteps) systematically increases long-term-average MAI by as much as 6 percent based on this example. Accordingly, Millennial Infiltration estimates are obtained by simply increasing Decadal Infiltration estimates by 6 percent.

3.6 Seasonality and Net Infiltration

3.6.1 Regional Seasonality Patterns

Infiltration-affecting factors vary seasonally, so it is reasonable to expect the near-surface soil water balance to also vary seasonally. Evapotranspiration is much more effective at removing soil water during hot seasons, and precipitation patterns tend to be more intense and shorter in duration during the summer in the American Southwest. Winograd, et al. (1998) present evidence from long-term sampling from spring discharges high in the Spring Mountains, Nevada, which are located in the transitional region between winter- and summer-dominated precipitation patterns. The Winograd, et al. (1998) evidence suggests that winter precipitation is significantly more efficient at inducing recharge than summer precipitation. This is consistent with the Stothoff and Musgrove (2006) findings that recharge was systematically somewhat smaller, for a given precipitation level, in areas dominated by summer precipitation. Footprint Box estimates of MAI under alternative climates assume that the seasonality remains roughly similar to present conditions and would tend to overestimate MAI if summer precipitation increased significantly. Estimates of how much MAI may be overestimated are considered in this section. Change in temperature with elevation is not considered, which may influence the ratio of recharge efficiency between summer and winter precipitation.

The current seasonality patterns in the western portion of North America are shown in Figure 3-11, using the Global Historical Climate Network stations augmented by the Nevada Test Site Special Operations and Research Division network. The color of the marker representing each station indicates the seasonality at that station. Each month is denoted by a small triangle, with the radius of the triangle proportional to the fraction of annual precipitation in the month. The months are arranged like a clock, with January between 12 and 1 o'clock. The triangles are color-coded by season, with December through February colored blue, March through May colored green, June through August colored red, and September through November colored orange. There is a complete shift in seasonality from the winter-dominated southern California coast, where markers are predominantly blue, to the summer-dominated region of northern Mexico near the Arizona and New Mexico border, where markers are predominately red. Yucca Mountain lies in the transition zone between these regimes under current climatic conditions.

Summer insolation peaked in northern latitudes in the early Holocene, favoring more expansive monsoonal conditions than currently seen. Such conditions may have increased summer precipitation significantly relative to present. Sharpe (2003) attributes enhanced monsoonal conditions to approximately 3 percent of the next million years and suggests that stations in southern Arizona (Nogales) and New Mexico (Hobbs) may be analogous to monsoonal conditions at Yucca Mountain during such periods.

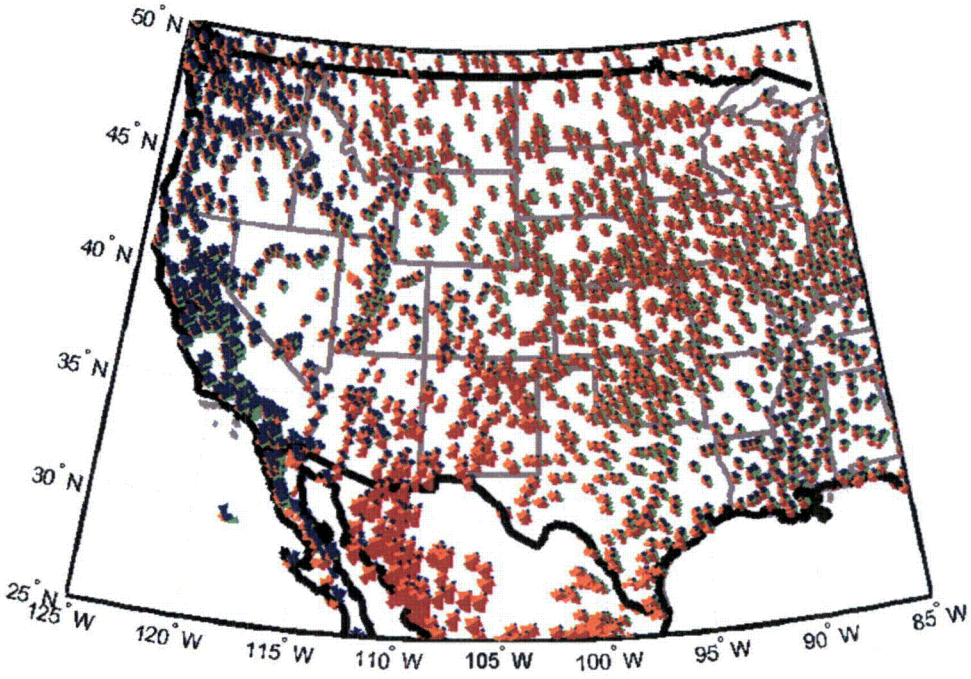

Figure 3-11. Monthly Fraction of Annual Precipitation at Global Historical Climate Network Stations. Color Denotes Season, With Blue = December-January-February, Green = March-April-May, Red = June-July-August, and Orange = September-October-November.

3.6.2 The Influence of Seasonality on Recharge

One way of assessing the effect of seasonal precipitation patterns is by describing the change in recharge from a fixed location with known seasonal precipitation and recharge patterns. Winograd, et al. (1998) used observations of stable isotopes from spring discharges to infer that summer (July through September) precipitation induced approximately 10 percent of annual recharge from approximately 30 percent of annual precipitation. The study by Winograd, et al. (1998) provides sufficient information to perform preliminary estimates of the effect of seasonality on recharge using the approximations developed in this section.

Based on the justification for a power-law relationship between MAP and MAI presented in Section 3.4, it is reasonable to assume that a power-law relationship also applies for each season, although the coefficients may vary with season. Using a first-order approximation to describe the change in recharge as precipitation seasonality changes where R is recharge, P is

precipitation, the *o* subscript represents a reference location with known seasonality and recharge, R^* is recharge at another location with a different seasonality

$$\log R^* = \log R_o + \frac{d \log R}{d \log P}(\log P^* - \log P_o) \tag{3-8}$$

and P^* is the MAP at the reference location that would yield R^* at the reference location Recharge enhancement factor F is determined by arranging Eq. (3-8) in the form

$$F = \frac{R^*}{R_o} = \left(\frac{P^*}{P_o}\right)^{\beta} \tag{3-9}$$

$$\beta = \frac{d \log R}{d \log P} \tag{3-10}$$

The Winograd, et al. (1998) observations allow the use of a two-season approximation to estimate P^*

$$P^* = a_w(P_w + \varepsilon P_s) \tag{3-11}$$

where

$$a_w = \frac{1}{1 - f_{so}(1 - \varepsilon)} \tag{3-12}$$

$$f_{so} = \frac{P_s}{P_s + P_w} \tag{3-13}$$

and where P_w and P_s are winter and summer precipitation, respectively; a_w is a weighting factor for winter seasonal precipitation effectiveness; ε is the efficiency of P_s relative to P_w at inducing recharge; and f_{so} is the fraction of annual precipitation occurring as summer precipitation. For this calculation, summer is referring to July through September and winter is referring to October through June. Both a_w and f_{so} are determined from the Winograd, et al. (1998) reference location of the Spring Mountains.

Approximately 28 and 20 percent of annual precipitation occurs in July through September in Las Vegas and Pahrump, Nevada, respectively. Assuming 10 percent of recharge occurs in these months, as indicated by the Winograd, et al. (1998) study, and f_{so} = 0.26, intermediate between Las Vegas and Pahrump, then ε = 0.32 and a_w = 1.22 in the Spring Mountains. Assuming that these values are also appropriate for Yucca Mountain, it is straightforward to estimate MAI for the Footprint Box if MAP were to change from present with different assumptions regarding seasonality change. Three cases are considered: (i) winter change, where summer precipitation stays fixed at present; (ii) summer change, where winter precipitation stays fixed at present; and (iii) same seasons, where the seasonality does not change. The same seasons case is simply the change in MAI with MAP for present-day MAT,

obtained by interpolating in the result table plotted in Figure 3-4. The other two cases use P^* to interpolate in the result table.

The three cases are shown in Figure 3-12. The winter change and same seasons curves are similar, because the fraction of summer precipitation is quite small for MAP greater than present. The summer change curve has a much shallower slope, because summer recharge efficiency is approximately one-third of winter recharge efficiency. This implies that while an expanded monsoonal climate may significantly increase MAP at Yucca Mountain, MAI would not increase significantly.

3.6.3 Regional Effects of Seasonality on Recharge

Another way of assessing the influence of seasonality is by examining how Footprint Box MAI would vary based on the present-day spatial distribution of MAP and on precipitation seasonality. The precipitation observations at the sites shown in Figure 3-11 provide a basis for estimating the spatial distribution of F at a reference elevation of 1,524 m [5,000 ft], which is

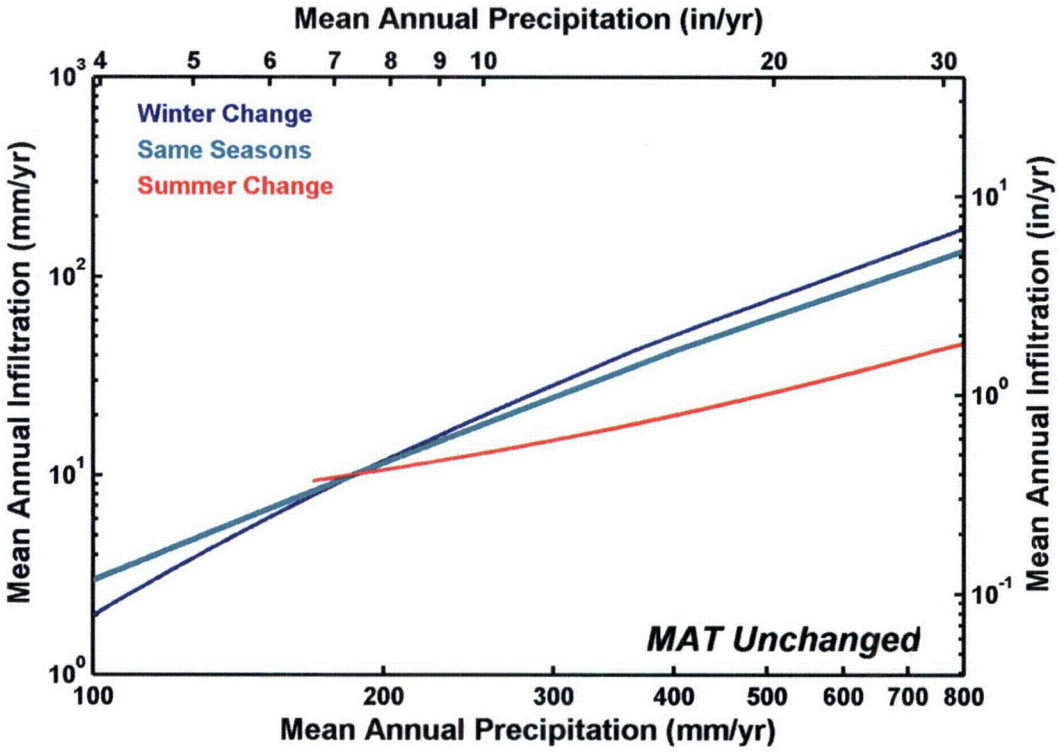

Figure 3-12. Footprint Box Decadal Infiltration Under Present Temperature But Changing Annual Precipitation. Winter Change and Summer Change Impose All Precipitation Change in Winter (October to June) or Summer (July to September), Respectively. Same Seasons Is the Curve From Figure 3-4 for Present Temperature.

approximately at the crest of Yucca Mountain. The approximation procedure has the following steps: (i) estimate P_w and P_s at the reference elevation for each observation site, (ii) estimate F at each observation site, and (iii) interpolate F between sites. No observation location lies precisely at the reference elevation; thus interpolation is necessary for estimating P_w and P_s. To illustrate, spatial interpolation is performed using

$$\log P = c_o + c_z Z + c_g N_g + c_t N_t + \sum_{i=1}^{N} c_i r_i \qquad (3\text{-}14)$$

where Z is elevation [km], N_g and N_t are normalized longitude and latitude, r_i is the radius (in longitude and latitude) from a pole, and the c coefficients are found through regression. As a first approximation, c_z is assumed to have a value of 0.28/km [0.45/mi], typical of regressions for the Yucca Mountain region, although c_z may be somewhat smaller across much of the area considered.

Estimated precipitation values at 1,524 m [5,000 ft] are shown in Figure 3-13(a) using a regular grid of poles (indicated with crosses) to pave the region between latitude 18° N and 55° N and between longitude 125° W and 95° W. The regression uses the full precipitation record for all stations with records of at least 20 years; these stations are indicated with dots. Contours are not drawn in areas with sparse coverage, such as northern Mexico. The grid is too coarse to resolve individual mountains or mountain ranges, but the regression suggests orographic effects from several mountain ranges including the Sierra Nevada and Cascade ranges. The regression also shows significant rainshadow effects in several locations including west-central Nevada.

The influence of seasonality on recharge is indicated in Figure 3-13(b) using a quadratic approximation for β as a function of MAP based on Footprint Box values with present-day MAT. The $F = 1$ contour passes through the Spring Mountain area, with Yucca Mountain experiencing slightly greater annual recharge efficiency. Precipitation seasonality typical of the southern California coastline has approximately 1.4 times greater recharge efficiency than the Spring Mountains. The U.S./Mexico border region near Arizona and New Mexico has approximately 0.6 times the recharge efficiency. These results are consistent with Figure 3-12.

3.6.4 Implications for Yucca Mountain

Seasonality change at Yucca Mountain may be largely due to differing strengths of the atmospheric highs in the Pacific and Atlantic Oceans, which mediate the position of the transition zone between winter- and summer-dominated precipitation. As summer precipitation waxes and wanes, recharge efficiency wanes and waxes. These preliminary assessments suggest that even a severalfold increase in summer precipitation would change MAI by only a small amount.

Postulated changes in MAP over glacial cycles have a greater effect on MAI than the seasonality ranges that are observed across the western United States today. Deflection of the jet stream to the south is thought to occur when continental ice caps are present. This type of deflection would tend to make the Yucca Mountain climate more like the climate to the north or northeast. If this is the case, the effect of seasonality change would be relatively small, probably increasing MAI by no more than 15 or 20 percent above the rate inferred from change

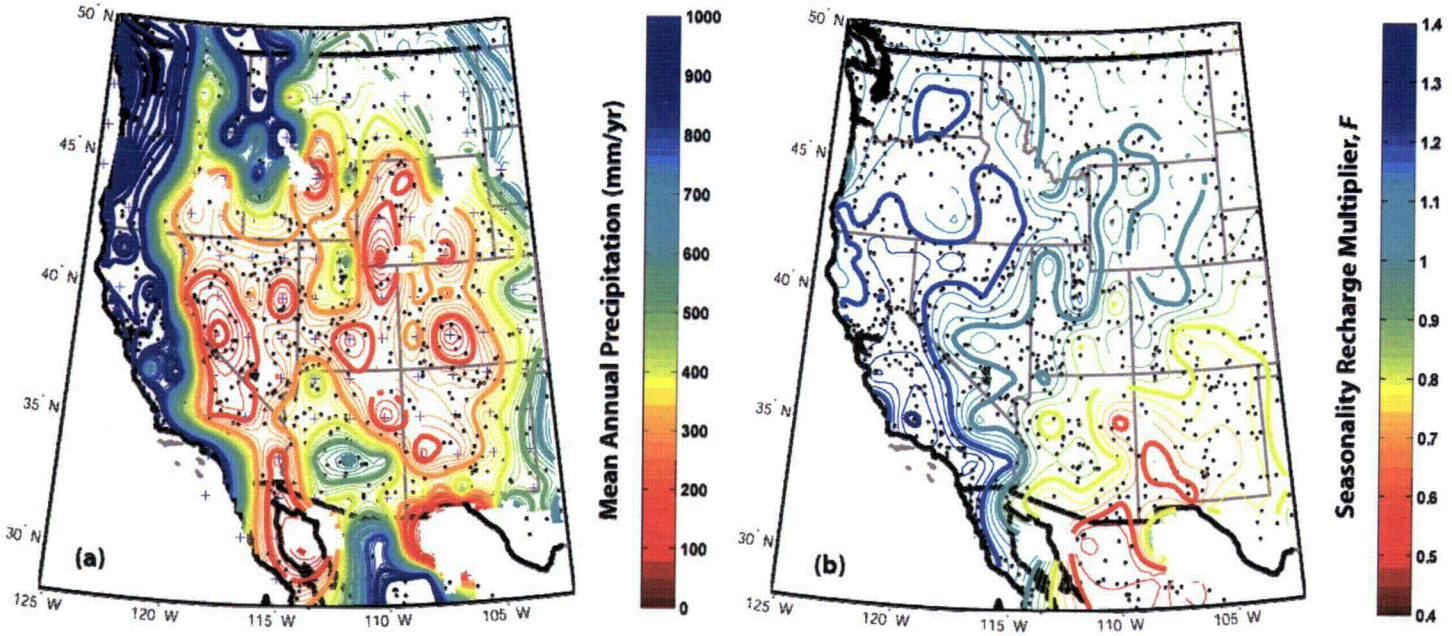

Figure 3-13. Estimated Spatial Distribution of (a) MAP in mm/yr and (b) *F*, the Multiplier for Mean Annual Recharge, both at 1,524 m [5,000 ft] Elevation. A 16-by-16 Grid of Poles Is Used to Interpolate MAP. [100 mm/yr = 3.94 in/yr]

in MAP and MAT based on initial values those directions that are only nominally larger than the value for F in the Yucca Mountain region.

3.7 Summary

A number of lines of evidence suggest that the recharge estimates provided by ITYM using the TPA Version 5.1 input files are consistent with available evidence. The best agreement is with available deep percolation flux estimates based on temperature profiles in deep boreholes. Estimates of deep percolation fluxes from perched water observations are also reasonably consistent with the ITYM estimates. There is reason to discount the observations from chloride mass balance calculations that use observations from both the saturated zone and the unsaturated zone matrix pore waters. Estimates from the saturated zone apparently agree with estimates using temperature profiles and perched waters, but the evidence suggests that the saturated zone waters are likely more representative of recharge from the Timber Mountain caldera than from Yucca Mountain. Estimates from unsaturated zone matrix pore waters are much smaller than estimates using temperature profiles, and there is reason to believe that the piston-flow assumption used for recharge analyses incompletely accounts for fast pathways, so that recharge estimates based on this assumption may be biased to the low side.

Tree-ring observations suggest that infiltration rates increase only slightly when variability is considered over several millennia, even though decadal-average MAI may vary severalfold over centuries to millennia.

Inferences drawn from long-term stable-isotope studies in the Spring Mountains, Nevada, suggest that winter precipitation is approximately three times more efficient than summer precipitation at producing recharge. This observation implies that a large change in summer precipitation may have only a modest effect on MAI. Precipitation seasonality strongly changes from the Pacific Coast of southern California to the border between Mexico and the United States in southern Arizona and New Mexico. No more than a threefold increase in MAI is estimated for a given elevation (neglecting temperature effects) when moving from strongly summer-dominated precipitation zones to strongly winter-dominated precipitation zones. Maximal effect at Yucca Mountain would be significantly less, because Yucca Mountain lies in the transition zone between the two extremes.

4 MILLION-YEAR INFILTRATION ESTIMATES

The climate and infiltration estimation method developed in Sections 2 and 3 are used in this section to estimate the probabilistic distribution of long-term-average net infiltration within the Footprint Box at Yucca Mountain. Two hypothetical future-climate scenarios are considered: a natural-change scenario and a global-warming scenario.

4.1 Natural-Change Scenario

The natural-change scenario assumes that prehistoric processes apply in the future without consideration of anthropogenic effects. Two independent approaches are used to estimate long-term-average Footprint Box infiltration: the Sharpe (2003) approach and the Orbital-Cycle Climate for Yucca Mountain (OCCYM)[1] approach.

The Sharpe (2003) approach is described in Section 2.1. Sharpe (2003) developed six representative climate states to describe representative periods during previous glacial cycles. Sharpe (2003) used evidence from previous glacial states to estimate climatic bounds at a reference Yucca Mountain elevation. The climatic uncertainty considered by Sharpe (2003) is encapsulated in uncertainty in the local climate for a reference elevation at Yucca Mountain given a global climate state. Sharpe (2003) also developed a sequence of climatic states using orbital parameters to describe the order and duration of the states.

The Sharpe (2003) interglacial and monsoon climate states were modified for the natural-change scenario to be consistent with the infiltration model described by Bechtel SAIC Company, LLC (2004c). The Bechtel SAIC Company, LLC (2004c) interglacial and monsoon climate states were translated from 1,400 m to 1,524 m [4,600 to 5,000 ft] using the Bechtel SAIC Company, LLC (2004c) mean annual precipitation (MAP)[2] and mean annual temperature (MAT)[3] distribution models. The upper bound precipitation for the monsoon state was further modified into an effective precipitation, using the procedure described in Section 3.6.2 to account for the reduced effectiveness of summer precipitation for inducing net infiltration. It is assumed that the lower bound monsoon precipitation has present-day seasonality, and the upper bound monsoon precipitation reflects an increase in summer precipitation from the lower bound. Effective annual precipitation for the upper bound is defined using the efficiencies estimated for Spring Mountain, as described in Section 3.6. The reference states to represent the Sharpe (2003) model with all adjustments are listed in Table 4-1.

The OCCYM approach is also based on Earth's orbital parameters to generate climatic sequences. Orbital parameters are linked to climate using sequences of numerically estimated global ice volumes that are based on insolation. Climate is estimated for reference ice volumes using independent evidence of previous climatic states and is interpolated between reference states assuming that climate smoothly changes with ice volume. Two reference states are

---

[1]The Orbital-Cycle Climate for Yucca Mountain module is referenced frequently throughout this chapter. The acronym OCCYM will be used.

[2]Mean annual precipitation is referenced frequently throughout this chapter. The acronym MAP will be used.

[3]Mean annual temperature is referenced frequently throughout this chapter. The acronym MAT will be used.

Table 4-1. Reference Climate States for 1,524 m [5,000 ft] Elevation at Yucca Mountain					
Model	Climate	Mean annual precipitation (mm/yr)		Mean annual temperature (°C)	
		Lower Bound	Upper Bound	Lower Bound	Upper Bound
OCCYM* (nominal)	Interglacial	201	241	15.7	17.7
	Full Glacial (OIS 6/16)	362	462	6.0	8.8
OCCYM* (cool)	Interglacial	201	241	13.9	16.9
	Full Glacial (OIS 6/16)	362	462	4.7	7.5
Sharpe‡	Interglacial	201	288	13.88	16.98
	Monsoon	204	300	13.88	15.08
	Intermediate	209	432	7.58	8.23
	Full Glacial (OIS 6/16)	320	513	0.00	4.70
	Full Glacial (OIS 2/4)	243	320	4.70	7.70
	Full Glacial (OIS 8/10)	432	537	7.90	8.80
	Million-Year Average	213	389	7.55	9.01

*Orbital-Cycle climate for Yucca Mountain (OCCYM)
†Sharpe, S. "Future Climate Analysis—10,000 Years to 1,000,000 Years After Present." MOD–01–001. Rev. 01. Reno, Nevada: Desert Research Institute. 2003.
100 mm/yr = 3.94 in/yr; °F = (9/5)°C + 32

defined: (i) interglacial and (ii) full glacial with MIS 6/16 climatic parameters. These reference global ice volume to orbital parameters, (ii) regional climate in the Yucca Mountain given a global ice volume, (iii) local climate at Yucca Mountain given the regional climate, and (iv) areal-average mean annual infiltration in the Yucca Mountain Footprint Box given the local climate. Note that the MAP limits described in Table 3-3 represent the midpoint of the triangular distribution used to account for the uncertainty of local climate given the regional climate, as described in Section 2.3.3.

The same abstracted representation of Millennial-Scale Footprint Box mean annual infiltration (MAI)[4] is used for both the Sharpe (2003) and OCCYM approaches. A truncated lognormal distribution is used to describe the uncertainty in Decadal-Scale areal-average MAI, developed using the average MAI and average standard deviation of MAI for all grid blocks within the Footprint Box in the Infiltration Tabulator for Yucca Mountain (ITYM)[5] model. The lowest and highest 0.5 percent of the full lognormal distribution are truncated. The Decadal-Scale

[4]Mean annual infiltration is referenced frequently throughout this chapter. The acronym MAI will be used.

[5]The Infiltration Tabulator for Yucca Mountain model is referenced frequently throughout this chapter. The acronym ITYM will be used.

abstraction is described in Section 3.3. Millennial-Scale MAI is derived from Decadal-Scale MAI by multiplying all MAI values by 1.06 to account for millennial-scale climatic variability, as described in Section 3.5.

The natural-change scenario using the two approaches is summarized in Figure 4-1a, which presents the cumulative probability distribution for million-year-average Footprint Box MAI. The nominal OCCYM climate case described in Section 2.3.4 is shown in Figure 4-1. All six OCCYM ice-volume sequences are drawn as dotted lines for each representative interglacial ice volume (i.e., f = 0, 0.2, and 0.4, where f is normalized ice volume). The average of the six sequences is shown as a thick line for all three of the OCCYM interglacial ice volumes, assuming that each sequence is equally likely. The Sharpe (2003) approach is also shown as a heavy line, almost completely obscuring the nominal case of the OCCYM approach.

The range in any given distribution is more than an order of magnitude greater than the difference between the mean values, and there is little difference between the shape of the OCCYM and Sharpe (2003) curves. These characteristics suggest that climate uncertainty is not the determining factor for the distribution. The uncertainty distribution for Footprint Box MAI shown in Figure 3-3 has a much wider range in MAI than the uncertainty distribution for long-term-average MAP shown in Figure 2-7(a), suggesting that infiltration uncertainty dominates climate uncertainty in determining overall uncertainty.

Figure 4-1b, in which all uncertain climatic parameters were set to their median values, is almost identical to Figure 4-1a, but with slightly smaller infiltration rates and slightly smaller dispersion in estimates. The comparison between the two sets of curves further suggests that infiltration uncertainty dominates climate uncertainty in determining overall uncertainty. The slight difference in median infiltration rates suggests that an increase in uncertainty increases the expected value of MAI, similar to the finding in Section 3.5 that temporal variability in climate increases the expected value of MAI.

A reference distribution in Figure 4-1b is derived from million-year-average MAP and MAT in the Sharpe (2003) model, using MAP = 311 mm/yr [12.2 in/yr] and MAT = 8.62 °C [47.5 °F]. The reference distribution is derived by time-averaging the median values in the Sharpe (2003) climate states. The differences between the MAI distributions from the Sharpe (2003) model suggest that the combined effect of temporal variability and uncertainty in climate over a glacial cycle increases the mean expected average MAI by approximately 8 percent, with the two factors having essentially equal influences.

Figure 4-2 shows the best estimate of million-year-average Footprint Box net infiltration from the nominal and cool OCCYM models, incorporating all of the considered sources of uncertainty and temporal variability. The nominal OCCYM distribution is calculated from the 18 individual OCCYM distributions shown in Figure 4-1(a), assuming that each of the 18 cases is equally likely. The cool OCCYM distribution is calculated using the same procedure with the alternative MAT values described in Section 2.3.4. The Sharpe (2003) model distribution from Figure 4-1 is shown for reference. Estimated statistics for the MAP, MAT, and MAI distributions are presented in Table 4-2.

Remarkably, the nominal OCCYM and Sharpe (2003) distributions are essentially identical, and the cool OCCYM distribution is only slightly larger. As it turns out, the long-term-average MAP and MAT values for the different climate representations are quite similar, despite the different

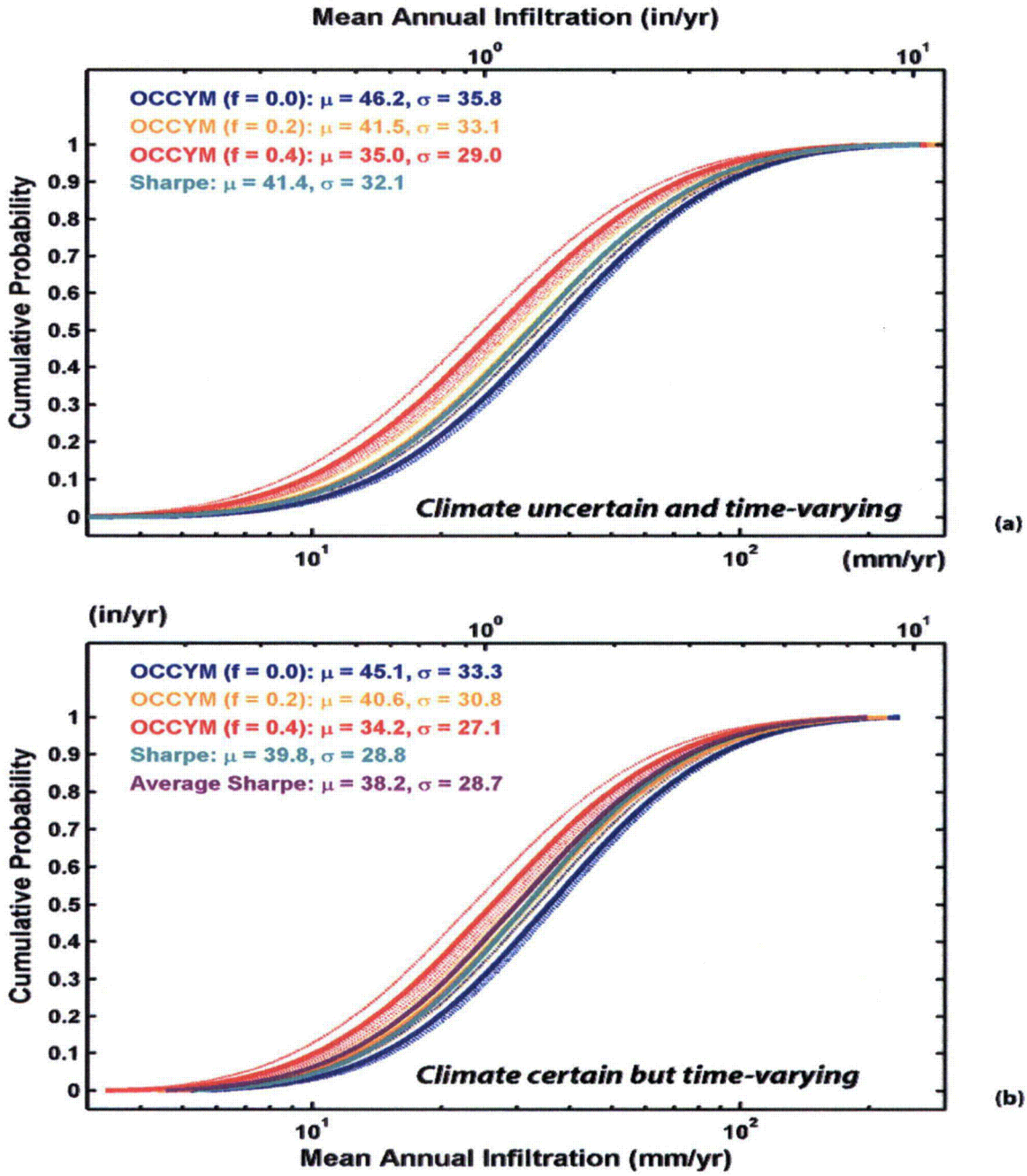

Figure 4-1. Cumulative Probability Distributions for Million-Year-Average Footprint Box MAI. (a) Considering Climatic Variability and Climatic Uncertainty (N_p = 10, N_t = 4, N_d = 5, and N_i = 50). (b) Considering Climatic Variability but Not Climatic Uncertainty (N_p = N_t = N_d = 1 and N_i = 1,000). "Average Sharpe" Denotes a Time-Averaged Climate Based on Medians of Sharpe (2003) Climate States. [100 mm/yr = 3.94 in/yr].

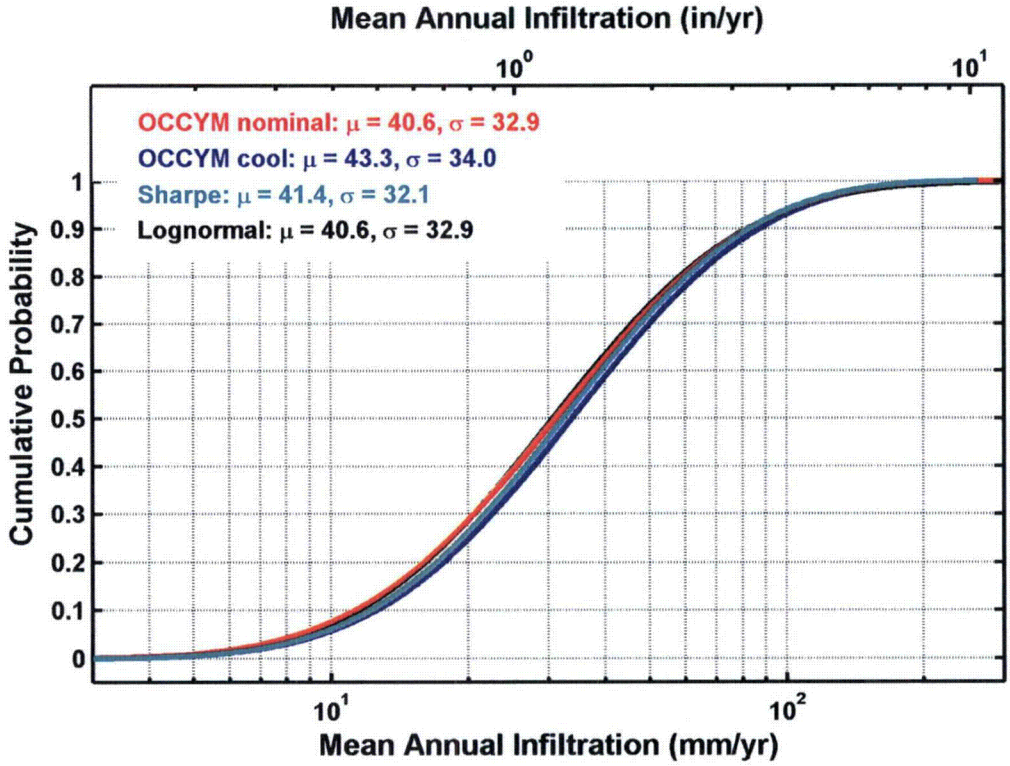

Figure 4-2. Best Estimates for Cumulative Probability Distribution of Million-Year-Average Footprint Box MAI for Both Independent Climate Models. Estimates use N_p = 10, N_t = 4, N_d = 5, and N_i = 50.

assumptions in creating the distributions. As a result, the uncertainties in estimating Footprint Box infiltration given climate are far larger than the differences in estimated future climatic conditions.

The black line in Figure 4-2 represents a lognormal distribution approximately describing the nominal OCCYM distribution. A lognormal distribution for variable x is equivalent to a normal distribution for $y = \log(x)$, which can be described in terms of the normalized variable u

$$u = \frac{y - \mu_y}{\sigma_y} \tag{4-1}$$

where μ_y is the mean value of y, and σ_y is the standard deviation of y. These parameters are estimated using Eqs. (2-6) and (2-7) using log-transformed values of MAI.

The additional uncertainty and temporal variability in the OCCYM and Sharpe (2003) approaches slightly widen the spread in expected MAI (increases σ_y) relative to the long-term-average climate, as well as increasing the median value.

Table 4-2. Summary of Statistics for Natural-Cycle Expected-Parameter Distributions*							
Parameter	**Model**	μ_x	σ_x	μ_y	σ_y	10^{μ_y}	σ_x/μ_x
Mean annual precipitation [mm/yr]	OCCYM† (f = 0.0)	339	45.9	2.53	0.0588	336	0.136
	OCCYM (f = 0.2)	323	43.8	2.51	0.0588	320	0.136
	OCCYM (f = 0.4)	299	40.6	2.47	0.0590	296	0.136
	OCCYM (nominal)	320	46.5	2.50	0.0630	317	0.145
	Sharpe‡	315	51.9	2.49	0.0715	311	0.165
Mean annual temperature [°C]	OCCYM (f = 0.0)	10.1	0.59				0.059
	OCCYM (f = 0.2)	10.8	0.57				0.052
	OCCYM (f = 0.4)	12.0	0.55				0.046
	OCCYM (nominal)	11.0	0.94				0.086
	OCCYM (cool)	9.7	1.01				0.104
	Sharpe‡	8.6	0.40				0.046
Mean annual infiltration with uncertain climate	OCCYM (f = 0.0)	45.8	35.6	1.55	0.319	35.2	0.777
	OCCYM (f = 0.2)	41.2	32.9	1.50	0.326	31.3	0.798
	OCCYM (f = 0.4)	34.8	28.8	1.41	0.337	26.0	0.829
	OCCYM (nominal)	40.6	32.9	1.49	0.332	30.6	0.810
	OCCYM (cool)	43.3	34.0	1.52	0.323	33.1	0.784
	Sharpe‡	41.4	32.1	1.50	0.319	31.9	0.776
Mean annual infiltration with certain climate	OCCYM (nominal)	39.7	30.7	1.49	0.314	30.7	0.773
	OCCYM (cool)	42.3	31.6	1.52	0.304	33.3	0.747
	Sharpe‡	39.8	28.8	1.50	0.293	31.8	0.724
Mean annual infiltration with steady and certain climate	OCCYM (nominal)	37.7	29.9	1.46	0.320	28.9	0.793
	OCCYM (cool)	40.4	31.0	1.50	0.310	31.5	0.766
	Sharpe‡	38.2	28.7	1.48	0.305	29.9	0.753

*The mean and standard deviation of the variable are denoted by μ_x and σ_x, respectively. The mean and standard deviation of the log-transformed variable are denoted by μ_y and σ_y, respectively.
†Orbital-Cycle Climate for Yucca Mountain (OCCYM)
‡Sharpe, S. "Future Climate Analysis—10,000 Years to 1,000,000 Years After Present." MOD–01–001. Rev. 01. Reno, Nevada: Desert Research Institute. 2003.
100 mm/yr = 3.94 in/yr; °F = (9/5)°C + 32

The lognormal distribution is a reasonable approximation to both best estimate distributions in the range of cumulative probability of $u < 2$. A lognormal distribution implies that y may approach infinity at some low level of probability, which is not physically possible because it implies MAI would exceed MAP. The long tail of the lognormal distribution begins to deviate significantly from the best estimate distributions above $u = 2$, but the lognormal approximation differs from the best estimate distributions by less than 5 percent throughout the range of $-3 < u < 2$, which contains 97.6 percent of the probability. Note that the best estimate distributions are themselves overestimates of expected MAI in the high end of the distribution as discussed in Section 3.3, because similar deviation in the high end of the distribution also occurs when Footprint Box MAI is approximated using a lognormal distribution. Accordingly, a lognormal approximation to long-term-average expected Footprint Box MAI significantly overestimates MAI at the high end of the distribution, even though the middle of the distribution may be well captured.

4.2 Global-Warming Scenario

Global-warming through anthropogenic effects may result in the equivalent of an extended interglacial period, especially because orbital forcings will be smaller for the next 500,000 years than were typical for the past 1 million years (Walter, 2005). Global warming may also increase summer heating in the North American continent interior and in the tropics, promoting atmospheric patterns that lead to a stronger summer monsoon and increased summer precipitation at Yucca Mountain.

An extended period of either interglacial or monsoonal conditions would reduce the million-year-average MAI, because the entire range of climates for both conditions is warmer and drier than the million-year-average climate. A simple calculation suggests that only a small reduction in million-year-average MAI would be expected because of an extended initial low-infiltration period due to anthropogenic forcings. A time-weighted average of MAI, using an initial "interglacial" MAI and the million-year-average MAI, provides a reasonable approximation to replacing actual infiltration with a reduced infiltration for part of the total period. The fraction of long-term-average MAI that would be experienced with an extended interglacial period, F_I, is simply the ratio of the time-weighted average MAI to the million-year-average MAI

$$F_I = \frac{I_{ig} T_{ig} + I_{lta}(T - T_{ig})}{I_{lta} T} \tag{4-2}$$

where I_{ig} is interglacial MAI, I_{lta} is long-term-average MAI, T is the total period (1 million years), and T_{ig} is the duration of the protracted interglacial period.

Setting I_{ig} to 0 mm/yr [0 in/yr] provides an extreme bounding condition. With this extreme bounding condition, $F_I = (T - T_{ig}) / T$, so that net infiltration with an extended interglacial period is reduced from the natural-change case by the fraction of the million years that the extended interglacial period is active. For example, a 10,000-year initial interglacial period would reduce F_I to 0.99, and a 100,000-year initial interglacial period would reduce F_I to 0.9. This implies that even an extended initial interglacial or monsoonal period would reduce million-year-average MAI by only a small fraction of the range in uncertainty for MAI.

4.3 Summary

In Section r, the climate and infiltration estimation methods developed in Sections 2 and 3 are used to estimate long-term net infiltration at Yucca Mountain and examine the impact of hypothetical future-climate scenarios.

The natural-change scenario presented in Section 4.1 assumes that prehistoric processes apply in the future without influence of anthropogenic effects. The natural-change scenario uses two independent representations for future climate states to derive uncertainties in Yucca Mountain climate. Million-year-average future climates for the models are similar, but not identical. Both climate representations are used to drive the Millennial-Scale model for Footprint Box net infiltration derived in Section 3. Despite the significant differences between the derivation of the climate models, expected million-year-average Footprint Box net infiltration is 41 mm/yr [1.6 in/yr] for both climate models and the coeffients of variation differ by less than 5 percent. This remarkable result is because the uncertainty in Footprint Box infiltration, given climate, greatly exceeds the uncertainty in estimates of future climate.

A lognormal distribution with mean of 40.6 mm/yr [1.60 in/yr] and coefficient of variation of 0.810 is within 5 percent of the best estimate distribution everywhere except in the extremes of the distribution. If an equivalent steady-state climate is assumed with median values for all uncertain climatic parameters, the corresponding lognormal distribution has a mean of 37.7 mm/yr [1.48 in/yr] and coefficient of variation of 0.793. Climatic variability and uncertainty over multiple glacial cycles increase expected million-year-average net infiltration by less than 9 percent and minimally increase infiltration uncertainty.

Global warming through anthropogenic effects may result in the equivalent of an extended interglacial or monsoonal period, especially because the orbital effect will be smaller for the next 500,000 years than were typical for the past 1 million years. The influence of a protracted interglacial period is considered in Section 4.2. To a first approximation, net infiltration with an extended interglacial is reduced from the natural-change case by the fraction of the million years that the extended interglacial is active.

5 SUMMARY AND CONCLUSIONS

Yucca Mountain, Nevada, has been studied for more than 20 years as a potential location for geologic emplacement of high-level nuclear waste. Assessments of the potential performance of the repository indicate that water fluxes contacting waste can strongly influence repository performance, leading to interest in quantifying the deep percolation flux of water at the repository horizon. Since net infiltration is the ultimate source of water at the repository horizon, the average net infiltration flux above the repository footprint can be used to estimate average deep percolation fluxes at the potential repository horizon over long periods of time.

Net infiltration at Yucca Mountain is spatially heterogeneous and is likely to significantly vary in magnitude over the next million years due to natural and anthropogenic changes in climate. Both the spatial patterns and the temporal change in net infiltration are uncertain; thus long-term-average net infiltration is also inherently uncertain. In this report, infiltration uncertainty at Yucca Mountain over the next million years is quantified by estimating both climatic uncertainty and net infiltration uncertainty given a climatic condition. The combination of these two uncertainties yields the overall uncertainty on net infiltration.

Two independent methods are used to estimate sequences of future climatic conditions at Yucca Mountain, as discussed in Section 2. The Sharpe (2003) model provides one method for estimating future climatic conditions, by correlating inferred past climatic conditions to insolation sequences. The Orbital-Cycle Climate for Yucca Mountain (OCCYM)[1] model provides an independent method, using similar insolation sequences to estimate global ice volume and correlating inferred past climatic conditions to global ice volume. The two models produce similar estimates of present-day climate, but somewhat different estimates of glacial conditions. Several lines of evidence suggest that the Sharpe (2003) model may overestimate the difference in climate from present-day conditions to full-glacial conditions. The two methods estimate similar long-term-average mean annual precipitation (MAP)[2] and mean annual temperature (MAT)[3] for the next million years, however, because the relative frequency of the different climatic states remains relatively unchanged in the Sharpe (2003) model, whereas the OCCYM model suggests a trend toward enhanced glacial conditions.

Both climate models use the same estimates of decadal-average infiltration for a given climate to estimate long-term-average infiltration, as discussed in Section 3. These estimates are calculated using the Infiltration Tabulator for Yucca Mountain (ITYM)[4] model, which considers uncertainty in site properties at a relatively fine spatial scale. A lognormal distribution provides a reasonable approximation to the uncertainty in areal-average net infiltration given a climatic condition. The lognormal distribution must be truncated at the high end, however, so that net infiltration is less than precipitation. A comparison in Section 3 between ITYM estimates and

---

[1]The Orbital-Cycle Climate for Yucca Mountain module is referenced frequently throughout this chapter. The acronym OCCYM will be used.

[2]Mean annual precipitation is referenced frequently throughout this chapter. The acronym MAP will be used.

[3]Mean annual temperature is referenced frequently throughout this chapter. The acronym MAT will be used.

[4]The Infiltration Tabulator for Yucca Mountain model is referenced frequently throughout this chapter. The acronym ITYM will be used.

available site and regional infiltration and recharge estimates suggests that (i) ITYM estimates are consistent with site observations, and (ii) ITYM estimates are consistent with regional elevation-dependent climatic change.

Tree-ring observations are used in Section 3.5 to assess the influence of climatic variability over millennial-scale periods during the Holocene. The tree-ring observations suggest that decadal-average precipitation may vary significantly over several millennia even though insolation patterns vary little over the same period. The ITYM model suggests that decadal-average net infiltration may vary severalfold over millennia because of precipitation variability. However, long-term-average net infiltration is only nominally increased relative to an equivalent steady state when this climatic variation is considered. A scaling factor is introduced to the calculations that provides a nominal systematic increase in net infiltration when averaging from the decadal to the millennial scales.

Precipitation seasonality changes are inferred to occur over orbital cycles, such as increased summer precipitation during interglacial periods with particularly intense summer insolation. A bounding calculation is presented in Section 3.6, suggesting that even a large increase in summer monsoon precipitation may have only a minimal impact on net infiltration.

The climate and infiltration models are combined in Section 4 to estimate long-term-average net infiltration. A pattern of infiltration uncertainty dominating climate uncertainty for these Yucca Mountain models clearly emerges. The set of expected net infiltration estimates from different representations of climate form a band of estimates, with no more than a factor of two difference between the low and high net infiltration means, and the best estimates from the Sharpe (2003) and OCCYM models are essentially identical. In contrast, there is well over an order of magnitude range in areal-average net infiltration estimates for a given climatic representation using the ITYM model, consistent with the CRWMS M&O (2003b) uncertainty analyses using an independent Yucca Mountain infiltration model.

A natural-cycle analysis presented in Section 4 used past climatic cycles extrapolated over the next million years (from Section 2) and the ITYM infiltration model (from Section 3) to estimate repository footprint-average million-year-average net infiltration. Best estimate probability distributions using the OCCYM climate model have a mean of 40.6 mm/yr [1.60 in/yr] and standard deviation of 32.9 mm/yr [1.30 in/yr]; with the Sharpe (2003) climate model, the distributions have a mean of 41.4 mm/yr [1.63 in/yr] and standard deviation of 32.1 mm/yr [1.26 in/yr]. Both distributions are well described using a lognormal distribution, with less than 5 percent error when $-3 < u < 2$, where u is the normal variate. The medians are 31 and 32 mm/yr [1.2 and 1.3in/yr] for the nominal OCCYM and Sharpe (2003) models, respectively.

A global-warming analysis presented in Section 4 examined the effect of an extended period of either interglacial conditions or enhanced monsoon conditions on million-year-average net infiltration. Both climatic conditions are anticipated to produce smaller infiltration rates than the long-term-average infiltration rate. Although the enhanced-monsoon climate may have significantly increased precipitation relative to the interglacial climate, the analysis in Section 3.6 suggests that increased summer precipitation minimally influences infiltration. The maximal change in million-year-average net infiltration would occur if infiltration ceased during the global warming period—an extreme assumption useful for illustration. If a zero-infiltration period lasted for 10 thousand years, long-term-average infiltration would decrease by 1 percent; if a

zero-infiltration period lasted for 100,000 years, long-term-average infiltration would decrease by 10 percent. These changes are small relative to the uncertainty in net infiltration.

The analyses in this document clearly suggest that uncertainty in estimates of million-year-average net infiltration for Yucca Mountain is dominated by infiltration model uncertainty. Under present-day conditions, the ITYM model estimates differ from the best estimate from regional studies by approximately a factor of 2, implying that alternative infiltration models may have best estimates for million-year-average net infiltration that filter, from the ITYM model by as much as a factor of 2. This difference is small relative to the overall range of infiltration uncertainty. It is also possible that alternative infiltration models may have a different estimate of the range of uncertainty, which can be reduced by incorporating additional information. Comparing the DOE uncertainty analysis to ITYM results suggests that estimates of the range in uncertainty may vary by roughly a factor of 2, again small relative to the overall range of infiltration uncertainty.

Based on the analyses in this report, the uncertainty in areal-average net infiltration over the next million years within a footprint box circumscribing the potential Yucca Mountain repository footprint is reasonably described with a lognormal distribution having a mean of 41 mm/yr [1.6 in/yr] or median of 31 mm/yr [1.2 in/yr] and standard deviation of 33 mm/yr [1.3 in/yr].

6 REFERENCES

Bagtzoglou, A.C. "Perched Water Bodies in Arid Environments and Their Role as Hydrologic Constraints for Recharge Rate Estimation: Part 1—A Modeling Methodology." *Environmental Forensics.* Vol. 4, No.1. pp. 39–46. 2003.

Barnola, J.M., D. Raynaud, C. Lorius, and N.I. Barkov. Historical CO_2 record from the Vostok ice core. In Trends: A Compendium of Data on Global Change. Carbon Dioxide Information Analysis Center, Oak Ridge National Laboratory, U.S. Department of Energy, Oak Ridge, Tenn., U.S.A. 2003

Bechtel SAIC Company, LLC. "Future Climate Analysis." ANL–NBS–HS–000008. Rev. 01. Las Vegas, Nevada: Bechtel SAIC Company, LLC. 2004a.

———. "Simulation of Net Infiltration for Present-Day and Potential Future Climates." MDL–NBS–HS–000023. Rev. 00. Las Vegas, Nevada: Bechtel SAIC Company, LLC. 2004b

———. "Technical Basis Document No. 1: Climate and Infiltration." Las Vegas, Nevada: Bechtel SAIC Company, LLC. 2004c.

Benson, L., M. Kashgarian, R. Rye, S. Lund, F. Paillet, J. Smoot, C. Kester, S. Mensing, D. Meko, and S. Lindström. "Holocene Multidecadal and Multicentennial Droughts Affecting Northern California and Nevada." *Quaternary Science Reviews.* Vol. 21. pp. 659–682. 2002.

Berger, A. and M.F. Loutre. "Insolation Values for the Climate of the Last 10 Million Years." *Quaternary Science Reviews.* Vol. 10, No. 4. pp. 297–317. 1991.

Bischoff, J.L., K.M. Menking, J.P. Fitts, and J.A. Fitzpatrick. "Climatic Oscillations 10,000–155,000 Year B.P. at Owens Lake, California Reflected in Glacial Rock Flour Abundance and Lake Salinity in Core OL-92." *Quaternary Research.* Vol. 48. pp. 313–325. 1997.

Bodvarsson, G.S., E. Kwicklis, C. Shan, and Y.-S. Wu. "Estimation of Percolation Flux From Borehole Temperature Data at Yucca Mountain, Nevada." *Journal of Contaminant Hydrology.* Vols. 62–63. pp. 3–22. 2003.

Constantz, J., S.W. Tyler, and E. Kwicklis. "Temperature-Profile Methods for Estimating Percolation Rates in Arid Environments." *Vadose Zone Journal.* Vol. 2. pp. 12–24. 2003.

CRWMS M&O. "Analysis of Geochemical Data for the Unsaturated Zone." ANL–NBS–HS–000017. Rev. 00 ICN 02. Las Vegas, Nevada: CRWMS M&O. 2003a.

———. "Analysis of Infiltration Uncertainty." ANL–NBS–HS–000027. Rev. 01. Las Vegas, Nevada: CRWMS M&O. 2003b.

———. "Geochemical and Isotopic Constraints on Groundwater Flow Directions, Mixing, and Recharge at Yucca Mountain, Nevada." ANL–NBS–HS–000021. Rev. 00. Las Vegas, Nevada: CRWMS M&O. 2000.

D'Agnese, F.A., G.M. O'Brien, C.C. Faunt, and C.A. San Juan. "Simulated Effects of Climate Change on the Death Valley Regional Groundwater Flow System." Nevada and California. U.S. Geological Survey Water-Resources Investigations Report No. 98-4041. 1999.

DOE. DOE/RW–0508. "Viability Assessment of a Repository at Yucca Mountain: Total-System Performance Assessment." Las Vegas, Nevada: DOE. 1998.

Forester, R.M., J.P. Bradbury, C. Carter, A.B. Elvidge-Tuma, M.L. Hemphill, S.C. Lundstrom, S.A. Mahan, B.D. Marshall, L.A. Neymark, J.B. Paces, S.E. Sharpe, J.F. Whelan, and P.E. Wigand. "The Climatic and Hydrologic History of Southern Nevada During the Late Quaternary." U.S. Geological Survey Open-File Report No. 98-635. 1999.

French, R.H. "Daily, Seasonal, and Annual Precipitation at the Nevada Test Site, Nevada." Publication No. 45042. Reno, Nevada: Desert Research Institute. 1986.

Gee, G.W., P.J. Wierenga, B.J. Andraski, M.H. Young, M.J. Fayer, and M.L. Rockhold. "Variations in Water Balance and Recharge Potential at Three Western Desert Sites." *Soil Science Society of America Journal.* Vol. 58, No. 1. pp. 63–72. 1994.

Hevesi, J.A., A.L. Flint, and J.D. Istok. "Precipitation Estimation in Mountainous Terrain Using Multivariate Geostatistics: Part II—Isohyetal Maps." *Journal of Applied Meteorology.* Vol. 31, No. 7. pp. 677–688. 1992a.

Hevesi, J.A., J.D. Istok, and A.L. Flint. "Precipitation Estimation in Mountainous Terrain Using Multivariate Geostatistics: Part I—Structural Analysis. *Journal of Applied Meteorology.* Vol. 31, No. 7. pp. 661–676. 1992b.

Hostetler, S.W. and L.V. Benson. "Paleoclimatic Implications of the High Stand of Lake Lahontan Derived From Models of Evaporation and Lake Level." *Climate Dynamics.* Vol. 4, No. 3. pp. 207–217. 1990.

Hughes, M.W. and L.J. Graumlich. "Multi-Millennial Nevada Precipitation Reconstruction." IGB AGES/World Data Center for Paleo Climatology Data Contribution Series 2000–049. Boulder, Colorado: NOAA/NGDC Paleoclimatology Program. 2000.

Hughes, M.W. and L.J. Graumlich. "Multi-Millennial Dendroclimatic Studies From the Western United States." *Climatic Variations and Forcing Mechanisms of the Last 2000 Years.* R.S. Bradley, P.D. Jones, and J. Jouzel eds. Vol. 141. pp. 109–124. New York City, New York: Springer-Verlag. 1996.

Imbrie, J., A. McIntyre, and A.C. Mix. "Oceanic Response to Orbital Forcing in the Late Quaternary: Observational and Experimental Strategies." A. Berger, S.H. Schneider, and J.-C. Duplessy eds. *Climate and Geo-Sciences, A Challenge for Science and Society in the 21st Century.* NATO ASI Series C. pp. 121–164. Boston, Massachusetts: Kluwer Academic Publishing Company. 1989.

Kaufman, D.S., S.C. Porter, and A.R. Gillespie. "Quaternary Alpine Glaciation in Alaska, the Pacific Northwest, Sierra Nevada, and Hawaii." A.R. Gillespie, S.C. Porter, and B.F. Atwater eds. *The Quaternary Period in the United States*. pp. 77–103. Amsterdam, The Netherlands: Elsevier Science Publishers B.V. 2003.

Kessler, M.A., R.S. Anderson, and G.M. Stock. "Modeling Topographic and Climatic Control of East-West Asymmetry in Sierra Nevada Glacier Length During the Last Glacial Maximum." *Journal of Geophysical Research*. Vol. 111. Part F02002. 2006.

Lea, D.W., D.K. Pak, and H.J. Spero. "Climate Impact of Late Quaternary Equatorial Pacific Sea Surface Temperature Variations." *Science*. Vol. 289. pp. 1,719–1,724. 2000.

LaMarche, V.C., Jr. "Paleoclimatic Inferences From Long Tree-Ring Records." *Science*. Vol. 183. No 4129. pp. 1,043–1,048. 1976.

Lichty, R.W. and P.W. McKinley. "Estimates of Groundwater Recharge Rates for Two Small Basins in Central Nevada." U.S. Geological Survey Water-Resources Investigations Report No. 94-4104. 1995.

Lloyd, A.H. and L.J. Graumlich. "Holocene Dynamics of Treeline Forests in the Sierra Nevada." *Ecology*. Vol. 78, No. 4. pp. 1199–1210. 1997.

Loehle, C. Predicting Pleistocene climate from vegetation in North America. *Climate of the Past* 3, pp. 109–118. 2007.

Lopes, T.J. and D.M. Evetts. "Groundwater Pumpage and Artificial Recharge Estimates for Calendar Year 2000 and Average Annual Natural Recharge and Interbasin Flow by Hydrographic Area, Nevada." U.S. Geological Survey Scientific Investigations Report No. 2004-5239. 2004.

Maxey, G.B. and T.E. Eakin. "Groundwater in White River Valley, White Pine, Nye, and Lincoln Counties, Nevada." Bulletin No. 8. Carson City, Nevada: Department of Conservation and Natural Resources, State of Nevada. 1949.

Moore, J.G. *"Exploring the Highest Sierra."* Stanford, California: Stanford University Press. 2000.

Nichols, W.D. "Regional Groundwater Evapotranspiration and Groundwater Budgets, Great Basin, Nevada. Professional Paper No. 1628. Denver, Colorado: U.S. Geological Survey. 2000.

———. "Geohydrology of the Unsaturated Zone at the Burial Site for Low-Level Radioactive Waste Near Beatty, Nye County, Nevada." Water-Supply Paper No. 2312. Reston, Virginia: U.S. Geological Survey. 1987.

NRC. "Risk Insights Baseline Report." ML040560162. Washington, DC: NRC. 2004. <www.nrc.gov/waste/hlw-disposal/reg-initiatives/resolve-key-tech-issues.html.>

Petit, J.R., J. Jouzel, D. Raynaud, N.I. Barkov, J.-M. Barnola, I. Basile, M. Bender, J. Chappellaz, M. Davis, G. Delaygue, M. Delmotte, V.M. Kotlyakov, M. Legrand, V.Y. Lipenkov, C. Lorius, L. Pépin, C. Riz, E. Saltzman, and M. Stievenard. "Climate and Atmospheric History of the Past 420,000 Years from the Vostok Ice Core, Antarctica." *Nature*. Vol. 399. pp. 429–436. 1999.

Reheis, M.C. "Highest Pluvial-Lake Shorelines and Pleistocene Climate of the Western Great Basin." *Quaternary Research*. Vol. 52, No. 2. pp 196–205. 1999.

Roper, L.D. "Insolation Codes for Windows." 2003. <http://roperld.com/science/InsolationCodes.htm.>

Russell, C.E., J.W. Hess, and S.W. Tyler. "Hydrogeologic Investigations of Flow in Fractured Tuffs, Rainier Mesa, Nevada Test Site." *Flow and Transport Through Unsaturated Fractured Rock*. D.B. Evans and T.J. Nicholson eds. Geophysical Monograph No. 42. pp. 43–50. Washington, DC: American Geophysical Union. 1987.

Sass, J.H., A.H. Lachenbruch, W.W. Dudley, Jr., S.S. Priest, and R.J. Munroe. "Temperature, Thermal Conductivity, and Heat Flow Near Yucca Mountain, Nevada: Some Tectonic and Hydrologic Implications." U.S. Geological Survey Open-File Report No. 87-649. 1988.

Sharpe, S. "Future Climate Analysis—10,000 Years to 1,000,000 Years After Present." MOD–01–001. Rev. 01. Reno, Nevada: Desert Research Institute. 2003.

Smith, G.I. and J.L. Bischoff. "An 800,000-Year Paleoclimatic Record from Core OL-92, Owens Lake, Southeast California." Special Paper No. 317. Boulder, Colorado: The Geological Society of America. 1997.

Spaulding, W.G. "Vegetation and Climates of the Last 45,000 Years in the Vicinity of the Nevada Test Site, South-Central Nevada." Professional Paper No. 1329. Washington, DC: U.S. Geological Survey. 1985.

Stothoff, S.A. "Infiltration Abstractions for Shallow Soil Over Fractured Bedrock in a Semiarid Climate." San Antonio, Texas: CNWRA. 1999.

———. NUREG/CR–6333. "BREATH Version 1.1—Coupled Flow and Energy Transport in Porous Media: Simulator Description and User Guide." Washington, DC: NRC. July 1995.

Stothoff, S. and M. Musgrove. "Literature Review and Analysis: Climate and Infiltration." CNWRA No. 07-002. San Antonio, Texas: CNWRA. 2006.

Strickland, L.E., R.S. Thompson, and K.H. Anderson. "North American Packrat Midden Database Dictionary." U.S. Geological Survey Open-File Report 01-022. 2001.

Thompson, R.S., K.H. Anderson, and P.J. Bartlein. "Quantitative Paleoclimatic Reconstructions From Late Pleistocene Plant Macrofossils of the Yucca Mountain Region." U.S. Geological Survey Open-File Report No. 89-338. 1999a.

———. "Atlas of Relations Between Climatic Parameters and Distributions of Important Trees and Shrubs in North America." Professional Paper No. 1650–A. Denver, Colorado: U.S. Geological Survey. 1999b.

Walter, G. "Analysis of Factors Contributing to Uncertainty in Estimating Future Climates at Yucca Mountain." San Antonio, Texas: CNWRA. 2005.

Winograd, I. "Radioactive Waste Disposal in Thick Unsaturated Zones." *Science*. Vol. 212, No. 4502. pp. 457–1464. 1981.

Winograd, I.J., A.C. Riggs, and T.B. Coplen. "The Relative Contributions of Summer and Cool-season Precipitation to Groundwater Recharge, Spring Mountains, Nevada, USA." *Hydrogeologic Journal*. Vol. 6 No. 1. pp. 77–93. 1998.

Winograd, I.J., T.B. Coplen, J.M. Landwehr, A.C. Riggs, K.R. Ludwig, B.J. Szabo, P.T. Kolesar, and K.M. Revesz. "Continuous 500,000-Year Climate Record from Vein Calcite in Devils Hole, Nevada." *Science*. Vol. 258, No. 5080. pp. 255–260. 1992.

Woolfenden, W.B. "A 180,000-Year Pollen Record from Owens Lake, California: Terrestrial Vegetation Change on Orbital Scales." *Quaternary Research*. Vol. 59. pp. 430–444. 2003.

Zhu, C., J.R. Winterle, and E.I. Love. "Late Pleistocene and Holocene Groundwater Recharge from the Chloride Mass Balance Method and Chlorine-36 Data." *Water Resources Research*. Vol. 39, No. 7. SBH 4–1–4–15. 2003.

APPENDIX A

GENERATION OF POSSIBLE FUTURE CLIMATES

A.1 Introduction

This appendix describes the method used to generate possible future climate sequences that could occur at a potential high-level waste repository at Yucca Mountain, Nevada, over the next 1 million years. This appendix also presents an analysis of the range of possible climatic conditions that could occur based on simulated future climate states. The purpose of the analysis was to develop a set of possible future climate sequences that could be used to evaluate the range and uncertainty in net infiltration and deep percolation of meteoric water to the repository horizon based on mean annual precipitation (MAP)[1] and mean annual temperature (MAT).[2] The analysis was not an attempt to predict the future climate at Yucca Mountain or to exactly reproduce past climates at Yucca Mountain; rather, it was performed to provide a transparent and objective methodology for generating infiltration scenarios that can be used in performance assessment.

A.2 Approaches for Generating Possible Future Climates

Various approaches exist that could be used to generate future climate sequences at Yucca Mountain. Future climates, globally and at Yucca Mountain, will be determined by a complex response of Earth-based events and processes to external forcing factors (NRC, 1997).

Over the period of geologic stability at Yucca Mountain, which is approximately 1 million years (National Research Council, 1999), the Earth-based processes involving interactions between the ocean, polar ice caps, and atmosphere will probably be similar to those that affected climates during the past 500,000 to 1 million years. Although the nature of these processes is generally understood, their interaction is complex, making prediction of future climate uncertain. Climate is also affected by large volcanic eruptions, with timing and magnitudes that are poorly predictable. Future climate may also be affected by releases of anthropogenic greenhouse gases.

The primary external forcing factor affecting Earth's climate is generally believed to be the "Milankovich Cycle" (e.g., Elkibbi and Rial, 2001; Paillard, 2001); that is, variations in the amount of solar radiation reaching the Earth (insolation) due to variations in (i) the elongation of Earth's orbit around the Sun (orbital eccentricity), (ii) the change in orientation of Earth's axis of rotation (precession), and (iii) the tilt of Earth's axis away from the orbital plane (obliquity). These orbital features are illustrated in Figure A–1. Unlike Earth-based climatological factors, past and future variations in insolation due to Earth-orbital parameters can be computed with a relatively high degree of accuracy (e.g., Berger, 1978; Berger and Loutre, 1991). Although external events, such as meteor or comet impacts, and variations in solar radiation due to relatively short-term fluctuations in solar activity (e.g., Bertrand, et al., 2002) may affect climate,

---

[1]Mean annual precipitation is referenced frequently throughout this appendix. The acronym MAP will be used.

[2]Mean annual temperature is referenced frequently throughout this appendix. The acronym MAT will be used.

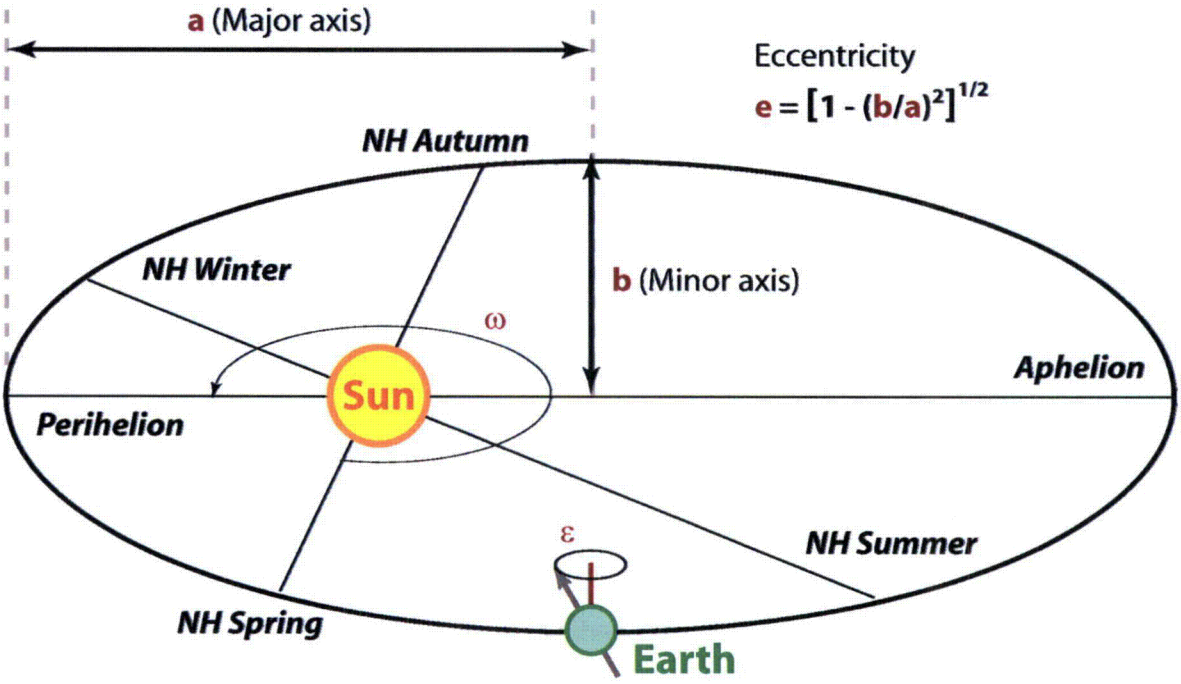

Figure A–1. Illustration of Earth's Orbital Parameters That Determine Insolation. Eccentricity of Earth's Orbit Around the Sun is Represented by *e*. Precession, the Time of the Year When the Earth is at the Perihelion is Represented by ω. Obliquity of the Earth's Axis of Rotation is Represented by ε.

the former events are unpredictable in the long term and the latter occur on a time scale (years to decades) that is orders of magnitude shorter than that of interest for Yucca Mountain.

Techniques that could be used to generate possible future climates range from numerical climate models that simulate ocean, land, and atmospheric processes (e.g., Berger and Loutre, 1991; Intergovernmental Panel on Climate Change, 2001) to empirical correlations between past climates and Earth's orbital cycles (e.g., Sharpe, 2003; Bechtel SAIC Company, LLC, 2004). All of these approaches can be described as climate models with various dimensionality, regional applicability, and extent to which they are based on mathematical representations of physical and chemical processes controlling climate.

Complex numerical models have the advantage that they can, in principle, predict future climates in local regions of the Earth that are based on objective, mathematical models. However, such models require substantial computational resources, are difficult to apply and calibrate for extended time periods, and are still subject to uncertainty because of limitations in scientific understanding of the processes controlling climate change and uncertainty in the parameter values used in the modeling (e.g., Shackley, et al., 1998).

Simpler empirical models and zero-dimensional models have been successfully calibrated (tuned) to reproduce variations in paleoclimate indicators, such as the marine oxygen isotope record or the oxygen isotope record from Devils Hole, Nevada (e.g., Sharpe, 2003; Shaffer, et al., 1996; Paillard, 1998; Ghil and Le Treut, 1981), and are much easier to use to generate long-term future climates. Because these models do not directly simulate climate conditions, such as precipitation and temperature, the climatic conditions must be inferred from correlations to paleoclimate indicators. For example, the marine oxygen isotope record as represented in the Spectral Mapping Project (SPECMAP)[3] reconstruction (Imbrie, et al., 1984)] is generally regarded as an indicator of global ice volume, but does not directly represent precipitation or temperature. The Devils Hole oxygen isotope record is an indicator of the temperature of precipitation recharging its contributing aquifer and does not yield a direct estimate of annual precipitation.

The validity of using these simple models depends, of course, on the validity of applying past climate correlations to the future. To the extent that the features, events, and processes that determined past climates during the later half of the Pleistocene continue to operate over the next 1 million years, the semiempirical models provide a reasonable basis for generating possible future climate sequences, although they are not likely to accurately predict the duration and intensity of future climates because of the inexact nature of the historical correlations.

The effect of greenhouse gases on global temperatures is a factor that could invalidate projections from the semiempirical models. A significant amount of research related to the potential effects of greenhouse gases (primarily carbon dioxide and methane) on global climate has been conducted over the past two decades. Much of this work has focused on estimating the climatological responses for the next two centuries that may result from the dramatic increase in atmospheric carbon dioxide produced over the past approximately 150 years as a result of industrialization and burning fossil fuels. A significant body of research has been developed that suggests greenhouse gas emissions will have some effect on the global climate, during at least the next few centuries (e.g., Intergovernmental Panel on Climate Change, 2001; National Academy of Sciences, 2002). The specific nature of these changes and their duration remains a subject of continuing research. NRC (1997) concluded that the influence of anthropogenic greenhouse gas emissions would dissipate over the next 3,000 to 5,000 years, resulting in a return to more natural climate variations. Recent work by Archer (2005) indicates that 25 percent of the anthropogenic carbon dioxide will remain in the atmosphere for thousands of years and 7 percent will remain for 100,000 years. Archer and Ganopolski (2005) estimated a much longer period of anthropogenic influence, potentially lasting hundreds of thousands of years, depending on the mass of fossil carbon ultimately emitted.

The semiempirical climate modeling approach was selected to generate future climate sequences for performance assessment because this approach has been demonstrated to be capable of reproducing broad features of global climate over periods of hundreds of thousands of years, is relatively simple to implement so that multiple realizations can be easily generated, and is transparent in terms of operating algorithms. Three such models were considered for this purpose: the (i) discrete and (ii) continuous models of Paillard (1998) and (iii) the cryodynamic model of Ghil and Le Treut (1981).

---

[3]The Spectral Mapping Project established a correlation between oxygen isotopes in Marine Sediments and Earth's orbital variations. The commonly uised SPECMAP acronym is referenced frequently throughout this report. The abbreviation SPECMAP will be used.

The Paillard models are rule-based zero-dimensional models wherein the transition between climate states is driven by the insolation record (either past or future) and a set of rules related to climate transitions and climate durations. As will be discussed in more detail in Section A.3, the discrete Paillard model has many similarities to the climate model of Sharpe (2003), but is more transparent and objective in terms of the rules employed (see Walter, 2005).

The Ghil and Le Treut (1981) model is also zero dimensional but more complex, consisting of three coupled, nonlinear differential equations that describe the global energy balance, ice sheet volume balance, and isostatic movement of the northern continental crust. Insolation is the external forcing factor. The coupled and nonlinear nature of the governing equations in the Ghil and Le Treut (1981) model cause the model to behave as a chaotic dynamic system, with stable and unstable states that depend on the choice of key parameters. Although the Ghil and Le Treut (1981) model has the advantage of being "physics-based" in the sense that the model is based on the physical principles of conservation of mass and energy, many of the parametric relationships in the model are still empirical. Ghil (1994) demonstrated that the Ghil and Le Treut (1981) model could reproduce some of the statistical aspects of paleoclimate reconstructions by a suitable choice of parameters, particularly higher frequency oscillations, but made no attempt to calibrate these parameters to the paleoclimate record. Previous analyses of the modeling approach by Ghil and Le Treut (1981) and Le Treut and Ghil (1983) demonstrated the potentially chaotic behavior of the model over certain parameter ranges.

The Ghil and Le Treut model was not selected for generating possible future climate sequences at this time because the model has not been calibrated to paleoclimate indicators and because of its sensitivity to parameter selection. Instead, the continuous version of the Paillard model was chosen because of its greater stability and simplicity of use. If features such as high frequency climate oscillations or the influence of greenhouse gases are to be investigated in the future, the more physically based Ghil and Le Treut (1981) model might be a suitable choice to replace the Paillard model. Other models of intermediate complexity, such as the Louvain-la Neuve (LLN) model (Berger, et al., 2003) may also be practical for generating very long-term future climate sequences (Walter, 2005).

A.3 Future Climate Models

Paillard's discrete and continuous models are based on the concept that changes in climate states occur when insolation in the northern hemisphere passes through certain threshold values, as illustrated in Figure A–2. Paillard uses ice sheet volume as a climate surrogate and represents the global climate as being in one of three characteristic states: interglacial (i), mild glacial (g), and full glacial (G). Although his continuous model yields a continuous record of ice sheet volume, the rate of ice sheet change is still controlled by parameters related to each specific climate state. The basic concepts and rules underlying the Paillard model are first illustrated for the discrete model and are then generalized to the continuous model.

A.3.1 Paillard Models

The Paillard models use a normalized value of northern hemisphere insolation as the forcing factor for climate change. The normalized value is computed from the actual summer insolation at the top of the atmosphere at 65° N using the following formula

$$I^* = \frac{I_a - I_m}{\sigma} \qquad \text{(A–1)}$$

where

I^*	—	normalized insolation with zero mean and unit standard deviation
I_a	—	actual insolation
I_m	—	mean of the insolation record
σ	—	standard deviation of the insolation record

Based on the definition in Eq. (A–1), the normalized insolation depends on the part of the insolation record that is chosen for analysis.

The Paillard models cycle between climate states, as illustrated in Figure A–2. Climate stays in the interglacial climate state until normalized insolation decreases to a threshold value of I_0, triggering a transition to the mild glacial state. Climate stays in the mild glacial state until ice sheet volume increases to a threshold value (V_{max}), triggering a transition to the full glacial state. Climate returns to the interglacial state when normalized insolation rises to a threshold value of I_1. Transitions from interglacial to full glacial and from full glacial to mild glacial are forbidden.

Several rules moderate the threshold-based transitions between states. In the discrete model, the mild glacial state must occur for a minimum duration of τ_g before a transition to the full glacial climate can occur. In the continuous model, the minimum duration condition is implemented using time constants for the maximum rates of ice sheet volume growth (τ_g) and decay (τ_i). Note that the τ_g parameter has a different meaning in the two Paillard models.

An additional rule, not illustrated in Figure A–2, further moderates the mild glacial to full glacial transition. A transition from the mild glacial to full glacial is prohibited if the preceding maximum in normalized insolation is greater than a threshold value of I_3. If this rule is satisfied, then the mild glacial to full glacial transition occurs as soon as normalized insolation falls below a value of I_2 (assuming all other conditions are satisfied). This rather *ad hoc* rule was apparently introduced to eliminate certain climate transitions that did not appear in the paleoclimate record, but which would have occurred using only the first two rules.

The future and past insolation records used for this study were for the summer solstice at 65° N latitude and were generated using a computer program developed by Roper (2003) based on the insolation model of Berger and Loutre (1991). The results of the Roper program were compared to values of insolation tabulated from National Oceanic and Atmospheric Administration (2006) to verify the Roper program. A comparison between the tabulated values for the past 900,000 years and those computed using Roper's program is shown in Figure A–3. The small differences between the records are not significant for the purpose of this analysis. The values of I_m and σ were computed for the time between 800,000 years before present and present.

The paleoclimate record shown in Figure A–4 was generated with the discrete Paillard model using his parameters, which were calibrated to the SPECMAP marine isotope record. The minor differences between the climate states generated for this study and those reported by Paillard (1998) may be due to small differences in the insolation records or the time periods over which the insolation averages and standard deviations were computed.

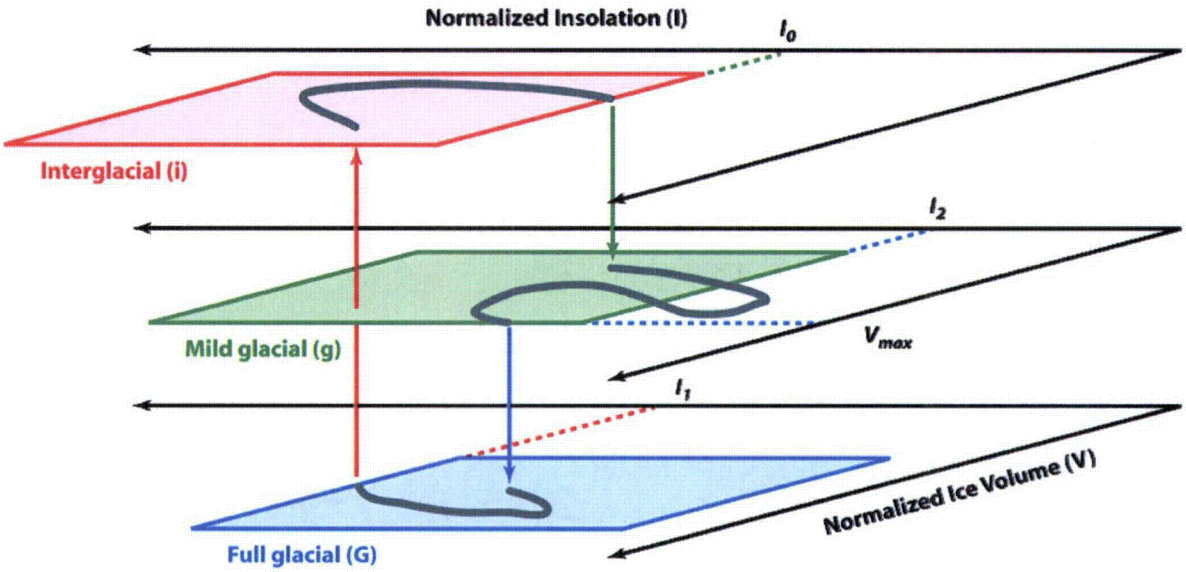

Figure A–2. Illustration of Paillard's Threshold Climate Model (Modified From Paillard, 1998)

The continuous Paillard model computes a continuous record of northern hemisphere relative ice volume with a discrete climate sequence. The change in relative ice volume during each model timestep (1,000 years in this case) is computed by

$$\frac{\Delta V}{\Delta t} = \frac{(V_R - V)}{\tau_R} - \frac{F}{\tau_F} \qquad \text{(A–2)}$$

where

V — is the relative ice volume

t — is time

V_R — is a reference ice volume for the climate state at time t

τ_R — is a time constant for the climate state at time t

F — is an insolation forcing function

τ_F — is a time constant for insolation

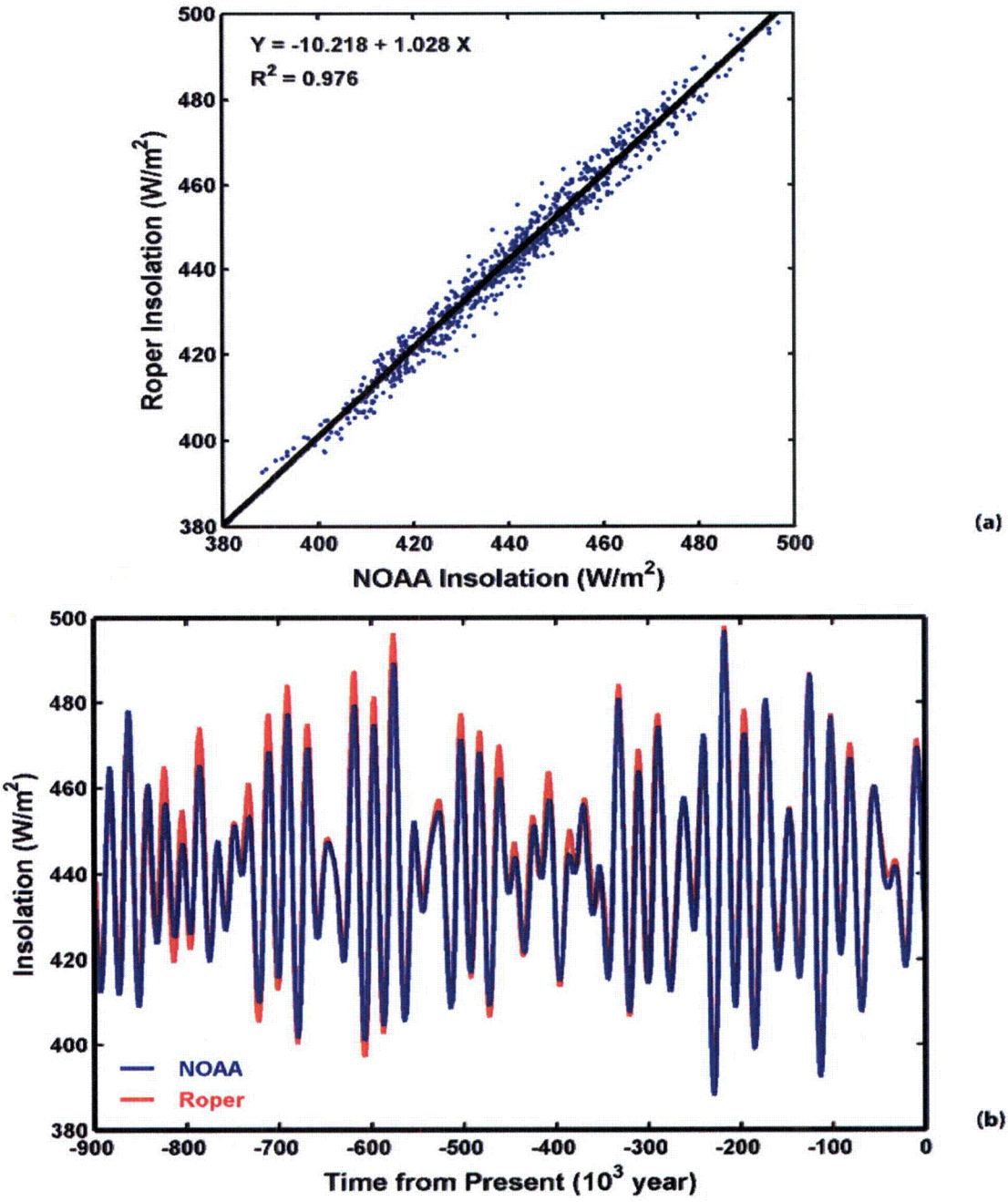

Figure A–3. Comparison Between Insolation Computed Using the Program Developed By Roper (2003) (Labeled "Roper") and Tabulated Values From National Oceanic and Atmospheric Administration (2006) (Labeled "NOAA").
(a) Comparison of Millennial Averages and (b) Time Sequences.
[1 W/m^2 = 1,197 Cal/ft^2/day]

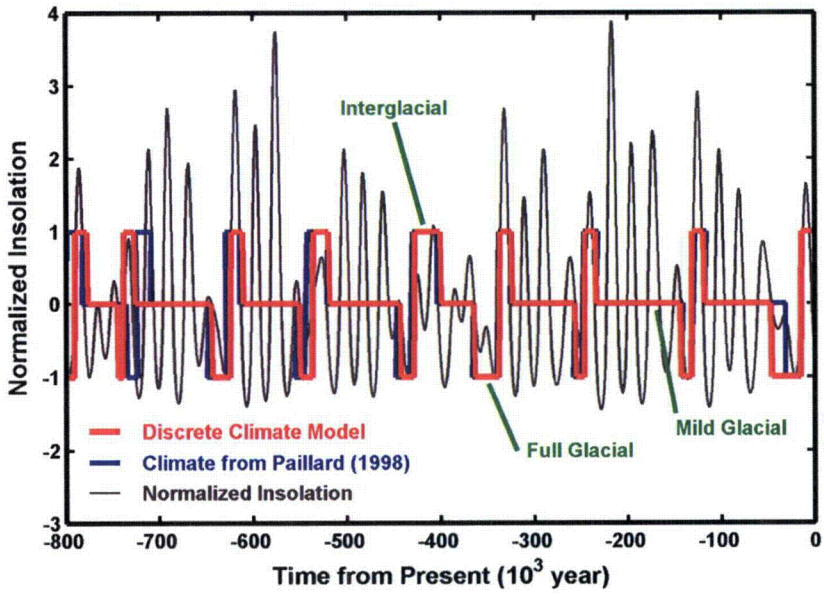

Figure A–4. Comparison of Past Climate Sequence Reported by Paillard (1998, p. 2) With the Sequence Computed From the Paillard Discrete Model Used for This Report and Normalized Insolation Used for This Report.

The forcing function is computed from the normalized insolation by first applying a filter

$$I_F^* = \frac{1}{2\left[I^* - \sqrt{4a^2 + (I^*)^2}\right]} \qquad \text{(A–3)}$$

where

I_F^* — is the smoothed, normalized insolation

a — is a parameter between 0 and 1

The forcing function is then computed as

$$F = \frac{I_F^* - I_m^*}{\sigma^*} \qquad \text{(A–4)}$$

where

I_m^* — is the mean of the filtered insolation

σ^* — is the standard deviation of the filtered insolation

Following Paillard, a value of *a* equal to 1 was used for this report. The effect of the filtering process is to reduce the extremes in negative values in the normalized insolation, as illustrated in Figure A–5. According to Paillard (1998), this empirical adjustment accounts for the lower sensitivity of the ice volume to insolation during cold periods.

The values of V_R and τ_R depend on the climate state at the time of interest (i.e., if the climate is interglacial, the interglacial values of V_R and τ_R are used to calculate the rate of change in relative ice volume). The climate state is determined by the same rules used in the discrete model. Figure A–6 shows a flowchart with the logic used to select the climate state and compute the change in ice volume.

Paillard's rule for causing an immediate change from mild glacial to full glacial states if the ice volume exceeded 1 was not implemented in the computer program used for this report. Contrary to Paillard's finding, this rule was found to (i) cause mild to full glacial transitions not indicated by the SPECMAP record and (ii) delay full glacial to interglacial transitions. The effect was particularly pronounced in the simulation of the past 100,000 years. An improved match to the paleoclimate record was achieved when the sudden transition rule was removed from the program. The reason for this discrepancy between the implementation of Paillard's

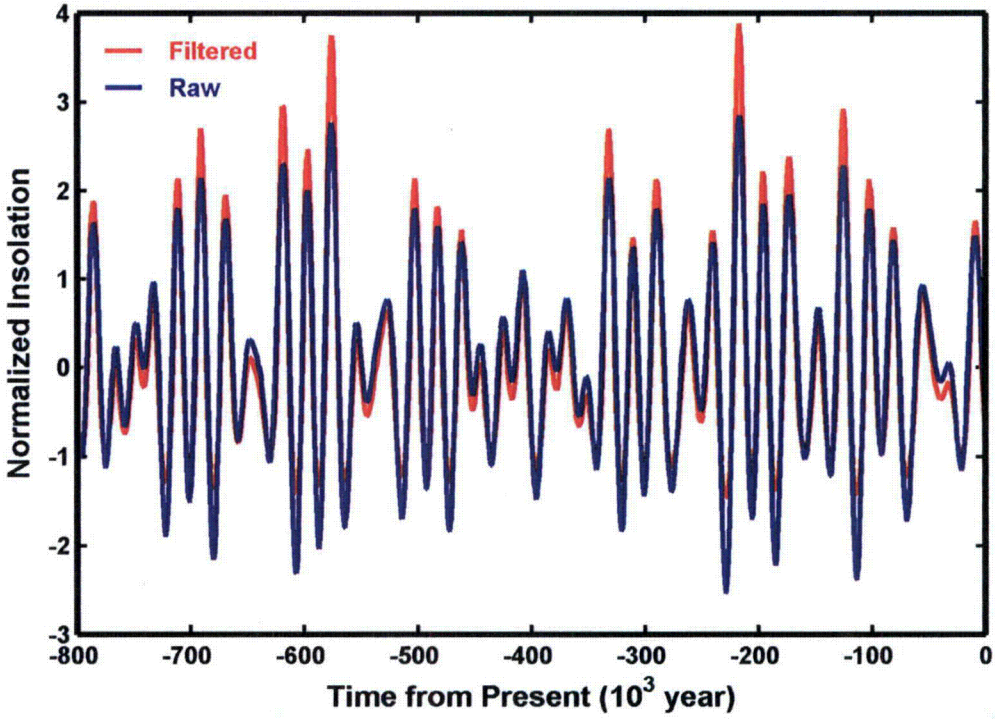

Figure A–5. Comparison of Raw, Relative Insolation With Filtered, Normalized Insolation

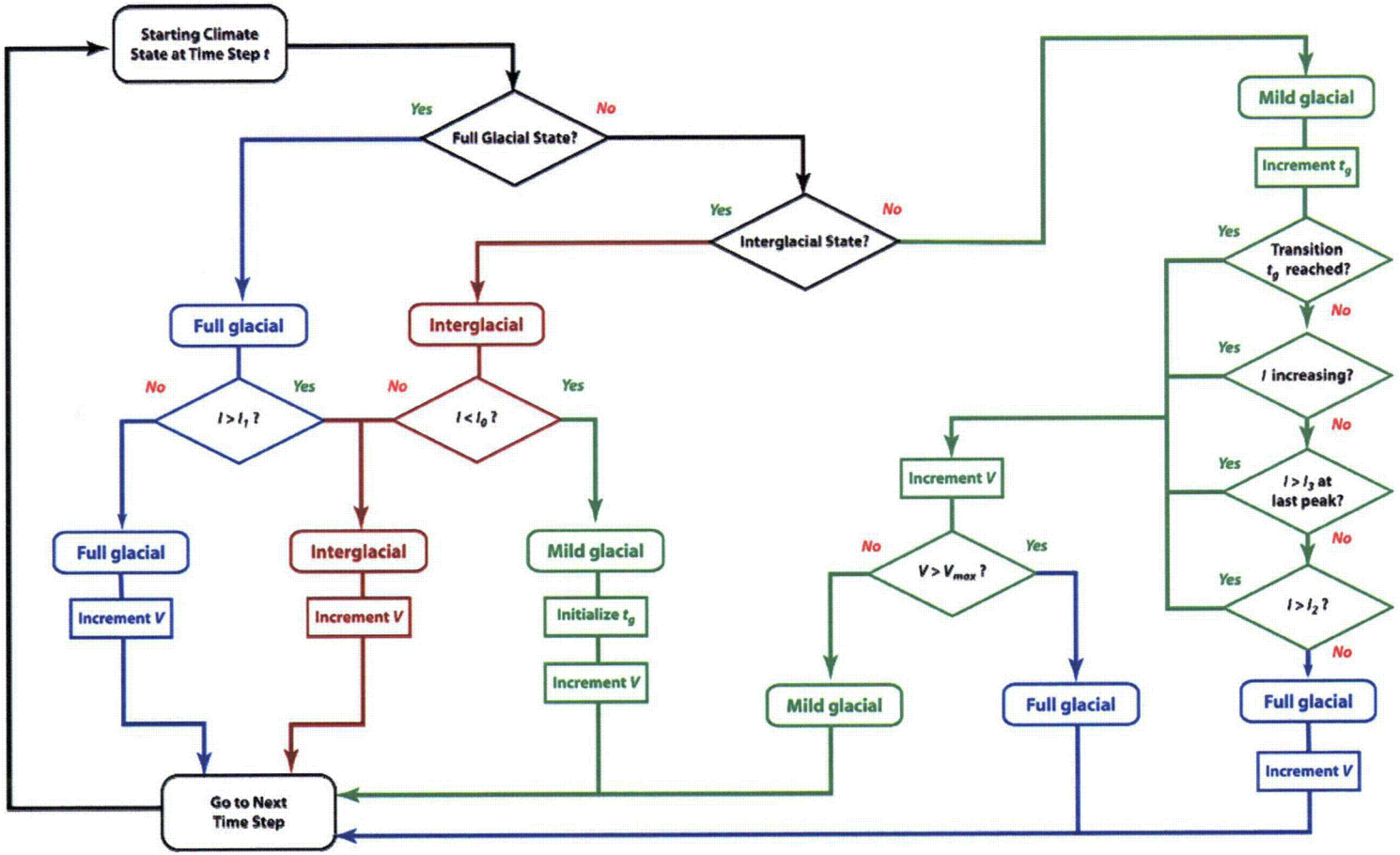

Figure A–6. Flowchart for Calculation of Climate State and Relative Ice Volume Using the Continuous Paillard (1998) Model Algorithm

model for this study and his reported model is not known, but may be due to small differences in the insolation record. Despite this difference in the models, the calibration to the past climate record developed for this study is practically identical to the presented by Paillard.

A.3.2 Comparison of Paillard Model to Past Climate Data

The continuous Paillard model depends on the nine adjustable parameters listed in Table A–1. The nominal values listed in Table A–1 are those Paillard developed to calibrate the past climate states and ice volume to the SPECMAP marine oxygen isotope chronology (Imbrie, et al., 1989). The past climate and relative ice volume simulated by the Paillard model for this report are shown in Figure A–7(a). The correlation between the simulated climate states, relative ice volume, and the SPECMAP record is shown in Figure A–7(b).

Figure A–8 shows a comparison between the SPECMAP record (scaled to the range of 0 to 1, with larger values indicating greater ice volume), the major marine isotope stages (MIS),[4] and the climates generated by the model using Paillard's calibrated (nominal) parameters (Table A–1). The simulated full glacial climate ice volumes agree well with the SPECMAP record, and the timing of the climate transitions also corresponds reasonably well to MIS boundaries.

Figure A–8 also shows a detailed comparison between the simulated ice volume using the Paillard model, scaled from 0 to 1, and the SPECMAP record, also scaled 0 to 1. Here, too, the correspondence between maxima and minima in the simulated ice volume and SPECMAP is good, although the magnitude of the values differs. Fifty of the 53 maxima and minima in the SPECMAP record are reproduced in the simulated ice volume record. In further support of Paillard's calibration parameters, Archer and Ganopolski (2005) reported that the critical value of insolation needed to trigger the onset of glacial conditions in a multidimensional, physics-based climate model was close to the nominal value of I_0 in Paillard's model.

A.3.3 Future Climate Simulations Using the Continuous Paillard Model

Possible future climates were generated using the continuous Paillard model by varying the parameters I_0 and I_3. Past and future climate sequences were generated for I_0 values of -0.5, -0.75 (nominal value), -0.8, and -0.9, all with I_3 set to a nominal value of 1. Decreasing the value of I_0 has the effect of prolonging interglacial periods at the expense of mild and full glacial periods and increasing it promotes transitions to mild and full glacial states. An additional climate sequence was generated with I_3 equal to 0.75 and the nominal value of I_0. Decreasing the value of I_3 prolongs mild glacial periods at the expense of full glacial periods. The time-parameter values were not changed because Paillard (1998) had found that his model was not very sensitive to those parameters.

The resulting past and future climate sequences are shown in Figure A–9 in terms of relative ice volume and climate state. As illustrated by Figure A–9, changing the I_0 and I_3 parameters from their nominal value has very little effect on the computed past ice volume and climate states. Future climates differ more as the parameters are varied, although the differences are not dramatic. The most significant difference in future climates was a prolongation of mild glacial

[4]Marine Isotope Stage is referenced frequently throughout this report. The abbreviation MIS will be used.

Table A–1. Adjustable Parameters in the Continuous Paillard Model and Their Nominal Values		
Parameter	**Description**	**Nominal Value**
I_0	Insolation value triggering transition from interglacial to mild glacial climate	-0.75
I_1	Insolation value triggering change from full glacial to interglacial climate	0
I_2	Insolation value that allows transition from mild glacial to full glacial climate	0
I_3	Insolation value that if exceeded, prevents transition from mild glacial to full glacial climate	1
τ_i	Time constant for interglacial climate state	10,000 years
τ_g	Time constant for mild glacial climate state	50,000 years
τ_G	Time constant for full glacial climate state	50,000 years
τ_F	Time constant for insolation forcing function	25,000 years

conditions during the next 100,000 years with I_0 equal to -0.9 and a reduction in the ice volume during the period from 175,000 years to 225,000 years after present with I_3 equal to 0.75. In general, the greatest sensitivity of climate and ice volume to the insolation parameters is during the next 300,000 years with less sensitivity thereafter. It is unclear why this particular period should be most sensitive to the insolation parameters but it may be related to the relatively low amplitude of insolation variations during the next 100,000 years being followed by a period of greater variation, as illustrated in Figure A–10. Paillard (2001) also noted a similar lack of sensitivity for the past climate record and increased sensitivity for the future climates.

A.4 Translation of Climate State and Ice Volume to MAP and MAT

The ultimate purpose of this analysis is to generate future sequences of MAP and MAT as functions of climate that can be used to evaluate the range and uncertainty in net infiltration and deep percolation of meteoric water through the repository horizon. Sharpe (2003) and Bechtel SAIC Company, LLC (2004) referenced discrete values of MAP and MAT to discrete climate states based on interpretations of the paleoclimate from lacustrine ostracode assemblages in the western United States and present-day analog site precipitation and temperature records. The approach taken here considers the work of Sharpe (2003), but references MAP and MAT to ice volume rather than solely to climate state. There are two reasons for this approach.

First, climate in the western United States is believed to be primarily controlled by the north-south position of zonal atmospheric circulation patterns (e.g., Forester, et al., 1999), which are strongly affected by the extent of the northern ice cap. These major zonal circulation patterns are illustrated in Figure A–11. When the northern ice sheet expands during cold,

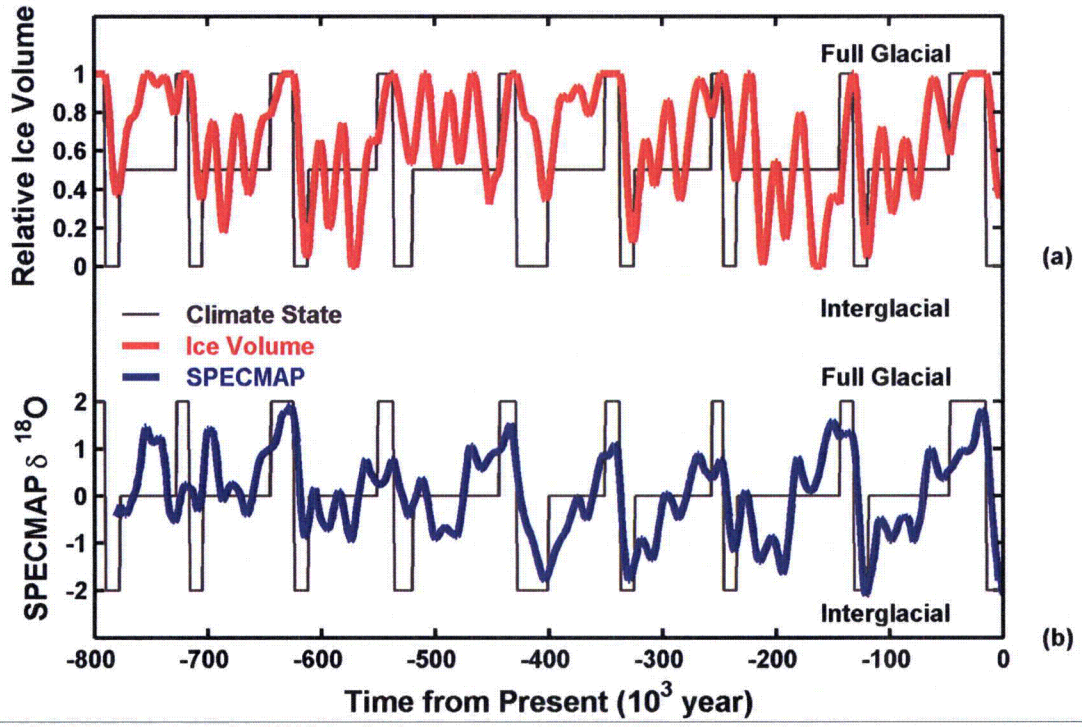

Figure A–7. (a) Simulated Climate and Ice Volume Using the Continuous Paillard Model and (b) Comparison of Simulated Climate States with SPECMAP $\delta^{18}O$ Record

glacial climates, the southern edge of the polar cell pushes south, increasing precipitation and lowering temperature in southern Nevada. During extreme increases in the size of the ice sheet, the polar cell could move far enough south to produce colder and drier conditions compared to less-extreme glacial conditions. During warm climates with smaller northern ice sheets, the circulation cells move north, resulting in relatively hot, dry conditions during interglacial periods. Small ice sheets could even allow (i) more frequent intrusion of the southwestern summer monsoon into southern Nevada, and (ii) increased winter precipitation because of prolonged El Nino conditions (e.g., Philander and Federov, 2003).

Second, indicators of global ice volume, such as the SPECMAP marine oxygen isotope record summarized in Section A.3, indicate that ice volume and, by implication, global climate, has fluctuated significantly during generalized climate states and lags behind climate state transitions, although a one-to-one correlation between the SPECMAP record and ice volume may not exist (e.g., Berger and Loutre, 1991). Thus, assigning single values of MAP and MAT to general climate states lasting tens of thousands of years may not represent either average conditions or variability in MAP and MAT during these periods.

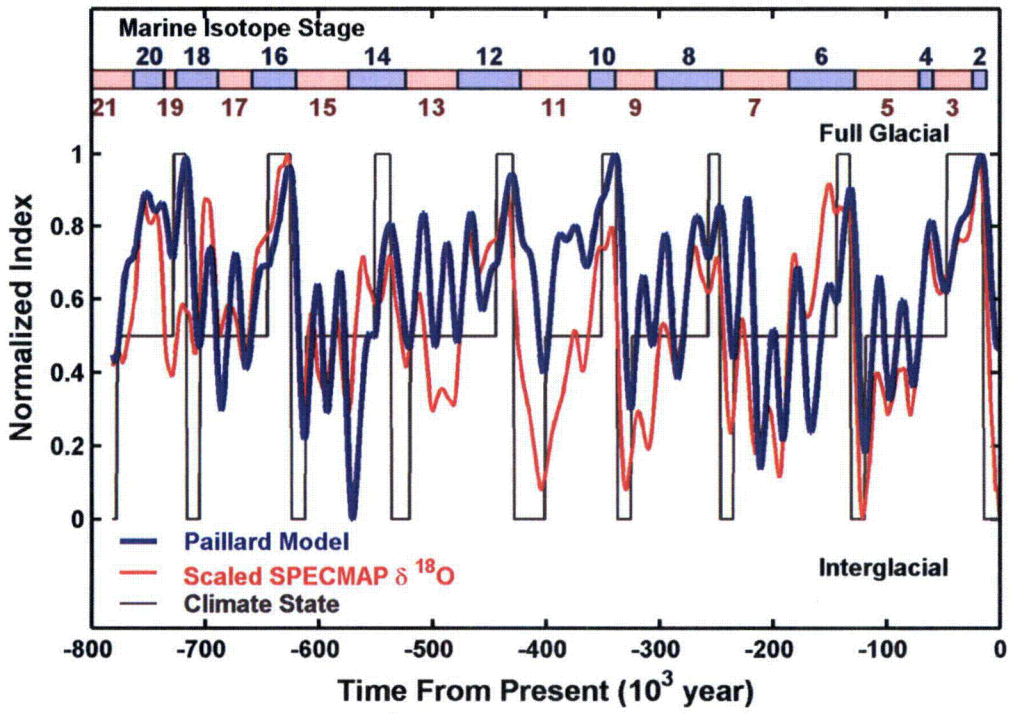

Figure A–8. Comparison of Simulated Climate States and Simulated Normalized Ice Volume to Scaled SPECMAP $\delta^{18}O$ and Marine Isotope Stages

Unfortunately, establishing a functional relationship between ice volume and the major climate parameters of MAP and MAT at Yucca Mountain is not straightforward. Shaffer, et al. (1996) have argued that variations in temperature and precipitation in southern Nevada reflected in the Devils Hole oxygen isotope record are better correlated to winter insolation in the subtropics and summer insolation at the latitude of Devils Hole than to arctic insolation. Based on their thesis, the ice volume record simulated by the Paillard model, which is driven by insolation at 65°N latitude and tuned to SPECMAP, would not necessarily be a good indicator of climate at Yucca Mountain. Figure A–12, however, illustrates that the SPECMAP record, the Devils Hole record, and the simulated normalized ice volume agree relatively well in terms of the number and duration of climate transitions, although the timing of some of the peaks disagree. Based on this general agreement between the isotopic records and the simulated ice volume, the ice volume computed by the Paillard model forced by arctic insolation provides a reasonable basis for generating possible future climate sequences and relative climate characteristics.

A simple functional relationship between climate state, ice volume, and estimates of MAP and MAT is developed in Section 2 of the main body of this report. The simple relationship is used to estimate long-term-average net infiltration at Yucca Mountain and is not discussed in this appendix. A slightly more complex functional relationship was developed to relate climate

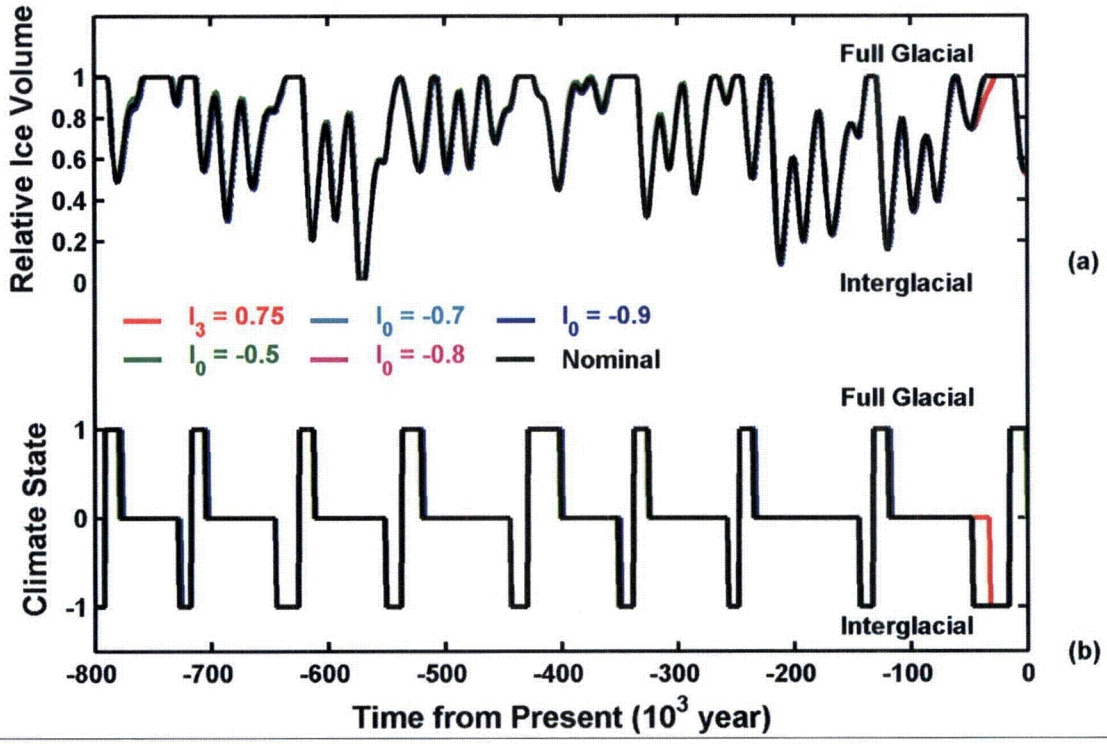

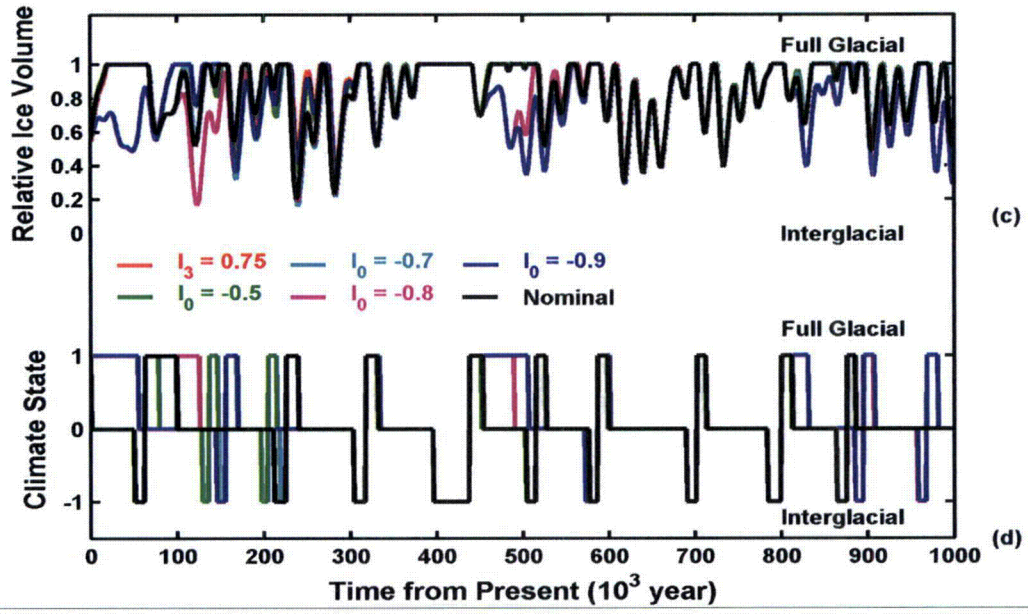

Figure A–9. Comparison of Past Ice Volumes and Climate Sequences Generated With Various Choices of Insolation Threshold Parameters: (a) Past Ice Volume, (b) Past Climate, (c) Future Ice Volume, and (d) Future Climate

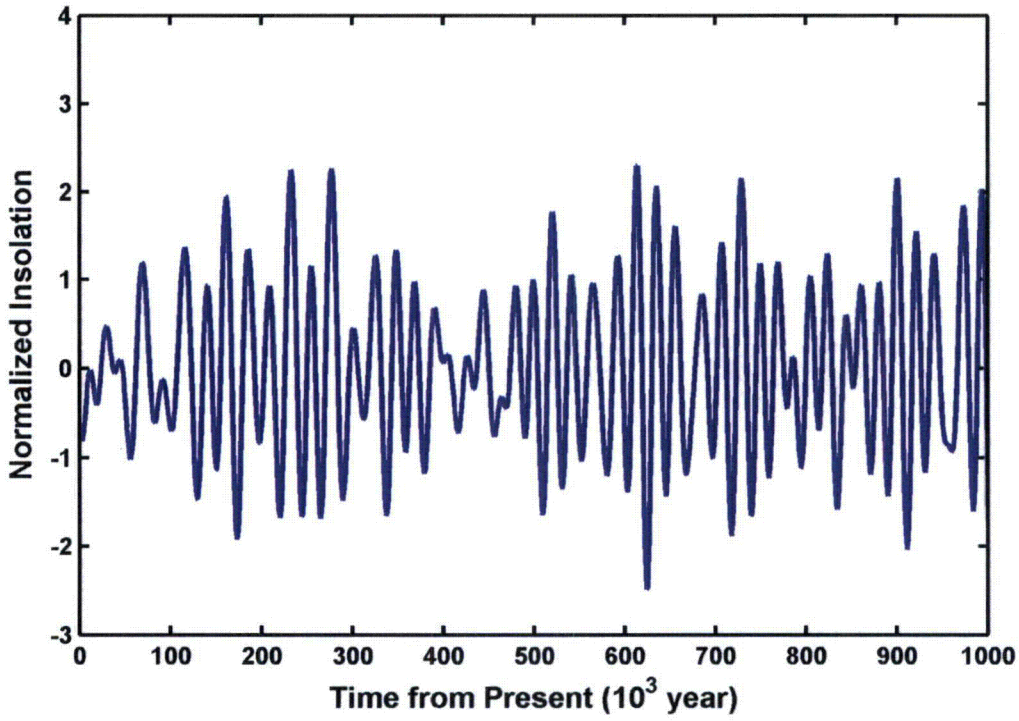

Figure A–10. Normalized Insolation (Summer Solstices, 65° N) for the Next 1 Million Years

states identified by Sharpe (2003) from lacustrine ostracode assemblages to the ice volumes simulated by the Paillard model. This second relationship allows an independent assessment of the Sharpe model while exploring the variability between different ice volume sequences.

Sharpe (2003) identified three major climate states (glacial, intermediate, and interglacial), further subdivided the glacial climate into three separate types based on estimated temperature and precipitation, and included a monsoon climate in the intermediate state. The intermediate state was described as transitional between the interglacial and glacial states. Figure A–12 shows a correlation between the climate states identified by Sharpe, the scaled Devils Hole isotope record, and the climate states and normalized ice volumes generated by the Paillard model. Although the correspondence between the climate states identified by Sharpe, the simulated climate sequence, and the Devils Hole record is not perfect, Sharpe's three major climate states generally fall into the following normalized ice volume ranges generated by the Paillard model:

- Interglacial — Ice volume less than 0.4
- Intermediate — Ice volume between 0.4 and 0.8
- Glacial — Ice volume greater than 0.8

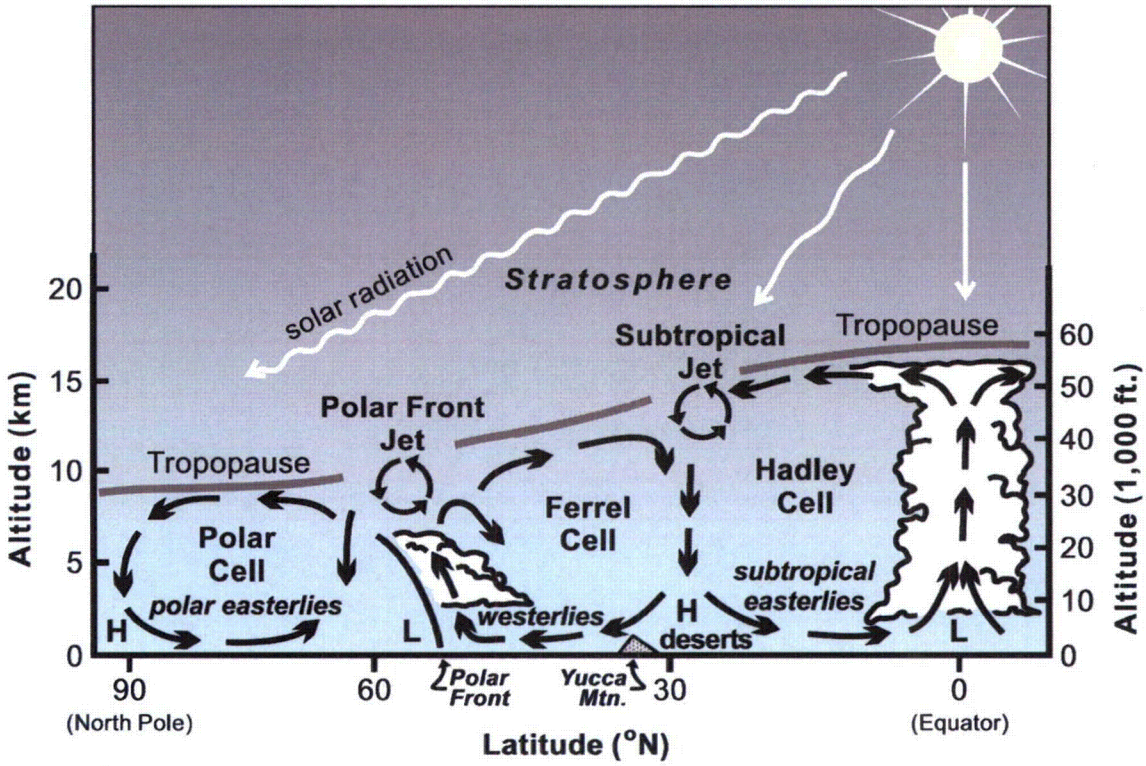

Figure A–11. Illustration of Atmospheric Circulation Patterns in the Western United States (From Bechtel SAIC Company, LLC, 2004, Figure 6-2)

Sharpe associated the interglacial climate with present-day climate conditions. Because the global ice volume has been less in the past than at present (e.g., Broecker, et al., 1968), present-day climate conditions may not be representative of future climates with smaller ice sheets. Thus, MAP and MAT for smaller ice sheets (lower normalized ice volume) may differ from present-day values. The intermediate climate of Sharpe is assumed to include transitions from interglacial to full glacial conditions and the mild glacial state of Paillard's model.

Sharpe (2003) subdivided the glacial climates into a relatively warm, wet glacial climate associated with MIS 8 and MIS 10; a cold, wet climate associated with MIS 6; and a cool, relatively dry climate associated with MIS 2 and MIS 4. Although Sharpe's interpretation may be reasonable, correlations between these climate characteristics and the SPECMAP and Devils Hole isotopic records are not obvious (Figure A–12). Because very large ice sheets would deflect cold air masses southward, it seems reasonable to associate the cold, wet glacial climate with the largest ice volume and the cool, wet glacial climate with ice volumes between the upper range of the intermediate ice volume range and the maximum ice volume. Sharpe inferred the cool, dry glacial climate from relative lake elevations in the Great Basin. Although such a glacial climate is possible, it is difficult to correlate with ice volume or the SPECMAP and Devils Hole isotopic records, so the cool, dry glacial climate is not included in future climate scenarios based on insolation or ice volume.

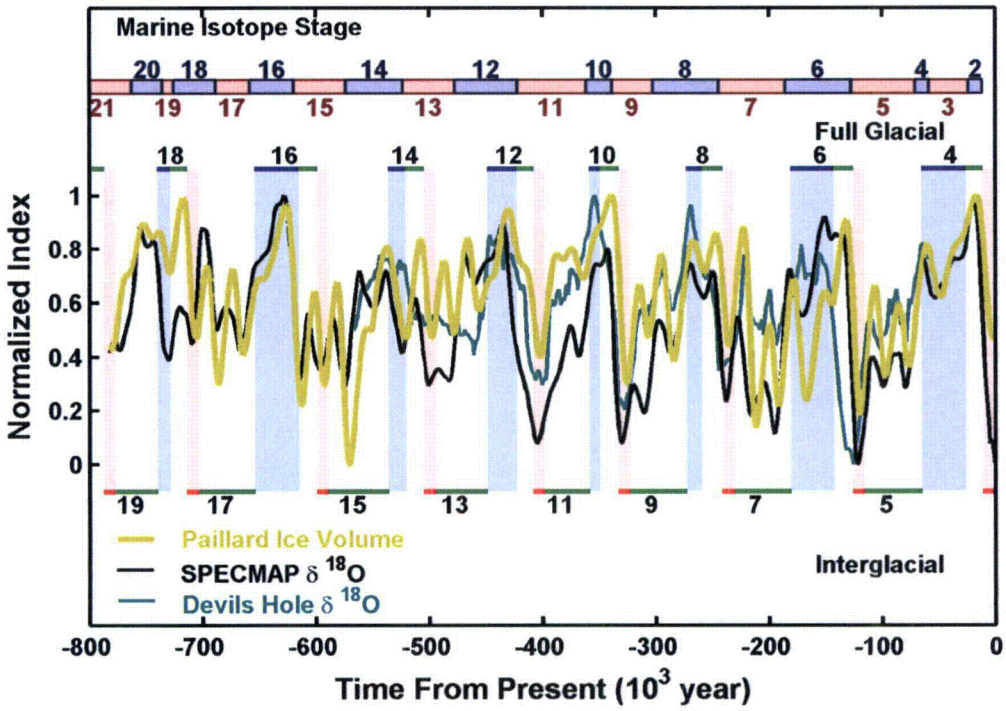

Figure A–12. Sequences of Scaled SPECMAP $\delta^{18}O$, Devils Hole $\delta^{18}O$, and Scaled Ice Volume Generated by the Continuous Paillard Model. Climate States Identified by Sharpe (2003) Are Shown as Blue Bands for Full Glacial Intervals and Pink Bands for Interglacial Intervals.

Based on these considerations, the following rules were developed to generate future sequences of MAP and MAT related to climate state and ice volume:

Ice Volume Less Than Upper Interglacial Level

$$P(t) = P_{min} + \frac{(P_i - P_{min})}{(V_i - V_{min})}[V(t) - V_{min}] \quad \text{(A–5)}$$

$$T(t) = T_{min} + \frac{(T_i - T_{min})}{(V_i - V_{min})}[V(t) - V_{min}] \quad \text{(A–6)}$$

where

$P(t)$ — is MAP at time t

P_i — is MAP at the upper interglacial level

P_{min} — is MAP at the minimum ice volume

$V(t)$ — is ice volume at time t

V_i — is the ice volume at the upper interglacial level

V_{min} — is the minimum ice volume (zero)

$T(t)$ — is MAT at time t

T_i — is MAT at the upper interglacial level

T_{min} — is MAT at the minimum ice volume

Ice Volume Between Upper Interglacial Level and Lower Full Glacial Level

$$P(t) = P_i + \frac{(P_g - P_i)}{(V_g - V_i)}[V(t) - V_i] \tag{A–7}$$

$$T(t) = T_i + \frac{(T_g - T_i)}{(V_g - V_i)}[V(t) - V_i] \tag{A–8}$$

where

P_g — is MAP at the lower glacial level

V_g — is the ice volume at the lower glacial level

T_g — is MAT at the lower glacial level

Ice Volume Greater Than Lower Full Glacial Level

$$P(t) = P_g + \frac{(P_{max} - P_g)}{(V_{max} - V_g)}[V(t) - V_g] \tag{A–9}$$

$$T(t) = T_g + \frac{(T_{max} - T_g)}{(V_{max} - V_g)}[V(t) - V_g] \tag{A–10}$$

where

P_{max} — is MAP at the maximum glacial level

V_{max} — is the ice volume at the maximum glacial level (1)

T_{max} — is MAT at the maximum glacial level

Eqs. (A–5) through (A–10) allow for a linear variation of MAP and MAT within each climate state and are general enough to allow the effects of uncertainty in the values of MAP and MAT for the end members of the climate states to be considered in generating possible future sequences of MAP and MAT.

Figure A–13 shows examples of the distribution of MAP and MAT versus normalized ice volume computed using Eqs. (A–5) through (A–10) and the upper and lower bound values of MAP and MAT estimated by Sharpe (2003) from analog climate site meteorological data. The use of Sharpe's analog site data is for illustrative purposes only and does not imply concurrence with those estimates of future climate MAP and MAT. The climate state ice volume boundaries and end member values of MAP and MAT used to generate Figure A–13 are listed in Table A–2. Present-day MAP at Yucca Mountain was assumed to be 190 mm/yr [7.5 in/yr] based on the analysis presented in Section 2 of the main body of this report. The minimum value of MAP reported by Sharpe (2003), 125 mm/yr [4.9 in/yr], was assumed to be the lowest value at Yucca Mountain at a normalized ice volume of zero.

Figure A–14(a) shows the cumulative frequency distribution of MAP based on Sharpe's upper bound analog sites for the past 800,000 years using the nominal insolation parameters in the Paillard model (Table A–1), the frequency distributions for the future 1 million years using the nominal Paillard model parameters, and values of I_0 (the insolation triggering the interglacial to mild glacial transition in the Paillard model) of –0.5 and –0.9. For the nominal value of I_0, there is little difference between the distributions for the past and the future. Making the value of I_0 less negative results in more frequent transitions from interglacial to mild glacial conditions and greater opportunity for a transition from mild glacial to full glacial. The more negative value has the opposite effect. The less negative I_0 value yields slightly wetter future climates and the

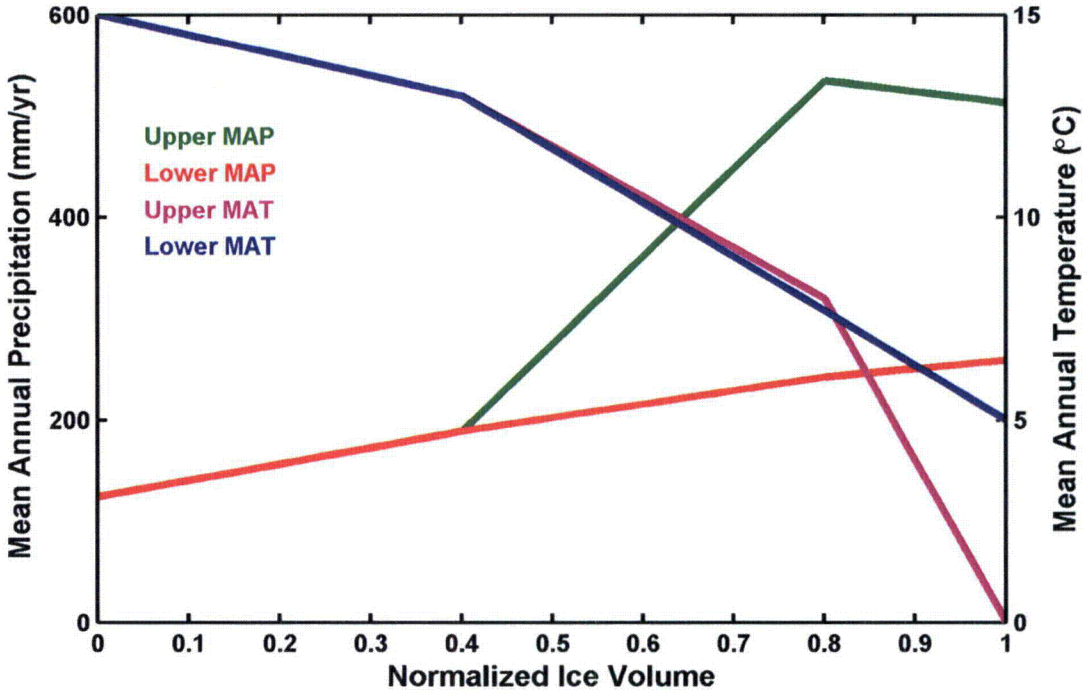

Figure A–13. Examples of Distributions of MAP and MAT Versus Normalized Ice Volume Computed From Eqs. (A–5) through (A–10) Using Upper and Lower Bound Analog Site Values From Sharpe (2003) With Present-Day MAP Set to 190 mm/yr [100 mm/yr = 3.94 in/yr]

Table A–2. Climate State End Member Values of Normalized Ice Volume, MAP,* and MAT† Used to Generate Examples of MAP and MAT Versus Normalized Ice Volume in Figure A–13					
Analog Site Estimates	**Parameter**	**Lower Bound**	**Interglacial to Intermediate or Mild Glacial**	**Mild Glacial to Glacial**	**Full Glacial Upper Bound**
Upper	Relative Ice Volume	0	0.4	0.8	1.0
	MAP (mm/yr)‡	125	190	535	513
	MAT [°C]§	15	13	8	0
Lower	Relative Ice Volume	0	0.4	0.8	1.0
	MAP (mm/yr)	125	190	243	260
	MAT [°C]	15	13	7.7	5

*MAP—mean annual precipitation
†MAT—mean annual temperature
‡100 mm/yr = 3.9 in/yr
§°C = 9/5 °F + 32

more negative value slightly dryer climates. The difference in the median MAP between the dry and wet climate sequences is approximately 90 mm/yr [3.5 in/yr], and the difference between their means is approximately 40 mm/yr [1.6 in/yr]. Similar frequency distributions of MAP based on Sharpe's lower bound MAP estimates are shown in Figure A–14(b). For the lower bound case, the difference between the median MAP is less than 20 mm/yr [0.78 in/yr]. Thus, the effect of model uncertainty is not very great when distributed over the next 1 million years and is much less than the uncertainty of climate parameters.

For some future time periods, such as the period from 100,000 to 300,000 years in the future, the model uncertainty becomes more significant. This uncertainty is illustrated by the MAP frequency distributions shown in Figure A–15 that are based on Sharpe's upper bound MAP estimates. During this time period, simulated climate and ice volume are much more sensitive to the choice of insolation parameters in the Paillard model (see Figure A–9), and the resulting range in the median values of MAP is approximately 270 mm/yr [10.6 in/yr] (Figure A–15).

A.5 Summary

The climate model of Paillard (1998) was used to create sequences of possible future climates that were then used to create possible future sequences of MAP and MAT for total-system performance assessment simulations. The model uses insolation variations due to Earth's orbital cycles as a climate-forcing process modulated by threshold insolation values that trigger changes in climate between interglacial, mild glacial, and full glacial states. The model output is in terms of discrete climate states and relative northern hemisphere ice volume.

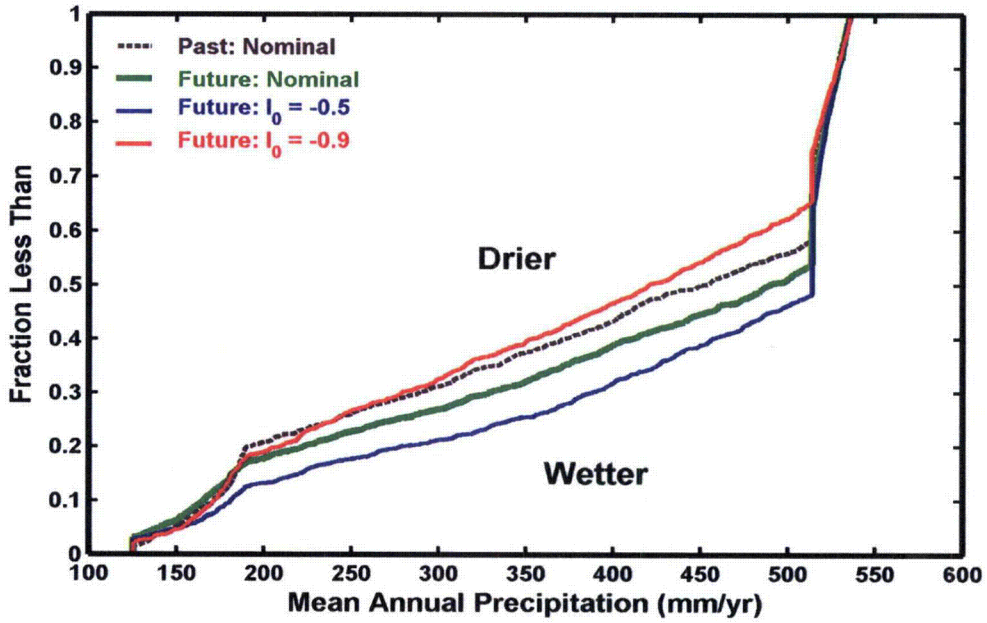

(a)

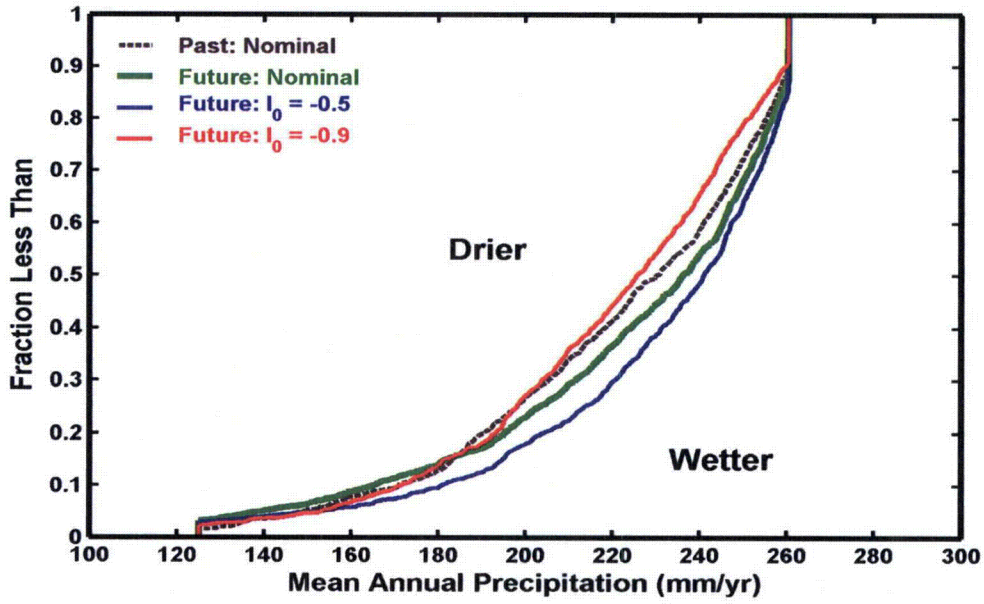

(b)

Figure A–14. Frequency Distribution of Past and Possible Future MAP for 1 Million Years After Present Based on Normalized Ice Volume Computed Using the Continuous Paillard Model and Sharpe (2003) (a) Upper Bound and (b) Lower Bound Analog Site Data. Climate End Members and MAP Values Are Listed in Table A–2. Paillard Model Parameters Are Listed in Table A–1. [100 mm/yr = 3.94 in/yr]

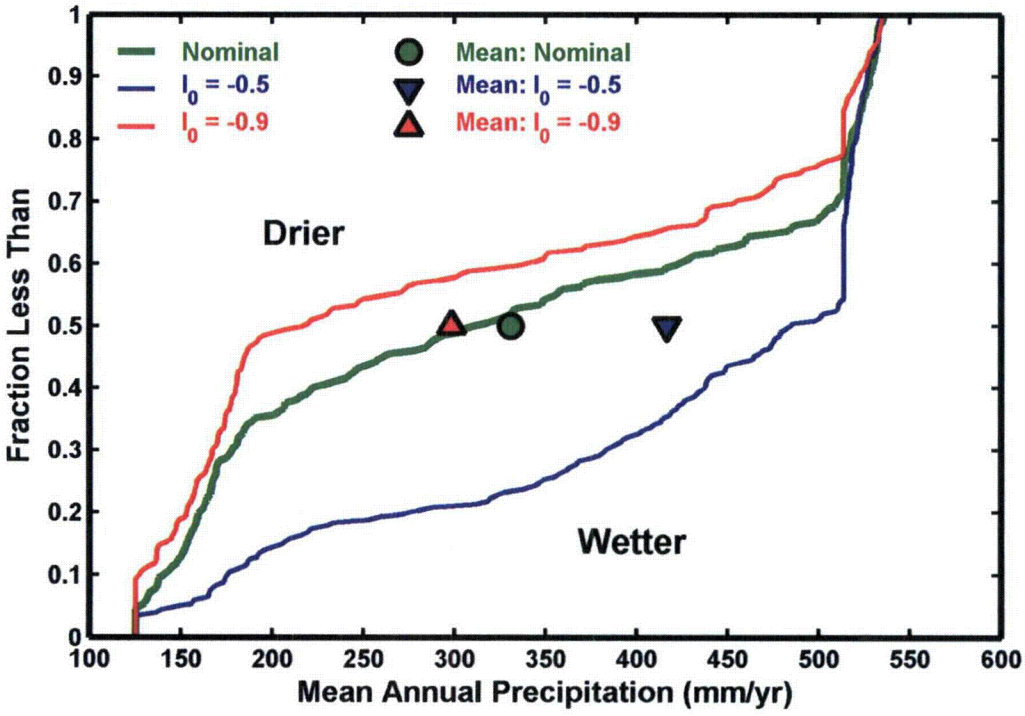

Figure A–15. Frequency Distribution of Past and Possible Future MAP During the Period 100,000 to 300,000 Years After Present Based on Normalized Ice Volume Computed Using the Continuous Paillard Model and Sharpe (2003) Lower Bound Analog Site Data. Climate End Members and MAP Values Are Listed in Table A–2. Paillard Model Parameters Are Listed in Table A–1.
[100 mm/yr = 3.94 in/yr]

The Paillard modeling approach was selected because it provided a simple and transparent method for generating possible future climates and because it had been calibrated to reproduce past climates with reasonable accuracy. In agreement with Paillard (1998), the model was found to be relatively insensitive to the values of calibration parameters with respect to simulating past climates. Simulated future climates of the next 1 million years show somewhat more sensitivity to the choice of key insolation parameters, but the fraction of the time spent in each climate state varied little on average.

The relative ice volume was used as a climate surrogate to create possible future sequences of MAP and MAT in the Yucca Mountain region. Values of MAP and MAT were described by linear functions of normalized ice volume during each of three climate states: interglacial, intermediate/mild glacial, and full glacial. Frequency distributions of MAP over the next 1 million years were computed using the upper and lower bound climate state analog site MAP from Sharpe (2003) as examples of possible future conditions. As with climate indicators, the million-year averages of MAP and MAT were not very sensitive to the choice of climate forcing parameters in the Paillard model. The greatest source of uncertainty was in the values of MAP assigned to the climate states. Averages for 100,000-year periods showed more variability, with the largest differences occurring between 100,000 and 300,000 years in the future. For this time period, the uncertainty in MAP due to uncertainty in insolation parameters was significant.

A.6 REFERENCES

Archer, D. "The Fate of Fossil Fuel CO_2 in Geologic Time." *Journal of Geophysical Research Oceans.* Vol. 110, No. C9, Article C09S05. 2005.

Archer, D. and A. Ganopolski. "A Movable Trigger; Fossil Fuel CO_2 and the Onset of the Next Glaciation." *Geochemistry Geophysics Geosystems.* Vol. 6. pp. 1–7. 2005.

Bechtel SAIC Company LLC. "Future Climate Analysis." Rev. 01. Las Vegas, Nevada: Bechtel SAIC Company LLC. 2004.

Berger, A. "Long-Term Variations of Daily Insolation and Quaternary Climatic Changes." *Journal of Atmospheric Science.* Vol. 35. pp. 2,362–2,367. 1978.

Berger, A. and M.F. Loutre. "Insolation Values for the Climate of Last 10 Million Years." *Quaternary Science Reviews.* Vol. 10. pp. 297–317. 1991.

Berger, A., M.F. Loutre, and M. Crucifix. "The Earth's Climate in the Next Hundred Thousand Years (100 kyr)." *Surveys in Geophysics.* Vol. 24. pp. 117–138. 2003.

Bertrand, C., J.-P. van Ypersele, and A. Berger. "Are Natural Climate Forcings Able to Counteract the Projected Anthropogenic Global Warming?" *Climate Change.* Vol. 55. pp. 413–427. 2002.

Broecker, W.S., D.L. Thurber, J. Goddard, T.-L. Ku, R.K. Matthews, and K.J. Mesolella. "Milankovitch Hypothesis Supported by Precise Dating of Coral Reefs and Deep-Sea Sediments." *Science.* Vol. 159. pp. 297–300. 1968.

Elkibbi, M. and J. A. Rial. "An Outsider's Review of the Astronomical Theory for the Climate: Is the Eccentricity-Driven Insolation the Main Driver of the Ice Ages." *Earth-Science Reviews.* Vol. 56. pp. 161–177. 2001.

Forester, R.M., J.P. Bradbury, C. Carter, A.B. Elvidge-Tuma, M.L. Hemphill, S.C. Lundstrom, S.A. Mahan, B.D. Marshall, L.A. Neymark, J.B. Paces, S.E. Sharpe, J.F. Whelan, and P.E. Wigand. "The Climatic and Hydrologic History of Southern Nevada During the Late Quaternary. U.S. Geological Survey Open-File Report 98–635. 1999.

Ghil, M. "Cryothermodynamics: The Chaotic Dynamics of Paleoclimate." *Physica D.* Vol. 77. pp. 130–159. 1994.

Ghil, M. and H. Le Treut. "A Climate Model with Cryodynamics and Geodynamics." *Journal of Geophysical Research.* Vol 86, No. C6. pp. 5,262–5,270. 1981.

Imbrie, J., A. McIntyre, and A.C. Mix. "Oceanic Response to Orbital Forcing in the Late Quaternary: Observational and Experimental Strategies." *Climate and Geosciences, A Challenge for Science and Society in the 21st Century.* A. Berger, S.H. Schneider, and J.C. Duplessy, eds. Boston, Massachusetts: D. Reidel Publishing Company. 1989.

Intergovernmental Panel on Climate Change. "Climate Change 2001: Synthesis Report." Cambridge, United Kingdom: IPCC, Cambridge University Press. 2001.

Le Treut, H. and M. Ghil. "Orbital Forcing, Climate Interactions, and Glaciation Cycles." *Journal of Geophysical Research.* Vol. 88, No. C9. pp. 5,167–5,190. 1983.

National Academy of Sciences. *Abrupt Climate Change: Inevitable Surprises.* Washington, DC: National Academy Press. 2002.

National Research Council. *Technical Bases for Yucca Mountain Standards.* Washington, DC: National Academy Press. 1999.

National Oceanic and Atmospheric Administration. "Orbital Variations and Insolation Database, NOAA/NCDC/WDC Paleoclimatology <ftp://ftp.ncdc.noaa.gov/pub/data/paleo/insolation/contents.91>. (20 August 2006).

NRC. "Issue Resolution Status Report on Methods to Evaluate Climate Change and Associated Effects at Yucca Mountain." Washington, DC: NRC. 1997.

Paillard, D. "Glacial Cycles: Toward a New Paradigm. Reviews of Geophysics." Vol. 39. pp. 325–346. 2001.

———. "The Timing of Pleistocene Glaciations From a Simple Multiple-State Climate Model." *Nature.* Vol. 391. pp. 378–381. 1998.

Philander, S.G. and A.V. Federov. "Role of Tropics in Changing the Response to Milankovich Forcing Some Three Million Years Ago." *Paleoceanography.* Vol. 18. pp. 23-1–23-11. 2003.

Roper, L.D. "Insolation Codes for Windows." <http://roperld.com/science/InsolationCodes.htm>. 2003.

Shackley, S., P. Young, S. Parkinson, and B. Wynne. "Uncertainty, Complexity and Concepts of Good Science in Climate Change Modelling: Are GFMs the Best Tools?" *Climate Change.* Vol. 38. pp. 159–205. 1998.

Shaffer, J.A., R.S. Cervany, and R.I. Dorn. "Radiation Windows as Indicators of an Astronomical Influence on the Devil's Hole Chronology." *Geology.* Vol. 24. pp. 1,017–1,020. 1996.

Sharpe, S. "Future Climate Analysis—10,000 Years to 1,000,000 Years After Present." MOD–01–001. Rev 01. Reno, Nevada: Desert Research Institute. 2003.

Walter, G. "Analysis of Factors Contributing to Uncertainty in Estimating Future Climates at Yucca Mountain." San Antonio, Texas: CNWRA. 2005.

APPENDIX B

ITYM MODEL DESCRIPTION

B.1 ITYM Conceptual Model

The distributed infiltration model Infiltration Tabulator for Yucca Mountain (ITYM)[1] uses an abstracted representation for net infiltration derived from many one-dimensional simulations. The ITYM model provides a spatial distribution of net infiltration using square grid cells that are 30 m [98 ft] on a side. Each grid cell has a set of associated parameters based on field mapping, laboratory analyses, and theoretical models. The ITYM model is intended to provide a collection of grid-cell estimates that capture the frequency distribution of infiltration within the constraints of grid resolution, as well as provide reasonable spatial patterns.

The ITYM model is used to tabulate areal-average net infiltration as a function of decade-average precipitation and temperature for the Total-system Performance Assessment (TPA) code (Mohanty, et al., 2002) while accounting for uncertainties in hydraulic parameters. ITYM uses a response relationship between soil and bedrock hydraulic parameters, decade-average climatic parameters, and decade-average infiltration that was developed using the BREATH code (Stothoff, 1995). Each one-dimensional simulation is driven by a decade of hourly weather measurements from Desert Rock, Nevada, on the Nevada Test Site (Stothoff, 1999). A typical decade was used, with an isolated wet year and a two-year sequence of wet years amongst seven drier years. Each simulation repeated the decade until decadal-average flux in the column was vertically uniform (i.e., the initial conditions did not affect the solution), and the last decade flux estimate was used as the estimate. A total of approximately 500 one-dimensional simulations explored combinations of hydraulic properties and climatic conditions to derive the response surface.

B.2 Spatially Distributed Inputs

The computational grid is derived from a standard U.S. Geological Survey digital elevation model with 30-m [98-ft] grid cell sides. Input properties are specified by defining additional input files with an identical grid to represent bedrock unit, soil unit, soil thickness, wind speed, upslope contributing area, and average upslope soil thickness. The bedrock map by Day, et al. (1998) is used to describe the spatial distribution of bedrock units, while the soil map derived by Lundstrom, et al. (1994, 1995,1996) and Lundstrom and Taylor (1995) is used to describe the spatial distribution of soil units.

The contributing area and average upslope soil thickness coverages are preprocessed from the underlying grid. The soil thickness coverage is derived using a mechanistic model describing the equilibrium mass balance of surficial materials, including dust deposition, overland flow of sediment, and creep on hill slopes. The soil thickness model is generally consistent with field observations from trenches, drill pads, pits, and other exposures. The windspeed coverage is derived from wind observations at Yucca Mountain meteorological stations corrected for the sheltering effect of the east-west washes. Upslope contributing area is calculated using the soil-thickness mechanistic model, as is the average upslope soil thickness.

B.3 Uncertainty in Input Properties

Almost all input properties are considered uncertain, with a normal or lognormal distribution. Correlation is allowed within groups of related properties, such as the hydraulic properties of a soil or bedrock unit. The mean, standard deviation, and correlation coefficients used for the probability distribution are also normally distributed, and these statistical parameters may be bounded or unbounded.

---

[1]Infiltration Tabulator for Yucca Mountain is referenced frequently throughout this report; consequently, the abbreviation ITYM will be used.

B.4 Matrix Hydraulic Properties

The statistical description of the hydraulic properties used to describe the bedrock and soil units are derived from U.S. Geological Survey measurements, supplemented by independent analysis. Bedrock fractures are the dominant pathway for water to migrate deep below the rooting zone, because the matrix permeability for welded tuffs at Yucca Mountain is so small that flows are severely limited in the matrix. Accordingly, bedrock matrix properties have little influence on net infiltration calculations. Bedrock matrix properties reproduce the model values from Flint, et al. (1996), although uncertainty in the properties was considered. Few measurements of soil hydraulic properties are available at Yucca Mountain; the soil-property estimates reported by Flint, et al. (1996) are derived from textural analyses. Limited independent field observations suggest that soil texture is almost uniform across hillslopes within the Footprint Box (defined in Section 3.2), and independently estimated properties are generally consistent with the Flint, et al. (1996) properties. Accordingly, the Flint, et al. (1996) properties were used, but were considered uncertain.

Each type of porous medium was described with van Genuchten soil hydraulic model properties, with normal distributions for the base-10 logarithms of intrinsic permeability, van Genuchten scaling pressure, and porosity, as well as the untransformed van Genuchten *m*.

B.5 Fracture Hydraulic Properties

The hydraulic properties of bedrock fractures are less well known than either the bedrock matrix or soil properties in the model domain. Three sources of uncertainty arise when considering bedrock fractures: (i) the cross-sectional area perpendicular to flow, (ii) the type of fracture filling, and (iii) the hydraulic properties of the fillings. However, the one-dimensional simulations are relatively insensitive to fracture properties, suggesting that delivery of water to the soil/bedrock interface may be the dominant factor controlling net infiltration and implying that uncertainty in net infiltration may be dominated by uncertainty in soil properties and soil thickness rather than uncertainty in fracture properties.

Information is limited regarding the near-surface bedrock-fracture properties affecting infiltration across Yucca Mountain. Fracture mapping on exposed pavements tend to focus on the number and orientation of fractures, with some efforts to measure apertures as well (Barton, et al., 1993; Waiting, et al., 2001) but less focus on fracture fillings. Independent field observations by the author of this report suggest that near-surface fractures at Yucca Mountain are usually filled with either the fine component of the overlying soil or a mixture of calcium carbonate and siliceous materials. These observations suggest that calcium carbonate/silicate fillings appear to be prevalent in systems with relatively narrow apertures and infrequent fractures, such as lithophysal units. Soil fillings are more evident in units with relatively large-aperture fractures and fissures, such as caprock and nonlithophysal units, although it is possible that carbonates or silicates appear at depth in fractures that have soil fillings near the soil/bedrock interface. Unfilled fractures appear to be rare in near-surface welded tuff, and even apparently unfilled fractures in well-washed areas of welded tuff such as active bare-rock channels in Split Wash appear to be filled below the channel bottom, based on observations of very slow drainage rates of ponded water. Unfilled fractures are common in the nonwelded units, but little evidence of flow through the fractures in nonwelded units has been found (Moyer, et al., 1996). Little information is available about the cross-sectional area of surficial fractures available for flow of water.

The ITYM model considers fractures to be partially soil-filled, partially carbonate-filled, and partially unfilled. The fraction of the fracture area assigned to each category is based on scientific judgment. A separate pathway is considered for each filling in each grid cell; infiltration for the grid cell is assumed to come from the pathway with the largest infiltration rate. Hydraulic properties describing soil fillings are assumed identical to the overlying soil. Hydraulic properties describing carbonate fillings are based on the limited set of samples with hydraulic measurements in the along-fracture direction in DTN:GS950308312210.002, Preliminary Fault/Fracture Properties, and DTN:GS950708312211.003, Updated Fault/Fracture Properties for Fast Pathways Model as well as from caliche measurements by

Baumhardt and Lascano (1993). Unfilled fractures are described with properties equivalent to parallel plates, but are so permeable that simulations are not sensitive to the unfilled-fracture hydraulic properties.

B.6 Plant Transpiration Model

The plant transpiration component of the ITYM model is highly abstracted, describing the efficiency of plant transpiration for removing water that would otherwise become net infiltration. The efficiency is assumed to be approximately 30 percent with no soil and to increase exponentially with soil thickness to approximately 99 percent efficiency with deep soil. This model is not tied to individual plant types and communities, and is the primary means for calibrating the ITYM model to observations.

B.7 Model Output

The ITYM model calculates the mean and standard deviation of decade-average infiltration and, if requested, log-transformed decade-average infiltration for each grid cell in the model. Each calculation is performed for a climate described by decade-average precipitation and decade-average temperature at a reference elevation of 1,400 m [4,600 ft], approximately 100 m [330 ft] below the crest of Yucca Mountain. Climatic parameters are adjusted for elevation-dependent effects within the ITYM model. Topography, upslope properties, and bedrock and soil maps are assumed to be the same and certain for any climatic condition. All other input properties are considered uncertain (and independent of climate) with statistical properties explicitly considered through Monte Carlo sampling. Each calculated statistic is output on the same grid used for input.

Multiple climatic conditions may be considered during a single ITYM run, typically bounding the entire range of climatic conditions anticipated for subsequent analysis. In the main body of this report, the precipitation range for all climates is covered with discrete values of 100, 200, 400, and 800 mm/yr [3.9, 7.9, 15.7, and 31.5 in/yr]; and the temperature range for all climates is covered with discrete values of 0, 7.3, 14.7, and 22 °C [32, 45.2, 58.4, and 71.6 °F], resulting in a total of 16 separate output grids for each statistic. ITYM performs an independent Monte Carlo analysis for each combination of precipitation and temperature; 2,000 realizations are used in this report for each combination of mean decadal precipitation and temperature.

Decade-average net infiltration is approximately lognormally distributed in each grid cell, with the coefficient of variation decreasing as the mean infiltration increases. The probability distribution of model-estimated areal-average decade-average infiltration is reasonably described using a lognormal distribution with the grid-cell-average mean and standard deviation of decade-average infiltration. The cumulative frequency distribution shown in Figure B–1 for the climatic case most like present-day conditions {MAP = 200 mm/yr [7.9 in/yr] and MAT = 14.7 °C [58.5 °F]}. All 59,700 grid cells in the full 54 km^2 [20.8 mi^2] domain are used to calculate the curves in Figure B–1. A good match is obtained between the 2,000 realizations of the actual areal-average infiltration, a lognormal distribution from the 2,000 areal average values, and a lognormal distribution from the grid-cell-average statistics. The lognormal distribution of areal average infiltration has the same mean as the corresponding average grid cell, but has a slightly smaller standard deviation. The results reported in Section 3.3 of the main body of this report use grid-cell-average statistics to estimate areal-average decade-average infiltration.

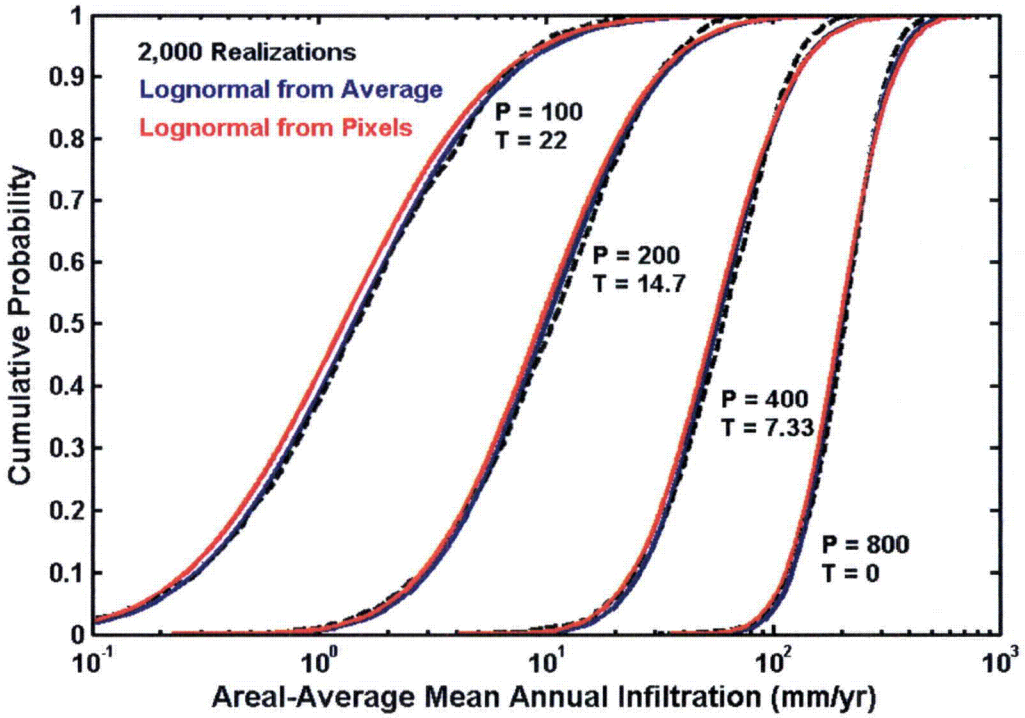

Figure B–1. Cumulative Probability Distribution for Areal-Average MAI. Areal-Average MAI From 2,000 Realizations Compares Well to Two Lognormal Distributions: One With the Same Mean and Standard Deviation as the Areal-Average Realizations and One With the Average Mean and Standard Deviation for the 59,700 Pixels.

B.8 Climate-Induced Property Changes

It is unlikely that topography will change significantly over the performance period, but it is quite possible that soil, fracture, bedrock, and vegetation properties will change over time, and other climatic properties such as relative humidity and windspeed may also change appreciably.

Soil thickness and hydraulic properties may be more dynamic than fracture properties; bedrock matrix properties will almost certainly be relatively unchanged. Hillslope soil reservoirs in the arid American Southwest are thought to be dynamic over glacial time scales, with soils developing over tens of thousands of years during wetter or cooler periods and rapidly being stripped from hillslopes as plant cover drops below a threshold value during interglacial periods (Bull, 1991). The soil thickness distribution and soil hydraulic properties used by ITYM are representative of present-day conditions, which are likely intermediate between thin soils with coarse textures during the early Holocene and likely to have thicker soils with finer textures during late glacial conditions. A numerical experiment performed by Stothoff, et al. (1999) suggests that replacing present-day soil thickness and texture with properties representative of a glacial-analog site may reduce net infiltration by a factor of two.

Fracture properties may vary over glacial cycles, but changes in fracture properties are highly uncertain. The most dynamic fracture component may be the fraction of the fractures filled with carbonates, because increased moisture may tend to redistribute carbonates. Fracture properties are poorly known even under present-day conditions; thus systematic variation in fracture properties is not explicitly considered and the associated uncertainty is incorporated in the uncertainty in the average value of fracture properties.

Climatic properties such as cloud cover, relative humidity and wind speed will likely change somewhat over glacial cycles, but precipitation and temperature have the dominant influence on calculated net infiltration (Stothoff, 1997). Systematic variation in climatic properties other than precipitation and temperature is neglected because these have relatively small effects on net infiltration.

B.9 REFERENCES

Barton, C.C., E. Larsen, W.R. Page, and T.M. Howard. "Characterizing Fractured Rock for Fluid-Flow, Geomechanical, and Paleostress Modeling: Methods and Preliminary Results From Yucca Mountain, Nevada. U.S. Geological Survey Open-File Report 93–263. 1993.

Baumhardt, R.L. and R.J. Lascano. "Physical and Hydraulic Properties of a Calcic Horizon." *Soil Science*. Vol. 155, No. 6. pp. 368–375. 1993.

Bull, W.B. "Geomorphic Responses to Climatic Change." Oxford, England: Oxford University Press. 1991.

Day, W.C., C.J. Potter, D.S. Sweetkind, and C.A. San Juan. "Bedrock Geologic Map of the Central Block Area, Yucca Mountain, Nye County, Nevada." U.S. Geological Survey Miscellaneous Investigations Series No. I–2601. 1998.

Flint, A.L., J.A. Hevesi, and L.E. Flint. "Conceptual and Numerical Model of Infiltration for the Yucca Mountain Area, Nevada." Milestone No. 3GUI623M. Las Vegas, Nevada: DOE. 1996.

Lundstrom, S.C. and E.M. Taylor. "Preliminary Surficial Deposits Map of the Southern Half of the Topopah Spring NW 7.5-Minute Quadrangle." U.S. Geological Survey Open-File Report No. 95-134. Scale 1:12,000. 1995.

Lundstrom, S.C., S.A. Mahan, and J.B. Paces. "Preliminary Surficial Deposits Map of the Northwest Quarter of the Busted Butte 7.5-Minute Quadrangle." Scale 1:12,000. U.S. Geological Survey Open-File Report No. 95-133. 1996.

Lundstrom, S.C., J.W. Whitney, J.B. Paces, S.A. Mahan, and K.R. Ludwig. "Preliminary Surficial Deposits Map of the Southern Half of the Busted Butte 7.5-Minute Quadrangle." U.S. Geological Survey Open-File Report No. 95-131. Scale 1:12,000. 1995.

Lundstrom, S.C., J.R. Wesling, E M. Taylor, and J.B. Paces. "Preliminary Surficial Deposits Map of the Northeast Quarter of the Busted Butte 7.5-Minute Quadrangle." U.S. Geological Survey Open-File Report No. 94-341. Scale 1:12,000. 1994.

Mohanty, S., T.J. McCartin, and D.W. Esh. "Total-system Performance Assessment (TPA) Version 4.0 Code: Module Descriptions and User's Guide." San Antonio, Texas: CNWRA. 2002.

Moyer, T.C., J.K. Geslin, and L.E. Flint. "Stratigraphic Relations and Hydrologic Properties of the Paintbrush Tuff Nonwelded (PTn) Hydrologic Unit, Yucca Mountain, Nevada." U.S. Geological Survey Open-File Report No. 95-397. 1996.

Stothoff, S.A. "Infiltration Abstractions for Shallow Soil Over Fractured Bedrock in a Semiarid Climate." San Antonio, Texas: CNWRA. 1999.

———. "Sensitivity of Long-Term Bare Soil Infiltration Simulations to Hydraulic Properties in an Arid Environment." *Water Resources Research*. Vol. 33, No. 4. pp. 547–558. 1997.

———. NUREG/CR–6333, "BREATH Version 1.1—Coupled Flow and Energy Transport in Porous Media: Simulator Description and User Guide." Washington, DC: NRC. July 1995.

Stothoff, S., O. Chadwick, D. Groeneveld, D. Or, R. Fedors, and D. Woolhiser. "Assessing Changes in Deep Percolation Over a Glacial Cycle Due to Linked Changes in Climate, Soils, and Vegetation at Yucca Mountain, Nevada." *Supplement to Eos, Transactions*. Vol. 80, No. 17. Section S3. 1999.

Waiting, D.J., R. Chen, J.G. Crider, W.M. Dunne, R.W. Fedors, D.A. Ferrill, M.B. Gray, B.E. Hill, P.C. La Femina, H.L. McKague, A.P. Morris, D.W. Sims, and J.A. Stamatakos. "Technical Assessment of Structural Deformation and Seismicity at Yucca Mountain, Nevada." San Antonio, Texas: CNWRA. 2001.

APPENDIX C

DATA SOURCES

Table C–1. Data Sources and Date Obtained for the Observations Used in the Report

Description	Source	Date
USGS*/NOAA† North American Packrat Midden Database	http://esp.cr.usgs.gov/data/midden/search.html	08/22/2006
Raw tree-ring widths (Methusaleh Walk -6000 to 1979)	http://www.ncdc.noaa.gov/paleo/drought/drght_graumlich.html	04/05/2006
Tree-ring chronology (Methusaleh Walk -6000 to 1979)	http://www.ncdc.noaa.gov/paleo/drought/drght_graumlich.html	04/05/2006
Yucca Mountain Project meteorological observations	http://www.ymp.dri.edu/index.html	06/21/2006
Nevada Test Site meteorological observations	http://www.sord.nv.doe.gov/SORD_Rain.html	07/01/2006
Global Historical Climatology Network data files	http://www.ncdc.noaa.gov/cgi-bin/res40.pl?page=ghcn.html	07/05/2006
SPECMAP‡ stacked $\delta^{18}O$ sequence	http://www.ngdc.noaa.gov/mgg/geology/specmap.html	07/09/2006
Devils Hole $\delta^{18}O$ sequence	http://pubs.usgs.gov/of/1997/ofr97-792/	06/27/2006

*U.S. Geological Survey
†National Oceanic and Atmospheric Administration
‡Spectral Mapping Project